Stefan Reimond, BSc.

Representation of the Gravity Field of Irregularly Shaped Bodies

MASTER'S THESIS

to achieve the university degree of

Diplom-Ingenieur

Master's degree programme: Geomatics Science

submitted to

Graz University of Technology

Supervisor

Dr.-Ing. Dipl.-Ing. Oliver Baur

Institute of Geodesy - Working Group Theoretical Geodesy and Satellite Geodesy
Univ.-Prof. Dr.-Ing. Torsten Mayer-Gürr

Graz, January 2015

AFFIDAVIT

I declare that I have authored this thesis independently, that I have not used other than the declared sources/resources, and that I have explicitly indicated all material which has been quoted either literally or by content from the sources used. The text document uploaded to TUGRAZonline is identical to the present master‘s thesis dissertation.

Date

Signature

Acknowledgements

I would like to thank, first and foremost, my supervisor Oliver Baur for his continuous support over the last few months. Without his valuable ideas, his optimism and enthusiasm as well as sheer endless patience this thesis would not have been possible. I am glad and thankful to be able to continue this collaboration.

I greatly appreciate Torsten Mayer-Gürr for helping with the administrative part of carrying out the thesis.

Furthermore I would like to thank my colleagues at the Space Research Institute in Graz for not only welcoming me to the team in such a nice and uncomplicated way but also for numerous coffee breaks, interesting conversations and entertaining movie nights.

This thesis is only the final stop on a long journey called university education. A lot of work and even more fun was part of it. I wish to thank all my dearest colleagues and friends for joining me on this trip ('scuse the cheesiness).

It is a great pleasure to thank all my family for supporting me in every conceivable way. No time too late, no way too long - I could and can always turn to you - thanks!

Writing a master's thesis can be tough. Sometimes you try one thing, you fail. Then you think about another thing and you fail again. Yes, you might even get frustrated. If it wasn't for my girlfriend, who never lost patience and always encouraged me to carry on, I could hardly have completed my thesis. A very special thanks to you, Anna!

Abstract

Knowledge of the gravitational field of a small body, e.g. a comet or asteroid, is crucial in order to study a spacecraft's motion in its environment and to infer geophysical properties. Traditionally, the gravitational field of a body is modeled by means of spherical harmonics. For bodies of near-spherical shape (such as the Earth), this is an adequate method, because the reference figure, i.e. a sphere, snugly fits the body. For irregularly shaped bodies, however, the adoption of spherical harmonics might be a sub-optimal choice. As an alternative, oblate or prolate spheroidal harmonics (OH or PH, reference figure is an ellipsoid of revolution) or ellipsoidal harmonics (EH, reference figure is a tri-axial ellipsoid) should be considered. The latter will in general be the best choice in terms of aptness of the reference figure. The downside of EH, however, lies in the considerably increased (numerical) complexity of the computation of the base functions, i.e., the Lamé functions of the first and second kind. OH or PH represent a promising path down the middle. Elongated bodies (such as Asteroid 433 Eros) are often similarly well approximated by a prolate spheroid as by the corresponding tri-axial ellipsoid. Contracted bodies, on the other hand, can be described accordingly well by means of an oblate spheroid.

We compare the SH, OH, PH and EH gravitational field parameterizations for different celestial bodies, including Rosetta's target comet 67P. The tasks are as follows: Based on the polyhedral representation of a body's shape, the gravitational potential and acceleration vector is computed under the assumption of constant density for evenly or irregularly distributed points inside or outside the respective reference figures. Real orbit data of the NEAR shoemaker is included as well. In a least-squares adjustment, these quantities serve as observations in order to determine the SH, OH, PH and EH series coefficients. Harmonic synthesis yields gravitational fields which are then compared with the corresponding forward-modeled data. Due to the various data distributions, conclusions can be drawn concerning the performance of the four methods both inside and outside their respective convergence regions.

The results of this simulation prove indeed a faster convergence of EH compared to all other parametrizations. Still, PH and OH perform similarly well and should be preferred due to better stability of the basis functions. SH are still the best choice if all computation or evaluation points are located far outside the attracting masses.

Kurzfassung

Die erfolgreiche Manövrierung einer Raumsonde in der Nähe eines Kometen oder Asteroiden gelingt nur mithilfe eines zuverlässigen Gravitationsfeldmodells. Auch für die Untersuchung geophysikalischer Vorgänge und Eigenschaften dieser Körper ist Kenntnis der Gravitationswirkung unumgänglich. Traditionell wird das Schwerefeld eines Körpers unter Zuhilfenahme von Kugelfunktionen (SH, sphärisch Harmonische) beschrieben. Während dies für Objekte kugelähnlicher Gestalt (wie z.B. der Erde) eine durchaus geeignete Methode darstellt, sollte für ungleichmäßig geformte Körper wie Asteroiden über Alternativen nachgedacht werden. Die Wahl der Referenzfigur sollte der tatsächlichen Form des Körpers möglichst nahe kommen. Sphäroide oder dreiachsige Ellipsoide stellen eine weitaus bessere geometrische Approximation als Kugeln dar. Die Lösung der Laplace Gleichung in diesen Parametrisierungen führt in analoger Weise zu sphäroidisch-harmonischen (OH wenn abgeflacht, PH wenn langgezogen) und ellipsoidisch-harmonischen (EH) Reihenentwicklungen. Ellipsoide kommen der tatsächlichen Form immer am nächsten, die Komplexität der zugrundeliegenden Basisfunktionen (Lamé Funktionen) erschwert jedoch die Anwendung von EH. Als attraktiver Zwischenweg präsentieren sich OH und PH, die je nach Form des Asteroiden eine vergleichbar gute Lösung liefern.

In dieser Arbeit werden die SH, OH, PH und EH Parametrisierungen des Gravitationsfeld für verschiedene Himmelskörper getestet und verglichen. Die Arbeitsschritte sind wie folgt: Ausgehend von einem Polyeder-Modell des Körpers werden auf analytischem Wege unter Annahme konstanter Dichte Gravitationspotential und –beschleunigung in Berechnungspunkten sowohl innerhalb als auch außerhalb der jeweiligen Referenzfiguren bestimmt. Inkludiert sind auch Orbitdaten der Raumsonde NEAR Shoemaker. Mithilfe dieser Größen werden im Rahmen einer Ausgleichung nach kleinsten Quadraten die Koeffizienten der jeweiligen Reihenentwicklungen geschätzt. Die rückwärtsgerechneten Gravitationswerte werden anschließend mit den Ausgangswerten verglichen.

Die Ergebnisse dieser Simulation spiegeln die geometrische Situation wider. Die EH erweisen sich stets als die am schnellsten konvergierende Reihenentwicklung. Der Unterschied zu PH oder OH ist aber beinahe verschwindend. Aufgrund der numerisch einfacheren Berechnung der Basisfunktionen sind die sphäroidalen Paramtrisierungen daher zu bevorzugen. Befinden sich jedoch alle Berechnungspunkte in großem Abstand von den anziehenden Massen, so stellen SH immer noch die beste Wahl bei der Modellierung dar.

Contents

List of Figures

List of Tables

Chapter 1.

Introduction

1.1. Motivation

On November 12, 2014, the space mission Rosetta set a milestone in space science history when it successfully lowered its lander Philae on the surface of Comet 67P/Churyumov–Gerasimenko, short 67P. After more than 10 years traveling through space, it became the first spacecraft to orbit and soft-land on a comet. Little was known of 67P before, only rough estimates of its physical and geometrical properties had been made. It is no wonder, then, that scientists at ESA's mission control center were pretty surprised when Rosetta's on-board camera delivered first high resolution pictures of what seemed to be a giant space rubber duck. The comet is by far more irregularly shaped than previously supposed. That gave a lot of people headaches, because as a consequence the chances of successfully landing on the comet shrunk tremendously.

Why so? First of all, the surprisingly steeply and rocky surface obviously wouldn't really *support* a soft and safe landing. The lack of any large flat areas made it especially hard to choose a suitable landing site, since the risk of the lander being damaged or rolling over would increase a lot by selecting an unsuitable option. On September 15, 2014, however, after a few weeks of considerations and evaluations, the mission's masterminds proudly presented the preferred spot where Philae would be supposed to be set down. A small area of about one square kilometer on the "head" of 67P[1].

The harsh ground conditions, however, have not been the only challenge the responsible scientists and engineers were facing during the landing planning process. When Rosetta arrived at comet 67P in summer 2014, it was pulled by the comet's gravitational attraction and captured within its gravity field. In order to safely navigate the spacecraft near the comet and to precisely determine the final landing trajectory of Philae, knowledge of the gravity field was crucial.

[1] http://www.esa.int/Our_Activities/Space_Science/Rosetta/J_marks_the_spot_for_Rosetta_s_lander

This is where this thesis intervenes. In this work, we wish to investigate different methods of modeling small bodies' gravitational fields. The comet Chury, as Rosetta's target is fondly called, will here only play an ancillary role. We are interested in finding suitable methods to represent gravity of arbitrary shaped and sized bodies.

Traditionally, the gravity field of a body is represented in terms of harmonic series using a set of global basis functions. In most cases, these basis functions are spherical harmonics. The theory and also practical aspects of spherical harmonics have been extensively studied and discussed over the last decades or even centuries. Thanks to dedicated space missions such as GRACE and GOCE it is possible, nowadays, to model the Earth's gravity field more accurately than ever before. We can observe ice mass changes in Greenland as well as ocean tides in Madagascar. We see freshwater losses in India and post-glacial rebound effects in Canada. All these applications make use of, inter alia, spherical harmonics.

But, as the name already implies, these types of basis functions are referred to a sphere as reference figure. Even though the Earth is flattened at the poles and therefore not perfectly spherical, this small bias is negligible. While this approach is fine for near-spherical bodies such as the Earth or the Moon, problems may occur when we choose spherical harmonics to represent the gravitational field of irregularly shaped bodies.

But what else is there? What reference figure fits a rubber duck?

As a first approach, one might use spheroids, i.e., bi-axial ellipsoids, to approximate the shape of such a body. The corresponding basis functions are then called spheroidal harmonics. If the ellipsoid takes the shape of a hamburger bun, we speak of oblate spheroids. Football-shaped ellipsoids are called prolate. As mentioned before, the Earth is flattened at the poles and thus resembles an oblate spheroid. The use of oblate spheroidal harmonics to model the gravitational potential is therefore nothing totally strange to geodesists. Prolate spheroidal harmonics, however, have only recently been "discovered" for this purpose, see Fukushima (2014).

A generalization of spheroids leads to tri-axial ellipsoids as reference figures and hence to ellipsoidal harmonics. This method, however, has the disadvantage of becoming increasingly complex.

A different approach to describe the gravitational field is by means of forward modeling techniques. If the shape of the attracting body is known, gravitational effects can fairly easily be evaluated for any point outside the body. The huge disadvantage of this method, however, is the requirement of a model describing the mass distribution in the body's interior. Obviously such models hardly exist.

1.2. Prior Work

The theory of ellipsoidal harmonics goes back to the ingenious mathematicians of the 19^{th} century and was elaborated in great detail by Byerly (1893) and Hobson (1931) and more recently by Dassios (2012). Regarding the usage of ellipsoidal harmonics for the purpose of gravitational field modeling, similar investigations were carried out by Garmier and Barriot (2002), Dechambre and Scheeres (2002) and Hu (2012), to name but a few. All authors draw the conclusion, that ellipsoidal harmonics are more suitable for highly irregularly shaped bodies than spherical harmonics. Also, that the computational complexity is very high and numerical issues allow only for the computation of low degrees, say less than 20.

Spheroidal parametrizations of the Earth's gravitational field were extensively treated by Balmino et al. (1991) and Thong (1989). Application to asteroids was also recently suggested by Fukushima (2013, 2014). The advantage of this approach is clearly the simplified computation of the basis functions, their numerical stability and as a consequence the possibility of determining the gravity field with higher spatial resolution.

To represent the "true" gravitational field, the polyhedral method seems to be the standard. Analytical expressions for the gravity effects of simple three-dimensional objects (for instance cubes) have been known for many decades (cf. MacMillan (1958)). A generalization to polyhedrons was established by Werner and Scheeres (1997) and recently refined by Tsoulis (2012) and D'Urso (2013).

1.3. Small Bodies

Small bodies can be found throughout the solar system. Many different classification approaches exist, which try to divide those objects up into categories based on geometrical (e.g., orbit, size), physical or chemical (e.g., emissions spectra, composition) or other properties. An extensive treatise of this topic is beyond the scope of this thesis as well as the author's personal knowledge. For more details the reader is referred to the literature.

Except for planets, dwarf planets and artificial satellites every object in the solar system is defined as a small body (IAU, 2006). In general we speak of asteroids, comets and planetary satellites, e.g. the Moon. In the following, based on Scheeres (2012), a few facts have been compiled to provide some overview information and to prepare a smooth start into this otherwise highly mathematical text.

Asteroids are small bodies traveling on heliocentric orbits. Small, in this case, is anything between a few meters of diameter up to almost 1000 km. Nevertheless, they

are smaller than planetary satellites so that their gravitational attraction is insufficient to form them into a spherical or spheroidal shape. They are inactive and consist mainly of rocky material. So far, more than 600000 asteroids have been counted in our solar system and this number increases daily[2]. Most asteroids are located within the Asteroid Belt between Mars and Jupiter.

Comets, in contrast to asteroids, are active bodies, composed of rock and ice. They orbit the Sun and begin to outgas when the distance between them decreases. The effect of outgasing causes the comet to form a tail, which can also be seen from Earth. The size of the nucleus, i.e., the rocky core of a comet, is in the range of that of asteroids. Its tail, on the other hand, can reach a length of up to one million kilometers. The remains of an outgased comet are usually indistinguishable from asteroids or meteoroids, how small asteroids are referred to.

The origin of these small bodies goes back to the formation of the solar system about 4.6 billion years ago. It is believed, that during this era, Jupiter prevented those little rocks from forming a planetary body. Instead, they collided and broke apart into smaller objects. A process, which is still ongoing.

During its journey through our solar system, some of these asteroids and comets cross the Earth's orbit around the Sun. They do not only attract the science community's attention, but also the public's. Extraterrestrial objects have always been a fascination for human beings. Not without reason they play a big role in a lot of science fiction stories and movies. This fascination arises primarily from the spectacular possibility of an impact on the Earth's surface. Scientists, on the other hand, are eager to study the small body itself. By knowing all about the geological and chemical composition of these drifting time capsules, we might learn more about the early ages of the universe. And to put the icing on the cake, the dramatic theory of a comet bringing life to Earth billions of years ago shall be mentioned but left to to the reader to be pursued. We have good reasons, after all, to engage in the exploration of small solar system bodies. Dedicated missions planned by international space agencies prove this urge, to know more about what is and what has been going on in outer space.

1.4. Structure of the Present Work

We start by setting up some important notations and definitions concerning curvilinear coordinate systems in Chapter 2. Spherical, spheroidal and ellipsoidal coordinates and their relations to Cartesian coordinates will be examined.

[2] http://ssd.jpl.nasa.gov/?body_count

In Chapter 3 we will touch a few aspects of the theory of gravitation and potential. We will take a look at Laplace's equation in each of the reference systems defined in Chapter 2 and present the respective solutions. These are the first and second kinds of associated Legendre functions and Lamé functions.

Chapter 4 discusses the practical aspects of all harmonic functions. A close look will be taken on the applicability for different sized and shaped reference figures and what restrictions one might encounter when using these functions.

Chapter 5 deals with forward modeling techniques and provides formulas for determineing gravitational effects of constant density polyhedrons. A brief summary of available shape file formats is included as well.

Chapter 6 establishes the relation between observations taken outside the attracting body and the underlying gravitational field. We will also briefly sketch out the idea of least squares estimation, which will be the method used to achieve this task.

We tested our implementation on different bodies. Particular emphesis, however, has been out on Asteroid 433 Eros. Due to the up-to-date nature of the Rosetta mission, investigations have also been carried out on comet 67P/Churyumov–Gerasimenko. Since both Eros and "Chury" are quite oddly shaped, the more sphere-like asteroids 101955 Bennu and 29 Amphitrite have also been included in our tests. Our results are summarized in Chapter 7.

Finally, in Chapter 8 we will summarize and discuss our results. Conclusions about pros and cons will be drawn and an outlook to possible future work is presented.

Chapter 2.

Curvilinear Coordinate Systems

2.1. General Remarks

We start with setting up some important notations regarding coordinate systems that will be used throughout this thesis. First of all, a point in the three-dimensional Euclidean space will generally be referred to as P. This point P has three components and is embedded into a curvilinear coordinate system, which sometimes will be called reference system. By fixing one coordinate and letting the others vary, we find so-called coordinate surfaces. Intersection lines of two coordinate surfaces in such systems are in general curved. We will only make use of orthogonal coordinate systems, which have the characteristic that the family of coordinate surfaces intersect each other always orthogonally, i.e., at right angles.

We will be dealing with five different types of coordinates and respective systems:

1. Cartesian coordinates
2. Spherical coordinates
3. Oblate (spheroidal) coordinates
4. Prolate (spheroidal) coordinates
5. Ellipsoidal coordinates

In the following sections general definitions of these systems will be given. Moreover, the relation between each of the systems with the Cartesian system will be established. Finally, for later purpose, the general element of arc in each system is stated.

2.2. Cartesian Coordinates

These coordinates form a special case of curvilinear systems since each of the three coordinate surfaces is a plane, hence, their intersections are straight lines. There are three distinct coordinate lines which meet in one common point referred to as the origin of the reference system. The position vector $\mathbf{r}$ of a point P w.r.t. this system can be defined by means of orthonormal basis vectors $\mathbf{e}_i$ and coordinates x_i, with i being 1, 2 or 3:

$$\mathbf{r} = x_1\mathbf{e}_1 + x_2\mathbf{e}_2 + x_3\mathbf{e}_3. \tag{2.1}$$

In Chapter 3 we will need the element of arc to derive solutions of Laplace's equation in different coordinate systems. The differential vector $d\mathbf{r}$ is given by the total differential of Eq. 2.1 by

$$d\mathbf{r} = \frac{\partial \mathbf{r}}{\partial x_1}dx_1 + \frac{\partial \mathbf{r}}{\partial x_2}dx_2 + \frac{\partial \mathbf{r}}{\partial x_3}dx_3. \tag{2.2}$$

Please note that the partial differentiations are taken for each component of $\mathbf{r}$ separately. By noting that

$$\frac{\partial \mathbf{r}}{\partial x_i} = \frac{\mathbf{e}_i}{h_i} = \mathbf{e}_i \tag{2.3}$$

and introducing the scale factor h_i

$$h_i = \left\| \frac{\partial \mathbf{r}}{\partial x_i} \right\| \tag{2.4}$$

we can reformulate Eq. 2.2 to the more general form

$$d\mathbf{r} = h_1 dx_1\mathbf{e}_1 + h_2 dx_2\mathbf{e}_2 + h_3 dx_3\mathbf{e}_3. \tag{2.5}$$

The element of arc, often denoted as ds and introduced in squared form, is defined as the sum of the squared elements of $d\mathbf{r}$, which is

$$ds^2 = \langle d\mathbf{r}, d\mathbf{r}\rangle = dx_1^2 + dx_2^2 + dx_3^3. \tag{2.6}$$

It becomes immediately clear, that in case of Cartesian coordinates, the scale factors h_i are equal to unity, because of the orthonormal characteristic of the basis vectors $\mathbf{e}_i$:

$$\mathbf{e}_i^2 = \mathbf{e}_i^\mathsf{T}\mathbf{e}_i = 1. \tag{2.7}$$

The upper index T in the above equation indicates transposition.

2.3. Spherical Coordinates

Spherical coordinates are three-dimensional polar coordinates. The point P in space is uniquely determined within a spherical coordinate system with known origin by one distance and two angular components. Various conventions are used in the literature for symbolic representations of the coordinates and their preferred listing order. We use the following notation:

- r is the Euclidean distance measured from the origin to P.
- ϑ is the polar angle measured from the axis pointing towards zenith to the line connecting the origin and P.
- λ is the azimuthal angle measured on the reference plane from a reference direction to the connecting line in this plane.

This notation is often used in Geoscience, where r is the radius and ϑ and λ are referred to as co-latitude and longitude, respectively. Even more often, the latitude φ is used to describe the vertical polar angle. It is related to ϑ by

$$\varphi = \frac{\pi}{2} - \vartheta. \tag{2.8}$$

The radial component ranges from 0 to ∞, ϑ is defined between 0 and π, λ between 0 and 2π. By fixing one coordinate at a time, one first-order and two second-order surfaces are generated. Constant radial distance yields a sphere centered at the origin. By fixing the co-latitude ϑ the resulting coordinate surface is a one-sheeted singular cone. Finally, the surface $\lambda = const.$ is a half plane cut by the zenith directional axis. The intersection of all three surfaces is one single point.

The spherical coordinates can be determined from the Cartesian by using the following equations

$$\begin{aligned} r &= \sqrt{x_1^2 + x_2^2 + x_3^2}, \\ \vartheta &= \arccos \frac{x_3}{r}, \\ \lambda &= \arctan \frac{x_2}{x_1}. \end{aligned} \tag{2.9}$$

Given the spherical coordinates, the inverse transformation reads

$$\begin{aligned} x_1 &= r \sin\vartheta \cos\lambda, \\ x_2 &= r \sin\vartheta \sin\lambda, \\ x_3 &= r \cos\vartheta. \end{aligned} \tag{2.10}$$

The correspondence is unambiguous when made sure that λ is computed in the correct quadrant. Also, Eqs. 2.9 and 2.10 are only true if both reference systems share the same origin.

In the previous section, the differential vector $d\mathbf{r}$ was introduced in Eq. 2.5. The spherical equivalent leads to

$$d\mathbf{r} = h_1 dr \mathbf{e}_r + h_2 d\vartheta \mathbf{e}_\vartheta + h_3 d\lambda \mathbf{e}_\lambda, \tag{2.11}$$

where the definition of $\mathbf{r}_{(r,\vartheta,\lambda)}$ is analogous to Eq. 2.3. Subsequently, the element of arc is given by

$$ds^2 = h_1^2 dr^2 + h_2^2 d\vartheta^2 + h_3^2 d\lambda^2. \tag{2.12}$$

The scale factors in spherical coordinates can be derived to be

$$\begin{aligned} h_1 &= 1, \\ h_2 &= r, \\ h_3 &= r \sin\vartheta. \end{aligned} \tag{2.13}$$

The squared curvilinear basis vectors are again equal to one due to orthogonality.

2.4. Spheroidal Coordinates

We saw that Cartesian coordinates are fully described by choosing an origin and three orthogonal axes. The definition of the spherical system is based again on the choice of an origin and a unit sphere in which the zenith direction and one reference direction in the plane orthogonal to it must be specified. We now introduce spheroids, also known as ellipsoids of revolution. They are generated when rotating an ellipse about one of its semi-axes. Oblate, from the Latin words *ob* ("towards") and *latus* ("broad, wide"), spheroids are obtained when the axis of rotation is the semi-minor axis of the ellipse. Prolate, from Latin *proferre* ("to stretch, lengthen"), spheroids are hence the result of the revolution about the semi-major axis.

In contrast to the spherical coordinate system, spheroidal coordinates rely on the definition of a reference figure, i.e., a spheroid with specified orientation and eccentricity. We introduce the equation of a tri-axial ellipsoid with the semi-axes a_1, a_2 and a_3 as

$$\frac{x_1^2}{a_1^2} + \frac{x_2^2}{a_2^2} + \frac{x_3^2}{a_3^2} = 1 \tag{2.14}$$

and note that

$$0 < a_3 < a_2 < a_1 < \infty. \tag{2.15}$$

In the oblate case, the two semi-axes a_1 and a_2 are equal and the oblate spheroid is given by

$$\frac{x_1^2 + x_2^2}{a_1^2} + \frac{x_3^2}{a_3^2} = 1. \tag{2.16}$$

The equation of a prolate spheroid, where $a_2 = a_3$, consequently reads

$$\frac{x_1^2 + x_2^2}{a_3^2} + \frac{x_3^2}{a_1^2} = 1. \tag{2.17}$$

When comparing Eqs. 2.16 and 2.17 it becomes clear that the axis of rotation is the same for both cases. This convention facilitates the definition of the coordinate systems described below.

2.4.1. Oblate Case

We introduce oblate (and prolate) coordinates as generalization of spherical coordinates. This system comprises again one component of distance-like characteristic and two angular components.

- u is the semi-minor axis of an ellipsoid of revolution, whose eccentricity is equal to that of the reference spheroid. In other words, the spheroid with the semi-minor axis u and the reference spheroid are confocal, i.e., they share the same foci.
- ζ is the reduced co-latitude, i.e., the complement of the reduced latitude β ($\zeta = \pi/2 - \beta$). It is defined as the angle measured from the axis of rotation to the line connecting the origin and the point P'. To find P', a sphere with radius corresponding to the length of the semi major-axis is inserted on which the point P is projected parallel to the axis of rotation.
- λ is equal to the spherical definition.

The domain in which the three coordinates are defined is the same as before. The surface of constant u is a confocal oblate spheroid, that of constant ζ is a confocal one-sheeted hyperboloid of revolution. The coordinate surface of λ is again a half plane.

According to Thong and Grafarend (1989), the relation to the Cartesian coordinates can be established by

$$\begin{aligned} u &= \sqrt{\frac{A_o}{2} + B_o}, \\ \zeta &= \arccos \frac{x_3}{u}, \\ \lambda &= \arctan \frac{x_2}{x_1}, \end{aligned} \tag{2.18}$$

with the auxiliary terms

$$\begin{aligned} A_o &= x_1^2 + x_2^2 + x_3^2 - E^2, \\ B_o &= \sqrt{\frac{1}{4}A_o^2 + E^2 x_3^2}, \end{aligned} \tag{2.19}$$

where the subscript o indicates oblate and E is the constant linear eccentricity defined as

$$E = \sqrt{a_1^2 - a_3^2}. \tag{2.20}$$

The inverse transformation is

$$\begin{aligned} x_1 &= \sqrt{u^2 + E^2}\sin\zeta\cos\lambda, \\ x_2 &= \sqrt{u^2 + E^2}\sin\zeta\sin\lambda, \\ x_3 &= u\cos\zeta. \end{aligned} \tag{2.21}$$

We can now proceed analogously to Section 2.3 and write the element of arc as

$$ds^2 = h_1^2 du^2 + h_2^2 d\zeta^2 + h_3^2 d\lambda^2 \tag{2.22}$$

with the scale factors

$$\begin{aligned} h_1 &= \sqrt{\frac{u^2 + E^2\cos^2\zeta}{u^2 + E^2}}, \\ h_2 &= \sqrt{u^2 + E^2\cos^2\zeta}, \\ h_3 &= \sqrt{(u^2 + E^2)\sin^2\zeta}. \end{aligned} \tag{2.23}$$

The angular coordinate ζ is usually represented by the Greek letter ϑ. However, to distinguish it from the spherical counterpart, a different letter is chosen. The longitude λ is identical to the spherical case.

2.4.2. Prolate Case

The three prolate coordinates are obtained by slight modifications of the oblate case:

- v is the semi-major axis of a confocal prolate spheroid.
- κ is the reduced co-latitude in the prolate case.
- λ remains unchanged too.

The coordinate surfaces of v are consequently confocal prolate spheroids. In analogy to the oblate case and according to Fukushima (2014), we find

$$\begin{aligned} v &= \sqrt{\frac{A_p}{2} + B_p}, \\ \kappa &= \arccos \frac{x_3}{v}, \\ \lambda &= \arctan \frac{x_2}{x_1}, \end{aligned} \tag{2.24}$$

with the subscript p indicating the prolate case of the auxiliary terms

$$\begin{aligned} A_p &= x_1^2 + x_2^2 + x_3^2 + E^2, \\ B_p &= \sqrt{\frac{1}{4} A_p^2 - E^2 x_3^2} \end{aligned} \tag{2.25}$$

The definition of E does not change. Inversely, the Cartesian coordinates are obtained via

$$\begin{aligned} x_1 &= \sqrt{v^2 - E^2} \sin\kappa \cos\lambda, \\ x_2 &= \sqrt{v^2 - E^2} \sin\kappa \sin\lambda, \\ x_3 &= v \cos\kappa. \end{aligned} \tag{2.26}$$

The element of arc in this system reads

$$ds^2 = h_1^2 dv^2 + h_2^2 d\kappa^2 + h_3^2 d\lambda^2 \tag{2.27}$$

with

$$\begin{aligned} h_1 &= \sqrt{\frac{v^2 - E^2 \cos^2\kappa}{v^2 - E^2}}, \\ h_2 &= \sqrt{v^2 - E^2 \cos^2\kappa}, \\ h_3 &= \sqrt{(v^2 - E^2) \sin^2\kappa}. \end{aligned} \tag{2.28}$$

The reduced co-latitude is again denoted by a different Greek letter κ in order to enhance distinctness.

2.5. Ellipsoidal Coordinates

Spheroids were stated to be generalizations of spheres. Now, we go one step further and generalize spheroids to tri-axial ellipsoids. We recall Eq. 2.14, which we extend by a new parameter q to

$$\frac{x_1^2}{a_1^2 - q} + \frac{x_2^2}{a_2^2 - q} + \frac{x_3^2}{a_3^2 - q} = 1. \tag{2.29}$$

This equation represents a polynomial of degree three in q. It can be shown that there exist three real roots $q_i, i = 1, 2, 3$, defined within the domain

$$-\infty < q_3 < a_3^2 < q_2 < a_2^2 < q_1 < a_1^2. \tag{2.30}$$

Each of them represents one family of confocal, second-degree surfaces, which are ellipsoids, one-sheeted and two-sheeted hyperboloids for q_3, q_2 and q_1, respectively (Dassios, 2012). At this point, we can introduce the ellipsoidal coordinates.

- $\rho = \sqrt{a_1^2 - q_3}$ corresponds to the radial component of the previous systems forming the family of ellipsoids,
- $\mu = \sqrt{a_1^2 - q_2}$ represents the one-sheeted hyperboloids,
- $\nu = \sqrt{a_1^2 - q_1}$ the two-sheeted hyperboloids.

The latter two correspond to the angular coordinates of the sphere, although their physical dimension is a distance. We introduce the semi-focal distances

$$k_1^2 = a_2^2 - a_3^2, \quad k_2^2 = a_1^2 - a_3^2, \quad k_3^2 = a_1^2 - a_2^2 \tag{2.31}$$

and conclude that

$$0 \leq \nu^2 \leq k_3^2 \leq \mu^2 \leq k_2^2 \leq \rho^2 < \infty. \tag{2.32}$$

By expressing the roots $q_i, i = 1, 2, 3$, explicitly in the relations defining the three coordinates and inserting them into Eq. 2.29 we find three equations which determine the respective coordinate surface:

$$\begin{aligned}
\frac{x_1^2}{\rho^2} + \frac{x_2^2}{\rho^2 - k_3^2} + \frac{x_3^2}{\rho^2 - k_2^2} &= 1, \\
\frac{x_1^2}{\mu^2} + \frac{x_2^2}{\mu^2 - k_3^2} + \frac{x_3^2}{\mu^2 - k_2^2} &= 1, \\
\frac{x_1^2}{\nu^2} + \frac{x_2^2}{\nu^2 - k_3^2} + \frac{x_3^2}{\nu^2 - k_2^2} &= 1.
\end{aligned} \tag{2.33}$$

According to Garmier and Barriot (2001), the solutions to the equations seen above and, thus, the explicit relation to Cartesian cordinates, are given by

$$\begin{aligned}
\rho^2 &= 2\sqrt{W}\cos\left(\frac{\alpha}{3}\right) - \frac{c_1}{3}, \\
\mu^2 &= 2\sqrt{W}\cos\left(\frac{\alpha + 4\pi}{3}\right) - \frac{c_1}{3}, \\
\nu^2 &= 2\sqrt{W}\cos\left(\frac{\alpha + 2\pi}{3}\right) - \frac{c_1}{3}
\end{aligned} \tag{2.34}$$

with

$$\begin{aligned} W &= \frac{c_1^2 - 3c_2}{9}, \\ R &= \frac{9c_1c_2 - 27c_3 - 2c_1^3}{54}, \\ \cos\alpha &= \frac{R}{\sqrt{W^3}}, \\ c_1 &= -\left(x_1^2 + x_2^2 + x_3^2 + k_2^2 + k_3^2\right), \\ c_2 &= x_1^2\left(k_2^2 + k_3^2\right) + x_2^2k_2^2 + x_3^2k_3^2 + k_2^2k_3^2, \\ c_3 &= -x_1^2k_2^2k_3^2. \end{aligned} \tag{2.35}$$

Given the ellipsoidal coordinates, the Cartesians are obtained via

$$\begin{aligned} x_1^2 &= \frac{\rho^2\mu^2\nu^2}{k_2^2k_3^2}, \\ x_2^2 &= \frac{\left(\rho^2 - k_3^2\right)\left(\mu^2 - k_3^2\right)\left(k_3^2 - \nu^2\right)}{k_3^2\left(k_2^2 - k_3^2\right)}, \\ x_3^2 &= \frac{\left(\rho^2 - k_2^2\right)\left(k_2^2 - \mu^2\right)\left(k_2^2 - \nu^2\right)}{k_2^2\left(k_2^2 - k_3^2\right)}. \end{aligned} \tag{2.36}$$

We see that the relation between the two coordinate systems is ambiguous, which is clear from Eqs. 2.34 and 2.36. One triplet of ellipsoidal coordinates can represent eight different points in the Cartesian system, each of which located in one octant. Various methods have been suggested to avoid the sign ambiguities to establish a one-to-one relation (cf. Bardhan and Knepley (2012); Panou (2014)). In this text, we refrain from dealing with this issue and claim that the inverse transformation into the Cartesian system is rarely needed. Also, this unpleasant problem will not cause any troubles when it comes to the computation of ellipsoidal harmonics, as we will see later.

We finalize this chapter with the introduction of the element of arc in ellipsoidal coordinates:

$$ds^2 = h_1^2d\rho^2 + h_2^2d\mu^2 + h_3^2d\nu^2. \tag{2.37}$$

The scale factors can derived to be (Dassios, 2012, Eq. 1.59-1.61)

$$\begin{aligned} h_1 &= \frac{\sqrt{\rho^2 - \mu^2}\sqrt{\rho^2 - \nu^2}}{\sqrt{\rho^2 - k_2^2}\sqrt{\rho^2 - k_3^2}}, \\ h_2 &= \frac{\sqrt{\rho^2 - \mu^2}\sqrt{\mu^2 - \nu^2}}{\sqrt{k_2^2 - \mu^2}\sqrt{\mu^2 - k_3^2}}, \\ h_3 &= \frac{\sqrt{\rho^2 - \nu^2}\sqrt{\mu^2 - \nu^2}}{\sqrt{k_3^2 - \nu^2}\sqrt{k_2^2 - \nu^2}}. \end{aligned} \tag{2.38}$$

Chapter 3.

Gravity Field Parametrization

3.1. Gravity and Gravitation

One tends to be a little sloppy when speaking of gravity by using the terms gravity and gravitation synonymously. In fact, in Physical Geodesy gravity is defined as the total contribution of gravitational and centrifugal force, caused by the rotation of the attracting body. Centrifugal force is known and its effects can always be added to the gravitational one. Therefore, we concentrate on the determination of gravitation. To avoid confusion it shall be mentioned that throughout this text we speak of gravitation, even if we use the term gravity sometimes.

3.2. The Law of Gravitation

Newton's fundamental law of gravitation states that two particles attract each other with a force dependent on their masses ($m_{(1,2)}$) and the squared distance separating them (l_{12}^2). This gravitational force is a three-dimensional vector whose direction coincides with the line connecting the point masses (Sansò and Sideris, 2013). This is expressed by the unit vector $\hat{\mathbf{r}}_{12}$.

$$\mathbf{g}_{12} = -\frac{Gm_1m_2}{l_{12}^2}\hat{\mathbf{r}}_{12} = -\frac{Gm_1m_2}{l_{12}^2}\frac{\mathbf{r}_{12}}{l_{12}} = -\frac{Gm_1m_2}{l_{12}^3}\mathbf{r}_{12}. \tag{3.1}$$

The proportionality factor G is the universal gravitational constant. It was introduced by Newton but first estimated many years after his death. It is an empirically determined constant and the refinement of its value is an ongoing process. The best actual estimate for its value is $G = 6.673\,84(80) \times 10^{-11}\,\mathrm{m^3kg^{-1}s^{-2}}$ (The NIST Reference On Constants Units and Uncertainty, 2014). It is evident by looking at Eq. 3.1 that the gravitational force decreases with increasing spacing between the attracting points and vanishes at infinity.

Let us assume that one mass is incomparably larger than the other, so that the attraction is really significant only in one direction. This allows us to simplify Eq. 3.1. We neglect m_2 and introduce the dominant mass as M, which yields

$$\mathbf{g}_{12} = -\frac{GM}{l_{12}^3}\mathbf{r}_{12}. \tag{3.2}$$

Now let us further assume that M no longer describes a single point in space, but represents the total mass of an agglomeration of point masses

$$M = \sum_i m_i. \tag{3.3}$$

This allows for the determination of the gravitational *field* exerted by M on a point P_j, given by

$$\mathbf{g}_j = -\sum_i \frac{Gm_i}{l_{ij}^3}\mathbf{r}_{ij}. \tag{3.4}$$

Eq. 3.4 is the basic equation of the so-called "mascon" (mass concentration) approach sometimes used for gravity field modeling. In its entirety, the individual point masses m_i represent the whole body, whose attraction is to be determined. By introducing the density as the ratio of the differential mass and the differential volume $\rho = dm/dv$ we are able to generalize the above equation for a solid body as

$$\mathbf{g}_j = -G \iiint_v \frac{\mathbf{r}_{ij}}{l_{ij}^3}\rho_i dv_i. \tag{3.5}$$

The force vector $\mathbf{g}_j$ is expressed in a three-dimensional coordinate system, consequently the element of volume dv is given by

$$dv = dx_1 dx_2 dx_3, \tag{3.6}$$

where x_i are the coordinates of the masses dm (Hofmann-Wellenhof and Moritz, 2006). The triple integral in Eq. 3.5 is hence explained by Eq. 3.6.

3.3. Potential Theory

The gravitational force is conservative and meets the following conditions:

- A potential function exists.
- Work is path-independent and the integral along a closed curve vanishes.
- The force field is irrotational.

All conditions are equivalent. This concept is used to express the vector $\mathbf{g}$ as the gradient of the scalar potential function V,

$$\mathbf{g} = \nabla V, \tag{3.7}$$

where the gradient operator ∇ describes the differentiation of the potential V w.r.t. the coordinates. In Cartesian coordinates, this relation reads

$$\mathbf{g}\left(x_1, x_2, x_3\right) = \nabla V\left(x_1, x_2, x_3\right) = \mathbf{e}_1 \frac{\partial V}{\partial x_1} + \mathbf{e}_2 \frac{\partial V}{\partial x_2} + \mathbf{e}_3 \frac{\partial V}{\partial x_3}, \tag{3.8}$$

with the basis vectors $\mathbf{e}_i$ of the orthonormal coordinate system. The potential V of a solid body can be determined in accordance with Eq. 3.5 by

$$V_j = G \iiint_v \frac{\rho_i}{l_{ij}} dv_i. \tag{3.9}$$

The potential V, from a physical point of view, is defined as the work needed to transport a particle from infinity ($V = 0$) to the field point P_j.

Apart from its conservative characteristics, the gravitational force and potential can shown to be continuously differentiable throughout space (Hofmann-Wellenhof and Moritz, 2006). Outside the attracting masses, the sum of the second derivatives vanishes:

$$\Delta V = 0. \tag{3.10}$$

In Eq. 3.10 a new operator called Laplace operator Δ was introduced. It is the short-hand notation for the divergence of the gradient of a function, which in Cartesian coordinates, it reads

$$\Delta = \nabla \cdot \nabla = \frac{\partial^2}{\partial x_1^2} + \frac{\partial^2}{\partial x_2^2} + \frac{\partial^2}{\partial x_3^2}. \tag{3.11}$$

Eq. 3.10 is Laplace's equation and is of fundamental importance in Physical Geodesy. Its significance lies in the fact that solutions of Laplace's equation are harmonic functions, which can be developed into harmonic series. This is the basis of what will shown in the following section.

As stated before, the potential satisfies Laplace's equation *outside* the attracting masses. In the interior, however, the second derivatives of the potential show discontinuities which are related to density variations (Sansò and Sideris, 2013). The corresponding equation in the inside is called Poisson's equation and satisfies

$$\Delta V = -4\pi G\rho. \tag{3.12}$$

Consequently, the gravitational potential is not a harmonic function inside the attracting masses.

3.4. Solutions to Laplace's Equation

In the previous section we introduced Laplace's equation as one of the most important mathematical relations in geodesy. It is the foundation on which gravity field recovery techniques are based upon. Technically, it represents a second order partial differential equation, which from a mathematical point of view is obviously more challenging to solve than Eq. 3.9. However, it is possible to find suitable solutions which no longer rely on the knowledge of the density distribution inside the body and are hence attractive for usage in Satellite Geodesy, for instance. This following very simplified "recipe" shall provide a first coarse overview of the solution technique. More details will be given in Subsections 3.4.1-3.4.4 for different types of curvilinear coordinates.

For an arbitrary curvilinear and orthogonal reference system with coordinates ξ_1, ξ_2, ξ_3 the Laplace equation is expressed by (Dassios, 2012)

$$\Delta V = \frac{1}{h_1 h_2 h_3}\left[\frac{\partial}{\partial \xi_1}\left(\frac{h_2 h_3}{h_1}\frac{\partial V}{\partial \xi_1}\right) + \frac{\partial}{\partial \xi_2}\left(\frac{h_1 h_3}{h_2}\frac{\partial V}{\partial \xi_2}\right) + \frac{\partial}{\partial \xi_3}\left(\frac{h_1 h_2}{h_3}\frac{\partial V}{\partial \xi_3}\right)\right] = 0, \quad (3.13)$$

where h_i are scale factors as introduced in Chapter 2. By using the method of separation of variables we can decompose this equation into three ordinary differential equations (ODE) and write

$$V(\xi_1, \xi_2, \xi_3) = f(\xi_1)\, g(\xi_2)\, h(\xi_3). \quad (3.14)$$

The essence of this idea is the fact that we now have three functions which depend on the respective coordinate ξ_i only. The solution for V emerges to be the sum of individual partial solutions V_n, where n indicates the summation index. Put differently, V can be represented by a series expansion of the form

$$V = \sum_{n=0}^{\infty} V_n, \quad V_n = f_n g_n h_n. \quad (3.15)$$

For the sake of simplicity we dropped the dependencies on the coordinates in the equations above. We will now be concerned with finding suitable functions in different parametrizations which satisfy Eq. 3.15. Table 3.1 provides a first, compact overview of those for the exterior case.

3.4.1. Spherical Harmonics

In spherical coordinates, Laplace's equation becomes

$$r^2\frac{\partial^2 V}{\partial r^2} + 2r\frac{\partial V}{\partial r} + \frac{\partial^2 V}{\partial \vartheta^2} + \cot\vartheta\frac{\partial V}{\partial \vartheta} + \frac{1}{\sin^2\vartheta}\frac{\partial^2 V}{\partial \lambda^2} = 0, \quad (3.16)$$

(ξ_1, ξ_2, ξ_3)	f_n	g_n	h_n
(r, ϑ, λ)	$r^{-(n+1)}$	$P_n^m(\cos\vartheta)$	$e^{\pm im\lambda}$
(u, ζ, λ)	$Q_n^m(iu/E)$	$P_n^m(\cos\zeta)$	$e^{\pm im\lambda}$
(v, κ, λ)	$Q_n^m(iv/E)$	$P_n^m(\cos\kappa)$	$e^{\pm im\lambda}$
(ρ, μ, ν)	$F_n^p(\rho)$	$E_n^p(\mu)$	$E_n^p(\nu)$

Table 3.1.: Exterior solutions to Laplace's equation in different parametrizations. P_n^m and Q_n^m are the associated Legendre functions of the first and second kind, respectively. E_n^p and F_n^p are the two kinds of Lamé functions. The coordinates are according to the reference systems described in Chapter 2.

which is obtained by substituting Eq. 2.13 into Eq. 3.13. The process of separating the variables yields three ordinary differential equations (Hofmann-Wellenhof and Moritz, 2006)

$$\begin{aligned} \frac{d}{dr}\left(r^2\frac{d}{dr}f(r)\right) - n(n+1)f(r) &= 0, \\ \frac{1}{\sin\vartheta}\frac{d}{d\vartheta}\left(\sin\vartheta\frac{d}{d\vartheta}\right)g(\vartheta) + \left(n(n+1) - \frac{m^2}{\sin^2\vartheta}\right)g(\vartheta) &= 0, \\ \frac{d^2}{d\lambda^2}h(\lambda) + m^2 h(\lambda) &= 0. \end{aligned} \tag{3.17}$$

An additional (integer) constant m turns up, whose definition range is $|m| \leq n$. Solutions to the first equation in Eq. 3.17 are r^n and $r^{-(n+1)}$. The former expresses solutions to functions that are harmonic *inside* a reference sphere (interior solutions), whereas the latter to those *outside* a reference sphere (exterior solutions). Since the gravitational potential is harmonic only outside the attracting masses (c.f. Eqs. 3.10 and 3.12), the exterior solutions are the ones we seek. Before dealing with the second differential equation, the group of solutions $e^{\pm im\lambda}$ to the last ODE in Eq. 3.17 is stated, with $i = \sqrt{-1}$. Since positive values for m are used more often in geodetic literature, the corresponding solutions $\cos(m\lambda)$ and $\sin(m\lambda)$ shall be given here too. We now concentrate on the second ODE in Eq. 3.17. As proven by many authors (e.g., Hobson (1931)) this equation may be transformed to the associated Legendre differential equation by applying the substitution $t = \cos\vartheta$:

$$\left(1-t^2\right)\frac{d^2}{dt^2}P_n^m(t) - 2t\frac{d}{dt}P_n^m(t) + \left(n(n+1) - \frac{m^2}{1-t^2}\right)P_n^m(t) = 0. \tag{3.18}$$

Two independent solutions of Eq. 3.18 are the associated Legendre functions of the first kind

$$P_n^m(t) = \left(1-t^2\right)^{\frac{m}{2}}\frac{d^m}{dt^m}P_n(t), \tag{3.19}$$

and the associated Legendre functions of the second kind

$$Q_n^m(t) = \left(1 - t^2\right)^{\frac{m}{2}} \frac{d^m}{dt^m} Q_n(t), \tag{3.20}$$

where $P_n(t)$ and $Q_n(t)$ are the Legendre polynomials of the first and second kind, respectively. It can be shown, that division by zero occurs when computing Q_n using the substitution $t = \cos\vartheta$ mentioned earlier (Hofmann-Wellenhof and Moritz, 2006). Hence, the functions of the second kind rule out for the spherical parametrization. The functions $P_n^m(t)$ can easily be determined using recurrence relations (see Chapter 4).

Inserting the solutions of the three ODEs in 3.17 into Eq. 3.15 yields

$$V(r, \vartheta, \lambda) = \sum_{n=0}^{\infty} \sum_{m=0}^{n} \frac{1}{r^{n+1}} P_{nm}(\cos\vartheta) \left[c_{nm} \cos m\lambda + s_{nm} \sin m\lambda\right]. \tag{3.21}$$

The summation integer n is usually referred to as degree and m as order of the series expansion. The constants c_{nm} and s_{nm} are called the coefficients of the series. They describe the characteristics of the potential function V and are hence the object of desire when it comes to gravitational field modeling. A different representation is commonly used, which reads

$$V(r, \vartheta, \lambda) = \frac{GM}{R} \sum_{n=0}^{\infty} \sum_{m=0}^{n} \left(\frac{R}{r}\right)^{n+1} P_{nm}(\cos\vartheta) \left[c_{nm} \cos m\lambda + s_{nm} \sin m\lambda\right], \tag{3.22}$$

with R being the radius of the best fitting reference sphere and GM the constant described in the beginning of this chapter. The advantage of reformulating the series this way, lies in the fact that the coefficients are now unit-less and refer to the surface of the reference sphere.

3.4.2. Oblate Spheroidal Harmonics

To find the solutions of Laplace's equation in oblate coordinates we proceed in the same way as in the spherical case and plug the scale factors 2.23 into Eq. 3.13, which eventually results in

$$\left(u^2 + E^2\right) \frac{\partial^2 V}{\partial u^2} + 2u \frac{\partial V}{\partial u} + \frac{\partial^2 V}{\partial \zeta^2} + \cot\zeta \frac{\partial V}{\partial \zeta} + \frac{u^2 + E^2 \cos^2\zeta}{(u^2 + E^2)\sin^2\zeta} \frac{\partial^2 V}{\partial \lambda^2} = 0. \tag{3.23}$$

Decomposition into three ODEs yields

$$\begin{aligned} \frac{d}{du}\left(\left(u^2+E^2\right)\frac{d}{du}f\left(u\right)\right)-\left[n\left(n+1\right)-\frac{E^2}{u^2+E^2}m^2\right]f\left(u\right)=0,\\ \frac{1}{\sin\zeta}\frac{d}{d\zeta}\left(\sin\zeta\frac{d}{d\zeta}\right)g\left(\zeta\right)+\left(n\left(n+1\right)-\frac{m^2}{\sin^2\zeta}\right)g\left(\zeta\right)=0,\\ \frac{d^2}{d\lambda^2}h\left(\lambda\right)+m^2h\left(\lambda\right)=0. \end{aligned} \tag{3.24}$$

By comparing Eq. 3.24 with Eq. 3.13 it becomes obvious that only the first of the three equations differs from the spherical case. By introducing another substitution variable,

$$\tau=i\frac{u}{E}, \tag{3.25}$$

the first ODE is transformed to

$$\left(1-\tau^2\right)\frac{d^2}{d\tau^2}P_n^m\left(\tau\right)-2\tau\frac{d}{d\tau}P_n^m\left(\tau\right)+\left(n\left(n+1\right)-\frac{m^2}{1-\tau^2}\right)P_n^m\left(\tau\right)=0, \tag{3.26}$$

which is again a form of the associated Legendre differential equation. As a matter of fact, both kinds of Legendre functions (Eqs. 3.19 and 3.20) are valid solutions when choosing the substitution variable τ. As stated in Hobson (1931), $P_n^m\left(\tau\right)$ represent the interior solution while $Q_n^m\left(\tau\right)$ are the preferred exterior solutions. The computation of the Legendre functions of the second kind is seen less often in literature, an effective algorithm suggested by Fukushima (2013) will be presented in Chapter 4.

To avoid complex solutions, the gravitational potential is written in the form

$$V\left(u,\zeta,\lambda\right)=\frac{GM}{a_1}\sum_{n=0}^{\infty}\sum_{m=0}^{n}q_{nm}\left(x\right)P_{nm}\left(\cos\zeta\right)\left[c_{nm}\cos m\lambda+s_{nm}\sin m\lambda\right], \tag{3.27}$$

where

$$q_{nm}\left(x\right)=\frac{Q_{nm}\left(ix\right)}{Q_{nm}\left(ix_0\right)}, \tag{3.28}$$

is the fraction of two associated Legendre functions, one of them being constant w.r.t. the reference spheroid,

$$x=\frac{u}{E},\qquad x_0=\frac{a_3}{E}, \tag{3.29}$$

with a_1 and a_3 being its semi-axes (cf. Eq. 2.15).

3.4.3. Prolate Spheroidal Harmonics

Laplace's equation in prolate spheroidal parametrization reads (Meixner and Schäfke, 1954)

$$\left(v^2 - E^2\right) \frac{\partial^2 V}{\partial v^2} + 2v \frac{\partial V}{\partial v} + \frac{\partial^2 V}{\partial \kappa^2} + \cot \kappa \frac{\partial V}{\partial \kappa} + \frac{v^2 - E^2 \cos^2 \kappa}{\left(v^2 - E^2\right) \sin^2 \kappa} \frac{\partial^2 V}{\partial \lambda^2} = 0. \tag{3.30}$$

By looking at the results of the separation approach,

$$\begin{aligned} \frac{d}{dv}\left(\left(v^2 - E^2\right) \frac{d}{dv} f\left(v\right)\right) - \left[n\left(n+1\right) + \frac{E^2}{v^2 - E^2} m^2\right] f\left(v\right) = 0, \\ \frac{1}{\sin \kappa} \frac{d}{d\kappa}\left(\sin \kappa \frac{d}{d\kappa}\right) g\left(\kappa\right) + \left(n\left(n+1\right) - \frac{m^2}{\sin^2 \kappa}\right) g\left(\kappa\right) = 0, \\ \frac{d^2}{d\lambda^2} h\left(\lambda\right) + m^2 h\left(\lambda\right) = 0. \end{aligned} \tag{3.31}$$

we see at once the similarity to the oblate case. With the knowledge we gained from the previous sections it is trivial to apply the already well-known substitution to the first ODE using the slightly modified substitution variable $\tau = iv/E$. Thus, the gravitational potential in the prolate parametrization is given by

$$V\left(v, \kappa, \lambda\right) = \frac{GM}{a_1} \sum_{n=0}^{\infty} \sum_{m=0}^{n} q_{nm}\left(y\right) P_{nm}\left(\cos \kappa\right) \left[c_{nm} \cos m\lambda + s_{nm} \sin m\lambda\right], \tag{3.32}$$

with the modified fractional term

$$q_{nm}\left(y\right) = \frac{Q_{nm}\left(iy\right)}{Q_{nm}\left(iy_0\right)}, \tag{3.33}$$

where

$$y = \frac{v}{E}, \qquad y_0 = \frac{a_1}{E}. \tag{3.34}$$

We see that oblate and prolate spheroidal harmonics are strongly connected. In both cases, associated Legendre functions of the second kind play the corresponding part to the radial attenuation factor in the spherical case.

3.4.4. Ellipsoidal Harmonics

The ellipsoidal representation of Laplace's equation is more complex compared to the spherical and spheroidal cases. Substitution of the scale factors 2.38 into Eq. 3.13 yields (Dassios, 2012)

$$\begin{aligned}
&\frac{1}{(\rho^2-\mu^2)(\rho^2-\nu^2)}\left(\sqrt{\rho^2-k_3^2}\sqrt{\rho^2-k_2^2}\frac{\partial V}{\partial \rho}\right)\left(\sqrt{\rho^2-k_3^2}\sqrt{\rho^2-k_2^2}\frac{\partial V}{\partial \rho}\right)\\
+&\frac{1}{(\rho^2-\mu^2)(\mu^2-\nu^2)}\left(\sqrt{\mu^2-k_3^2}\sqrt{k_2^2-\mu^2}\frac{\partial V}{\partial \mu}\right)\left(\sqrt{\mu^2-k_3^2}\sqrt{k_2^2-\mu^2}\frac{\partial V}{\partial \mu}\right)\\
+&\frac{1}{(\rho^2-\nu^2)(\mu^2-\nu^2)}\left(\sqrt{k_3^2-\nu^2}\sqrt{k_2^2-\nu^2}\frac{\partial V}{\partial \nu}\right)\left(\sqrt{k_3^2-\nu^2}\sqrt{k_2^2-\nu^2}\frac{\partial V}{\partial \nu}\right)=0.
\end{aligned} \tag{3.35}$$

We can simplify this relation by introducing the so-called thermometric parameters[1] ξ, η, ζ, each of which is a function of one ellipsoidal coordinate,

$$\begin{aligned}
\xi(\rho) &= \int_{k_2}^{\rho} \frac{dt}{\sqrt{t^2-k_3^2}\sqrt{t^2-k_2^2}},\\
\eta(\mu) &= \int_{k_3}^{\mu} \frac{dt}{\sqrt{t^2-k_3^2}\sqrt{k_2^2-t^2}},\\
\zeta(\nu) &= \int_{0}^{\nu} \frac{dt}{\sqrt{k_3^2-t^2}\sqrt{k_2^2-t^2}},
\end{aligned} \tag{3.36}$$

so that the Laplace equation takes the form

$$\left(\mu^2-\nu^2\right)\frac{\partial^2 V}{\partial \xi^2}+\left(\rho^2-\nu^2\right)\frac{\partial^2 V}{\partial \eta^2}+\left(\rho^2-\mu^2\right)\frac{\partial^2 V}{\partial \zeta^2}=0. \tag{3.37}$$

The approach of separating the variables in order to obtain ODEs is not straightforward. This is because each of the addends in Eq. 3.37 involves all three ellipsoidal coordinates. Without going into detail, the French mathematician Gabriel Lamé proved that by introducing the two separation constants A and B and making use of several geometrical

[1] This term was introduced by Lamé while studying temperature distribution inside ellipsoids (Dassios, 2012). The parameter ζ must not be confused with the oblate coordinate denoted by the same symbol.

identities, decomposition into the following three ODEs is possible (Dassios, 2012):

$$\begin{aligned}
\left(\rho^2-k_3^2\right)\left(\rho^2-k_2^2\right)\frac{d^2f\left(\rho\right)}{d\rho^2}+\rho\left(2\rho^2-k_3^2-k_2^2\right)\frac{df\left(\rho\right)}{d\rho}+\left(A\rho^2+B\right)f\left(\rho\right)=0,\\
\left(\mu^2-k_3^2\right)\left(\mu^2-k_2^2\right)\frac{d^2g\left(\mu\right)}{d\mu^2}+\mu\left(2\mu^2-k_3^2-k_2^2\right)\frac{dg\left(\mu\right)}{d\mu}+\left(A\mu^2+B\right)g\left(\mu\right)=0,\\
\left(\nu^2-k_3^2\right)\left(\nu^2-k_2^2\right)\frac{d^2h\left(\nu\right)}{d\nu^2}+\nu\left(2\nu^2-k_3^2-k_2^2\right)\frac{dh\left(\nu\right)}{d\nu}+\left(A\nu^2+B\right)h\left(\nu\right)=0.
\end{aligned} \tag{3.38}$$

It is easily seen that all equations in 3.38 follow the same structure with different ranges of definition (cf. Eq. 2.32). We can thus subsume them into

$$\begin{aligned}
\left(w^2-k_3^2\right)\left(w^2-k_2^2\right)\frac{d^2E\left(w\right)}{dx^2}+w\left(2x^2-k_3^2-k_2^2\right)\frac{dE\left(w\right)}{dx}-\\
-\left(n\left(n+1\right)w^2-\left(k_2^2+k_3^2\right)p\right)E\left(w\right)\ =0,
\end{aligned} \tag{3.39}$$

where the variable w takes the place of any of the three coordinates and the separation constants A and B have been replaced by $-n\left(n+1\right)$ and $\left(k_2^2+k_3^2\right)p$, respectively. The new constant p takes values within the range of $1\leq p\leq 2n+1$. Eq. 3.39 is called Lamé's equation and its solutions are the Lamé functions of the first kind $E_n^p\left(w\right)$ and those of the second kind $F_n^p\left(w\right)$.

When expressing the Lamé functions in terms of harmonic polynomials, four classes of real functions are obtained (Hobson, 1931). These classes are usually abbreviated with $\mathcal{K},\mathcal{L},\mathcal{M},\mathcal{N}$ and are given by

$$\begin{aligned}
\mathcal{K}&=\left\{P\left(w\right)\right\},\\
\mathcal{L}&=\left\{\sqrt{\left|w^2-k_3^2\right|}P\left(w\right)\right\},\\
\mathcal{M}&=\left\{\sqrt{\left|w^2-k_2^2\right|}P\left(w\right)\right\},\\
\mathcal{N}&=\left\{\sqrt{\left|w^2-k_2^2\right|}\sqrt{\left|w^2-k_3^2\right|}P\left(w\right)\right\}.
\end{aligned} \tag{3.40}$$

with $P\left(w\right)$ being a polynomial of the form

$$P\left(w\right)=P_n\left(w\right)=\sum_k a_k w^{n-2k}. \tag{3.41}$$

In the following chapter the practical implementation of the Lamé functions will be shown, which includes the explanation of when to use which class $\mathcal{K},\mathcal{L},\mathcal{M}$ or $\mathcal{N}$.

In order to model the gravitational potential by means of ellipsoidal harmonics we need Lamé functions of the second kind, which are regular outside the reference ellipsoid. They

are used to represent the upward continuation of the potential. The general solution reads

$$F(w) = E(w) \int_{w_0}^{w} \frac{dt}{[E(t)]^2 \sqrt{t^2 - k_2^2}\sqrt{t^2 - k_3^2}}, \tag{3.42}$$

and depends on the Lamé functions of the first kind. In Chapter 2 we mentioned that ρ represents the radial coordinate in the ellipsoidal reference system. Thus, we will only be concerned with functions of the type $F(\rho)$. A normalized form of this function is given by

$$F(\rho) = F_n(\rho) = (2n+1) E_n(\rho) \int_{\rho}^{\infty} \frac{dt}{[E(t)]^2 \sqrt{t^2 - k_2^2}\sqrt{t^2 - k_3^2}}. \tag{3.43}$$

Finally, the gravitational potential may be expressed by regarding Eq. 3.15 in a similar fashion to the spheroidal harmonics, namely by

$$V(\rho, \mu, \nu) = GM \sum_{n=0}^{\infty} \sum_{p=1}^{2n+1} \alpha_n^p \frac{F_n^p(\rho)}{F_n^p(a_1)} E_n^p(\mu) E_n^p(\nu). \tag{3.44}$$

Herein, the constants α_n^p are the ellipsoidal counterpart to the spherical and spheroidal coefficients c_{nm} and s_{nm}. For a thorough treatment of ellipsoidal harmonics we refer the reader to Hobson (1931) and Dassios (2012).

Chapter 4.

Computation of Basis Functions

In this chapter we will look more closely at the basis functions of the spherical, spheroidal and ellipsoidal harmonic series. We summarize without proofs the relevant formulas to effectively compute these functions and their first derivatives. The latter are required when determining gravitational field coefficients from observations involving the first derivative of the potential, i.e., the gravitational acceleration (vector).

4.1. Legendre Functions of the First Kind

We will keep this section very short, since the equations below are well-known and are easily found in the literature (e.g., (Colombo, 1981)). We follow the notation of Holmes and Featherstone (2002) to compute fully normalized associated Legendre functions (ALF) of the first kind using a degree-wise recursive algorithm. The recursion formula

$$P_{nm}(t) = a_{nm} t P_{n-1,m}(t) - b_{nm} P_{n-2,m}(t), \tag{4.1}$$

with $t = \cos\vartheta$ being the substitution variable introduced in 3.4.1, is used to compute zonal (i.e., $m = 0$) and tesseral (i.e., $0 < m < n$) ALFs. The two auxiliary variables a_{nm} and b_{nm} are functions depending solely on the degree n and the order m. They can be determined by

$$\begin{aligned} a_{nm} &= \sqrt{\frac{(2n-1)(2n+1)}{(n-m)(n+m)}}, \\ b_{nm} &= \sqrt{\frac{(2n+1)(n+m-1)(n-m-1)}{(n-m)(n+m)}}. \end{aligned} \tag{4.2}$$

The relation

$$P_{mm}(t) = s\sqrt{\frac{2m+1}{2m}} P_{m-1,m-1}(t) \tag{4.3}$$

is used to compute the sectoral (i.e., $n = m$) ALFs. Please note that our notation slightly differs from Holmes and Featherstone (2002), who use the letter u to shorten the sine of ϑ, while we use $s = \sin\vartheta$. In order to evaluate Eqs. 4.1 and 4.3, two initial seed values

$$P_{0,0} = 1, \qquad P_{1,1} = s\sqrt{3}, \tag{4.4}$$

are required. Furthermore, the coefficient $b_{m-1,m}$ occurring in Eq. 4.1 must be defined to be zero.

The first derivatives of the ALFs can be obtained using the equation

$$\frac{d}{dt}P_{nm}(t) = \frac{1}{s}\left(ntP_{nm}(t) - f_{nm}P_{nm}(t)\right) \tag{4.5}$$

with the auxiliary variable

$$f_{nm} = \sqrt{\frac{(n^2 - m^2)(2n+1)}{2n-1}}. \tag{4.6}$$

Eq. 4.5 is simplified for sectoral ALFs since f_{nm} vanishes in that case.

4.2. Legendre Functions of the Second Kind

Similar recurrence relations exist, which can be used to compute ALFs of the second kind, abbreviated ALF2. We make use of those presented by Thong and Grafarend (1989), presented in Appendix A. The functions Q_{nm} in Eqs. 3.28 and 3.33 can be determined by means of these formulas, which are then be used in the spheroidal representation of the gravitational potential. This may be seen as the standard approach, because it is comprehensible and straight-forward. However, a more effective method was suggested by Fukushima (2013), who managed to derive recursion formulas to directly compute the ratio q_{nm} in the above referred equations.

The crucial element of this approach is the reformulation of q_{nm} in terms of a ratio of two hypergeometric functions. One major argument that supports this idea is the better handling of large values of the argument x (or y). That is the case if the evaluation point is far outside the reference spheroid. The standard approach becomes earlier numerically unstable compared to this new method (see Section 4.4). The functions $q_{nm}(x)$ in the oblate and $q_{nm}(y)$ in the prolate case can be handled in quite a similar way, however, the differences are sufficiently large to justify their treatment in two separate subsections.

Before diving into this part, a very brief exposition of hypergeometric functions is given. A linear ODE of the second order having singularities exclusively of regular behavior is denoted as an equation of Fuchsian type (Wang et al., 1989). In a second-order ODE in

which the dependent variable is multiplied by some other functions $f_1(x), f_2(x)$, a point x_0 is considered a regular singular point if one of the two functions f_1, f_2 begins to diverge while the other remains finite as $x \to x_0$[1]. Equations of Fuchsian type with exactly three regular singular points are of particular interest in this context, since every solution of such equations may be represented as a hypergeometetric function. As a matter of fact, the Legendre differential equation 3.18 belongs to this type of ODEs, having regular singularities at -1, 1, and ∞[2]. Hypergeometric functions are frequently written in the form $F(a, b; c; z)$ and are defined by the hypergeometric (or Gauss) series

$$F(a, b; c; z) = \sum_{s=0}^{\infty} \frac{(a)_s (b)_s}{(c)_s \, s!} z^s \tag{4.7}$$

under the condition of $|z| < 1$. The parentheses $(\bullet)_s$ is a shorthand notation for

$$(x)_s = x(x+1)(x+2)\ldots(x+s-1) \tag{4.8}$$

and denotes the so-called Pochhammer symbol. More details on hypergeometric functions can be found in Wang et al. (1989) or Olver et al. (2010).

4.2.1. Ratio q_{nm} in the Oblate Case

We are now focusing on the expression of $q_{nm}(x)$ by means of hypergeometric functions. According to (Fukushima, 2013), we can write

$$q_{nm}(x) = \frac{F_{nm}(x)}{F_{nm}(x_0)} \left(\frac{y_0}{y}\right)^m \left(\frac{x_0}{x}\right)^{n-m+1}, \tag{4.9}$$

where

$$F_{nm}(x) = F\left(\frac{n-m+1}{2}, \frac{n-m+2}{2}; n+\frac{3}{2}; -t\right) \tag{4.10}$$

is defined as in Eq. 4.7. The remaining variables in Eq. 4.10 are given by

$$t = \frac{1}{x^2}, \qquad y = \frac{\sqrt{u^2+E^2}}{E}, \qquad y_0 = \frac{a_1}{E}. \tag{4.11}$$

At this point, determination of $q_{nm}(x)$ is already possible. Using the definitions above, the Gauss series may be expanded up to a reasonable degree where truncation causes no decisive errors. It is, however, advisable to make use of recurrence relations to reduce

[1] Weisstein, Eric W. "Hypergeometric Function." From MathWorld–A Wolfram Web Resource. http://mathworld.wolfram.com/HypergeometricFunction.html

[2] Weisstein, Eric W. "Legendre Differential Equation." From MathWorld–A Wolfram Web Resource. http://mathworld.wolfram.com/LegendreDifferentialEquation.html

computation time. The hypergeometric function F_{nm} in Eq. 4.10 can be expressed by means of the following recurrence formula

$$F_{nm} = F_{n+1,m} + a_{nm} t F_{n+2,m}. \tag{4.12}$$

Please note that actually $F_{nm} = F_{nm}(x)$. The auxiliary variable a_{nm} is a function of n and m only and reads

$$a_{nm} = \frac{(n-m+2)(n+m+2)}{(2n+5)(2n+3)}. \tag{4.13}$$

The evaluation of Eq. 4.12 is established in quite a similar way as before, however, seed value computation is more complex. Eq. 4.12 is easily seen to rely on the functions of highest and second highest degree. These initial values are obtained by yet two other recursive equations,

$$F_{nm} = F_{n,m-1} + b_{nm} t F_{n+1,m-1}, \tag{4.14}$$

$$F_{nm} = d_{nm} F_{n,m-1} + e_{nm}(1+t) F_{n,m-2}. \tag{4.15}$$

with

$$\begin{aligned} b_{nm} &= \frac{n-m+2}{2n+3}, \\ d_{nm} &= \frac{2(m-1)}{n+m}, \\ e_{nm} &= \frac{n-m+2}{n+m}. \end{aligned} \tag{4.16}$$

Three seed values are required within Eqs. 4.14 and 4.15. These are the functions of maximum degree and order $m \leq 1$ and the zonal function of the second highest degree. They can be computed using the relation

$$F_{nm}(x) = 2x\sqrt{w}\left(\frac{y}{x}\right)^m \left(\frac{2x}{x+y}\right)^n J_{nm}, \tag{4.17}$$

which again involves a hypergeometric function J_{nm}, given by

$$J_{nm}(x) = F\left(\frac{1}{2} - m, m + \frac{1}{2}; n + \frac{3}{2}; j\right) \tag{4.18}$$

with $j = (2y(x+y))^{-1}$. What seems to require a lot of effort is actually simplified by the fact that practically only the first three terms of Eq. 4.18 are needed to provide the accuracy satisfying most applications (Fukushima, 2013).

The first-order derivative of the ratio $q_{nm}(x)$ is simply expressed by another recurrence formula,

$$\frac{d}{dx} q_{nm}(x) = -\frac{1}{y^2}\left(B_{nm} q_{n+1,m}(x) + (n+1) x q_{nm}(x)\right), \tag{4.19}$$

with

$$B_{nm} = \left(\frac{(n-m+1)(n+m+1)}{2n+3} \right) \frac{F_{n+1,m}(x_0)}{x_0 F_{nm}(x_0)}. \tag{4.20}$$

Similar formulas for the second and third-order derivatives can be derived. In this text, however, only the first derivatives are considered.

4.2.2. Ratio q_{nm} in the Prolate Case

To compute this radial attenuation factor in the prolate case, we can proceed analogously to the previous subsection. In this parametrization, Eq. 4.9 becomes

$$q_{nm}(y) = \frac{F_{nm}(y)}{F_{nm}(y_0)} \left(\frac{x_0}{x} \right)^m \left(\frac{y_0}{y} \right)^{n-m+1}, \tag{4.21}$$

where

$$F_{nm}(y) = F\left(\frac{n-m+1}{2}, \frac{n-m+2}{2}; n+\frac{3}{2}; \tau \right) \tag{4.22}$$

and

$$\tau = \frac{1}{y^2}, \qquad x = \frac{\sqrt{v^2 - E^2}}{E}, \qquad x_0 = \frac{a_3}{E}. \tag{4.23}$$

The main recurrence formula, as a consequence of the argument τ, can be written as

$$F_{nm} = F_{n+1,m} - a_{nm}\tau F_{n+2,m}. \tag{4.24}$$

The term a_{nm} is equal to Eq. 4.13. The formula to compute the functions of maximum degree is given by Eq. 4.26, which is a slightly modified version of Eq. 4.15. To determine those of the second highest degree, Fukushima (2014) suggested a decreasing-order recurrence formula (Eq. 4.25) due to better stability performance. Again, the auxiliary terms b_{nm}, c_{nm}, d_{nm} and e_{nm} remain unchanged.

$$F_{n,m-1} = F_{nm} + b_{nm}\tau F_{n+1,m-1}, \tag{4.25}$$

$$F_{nm} = d_{nm}F_{n,m-1} + e_{nm}(1-\tau)F_{n,m-2}. \tag{4.26}$$

In complete analogy to the oblate case, the seed values are computed using the equations

$$F_{nm}(y) = 2y\sqrt{w} \left(\frac{x}{y} \right)^m \left(\frac{2y}{x+y} \right)^n W_{nm}, \tag{4.27}$$

$$W_{nm}(x) = F\left(\frac{1}{2} - m, m + \frac{1}{2}; n + \frac{3}{2}; -w \right), \tag{4.28}$$

$$w = (2x(x+y))^{-1}. \tag{4.29}$$

Note that in order to evaluate Eq. 4.25, it is necessary to treat the special case $F_{m-1,m}$. By inserting these values into Eq. 4.22 it is evident that the first argument becomes zero. Consequently, only the first term in Eq. 4.7 is different from zero. That is, because according to the definition of the Pochhammer symbol in (Olver et al., 2010, p. 5.2iii), the value of order zero equals unity, i.e., $(x)_0 = 1$. Thus, $F_{m-1,m} = 1$. In some cases the hypergeometric function in 4.28 might not converge, so that different expressions are required to deal with these exceptions (see Fukushima (2014)).

The first-order derivative of the ratio $q_{nm}(y)$ is given by

$$\frac{d}{dx} q_{nm}(y) = \frac{1}{x^2} \left(B_{nm} q_{n+1,m}(y) + (n+1)\, y q_{nm}(y) \right), \tag{4.30}$$

with

$$B_{nm} = \left(\frac{(n-m+1)(n+m+1)}{2n+3} \right) \frac{F_{n+1,m}(y_0)}{y_0 F_{nm}(x_0)}. \tag{4.31}$$

This is basically the same formula as in the oblate case with only slight modifications concerning the arguments x and y as well as the sign of the Eq. 4.30.

4.3. Lamé Functions of the First and Second Kind

In the previous chapter it was shown that Lamé functions are solutions of Laplace's equation in ellipsoidal parametrization. In their influential publication "Ellipsoidal Harmonic expansions of the gravitational potential: Theory and application," Garmier and Barriot managed to present the theory of the ellipsoidal harmonics, which was slumbering for many decades, in a contemporary manner. A very brief summary of their results is given below. For a thorough treatment, the reader is of course advised to refer to the original publication.

Determining the Classes of Lamé Functions

From the theory given in 3.4.4 we know that there exist $p = 2n+1$ Lamé functions for a given degree n. This is, of course, in complete accordance with the Legendre functions. We introduce the index r

$$r = \begin{cases} n/2 & \text{if } n \text{ is even} \\ (n-1)/2 & \text{if } n \text{ is odd} \end{cases} \tag{4.32}$$

to facilitate the classification of the functions. The number of functions associated with each class depends on the degree n and, as a consequence, on the size of the coefficient

matrix of the polynomial involved in the computation of the Lamé function. We denote the number of functions by the symbol N_f, where f represents one of the four classes. The following applies:

$$N_{\mathcal{K}} = r + 1, \quad N_{\mathcal{L}} = n - r, \quad N_{\mathcal{M}} = n - r, \quad N_{\mathcal{K}} = r. \tag{4.33}$$

From a practical point of view, we found it useful to generate a "class vector" $\mathbf{c}$ holding all classes corresponding to the order p for a given degree n. It is trivially generated by matrix-vector-multiplication,

$$\mathbf{c} = \mathbf{T}\mathcal{E} \tag{4.34}$$

where the vector $\mathcal{E}$ is symbolically written as

$$\mathcal{E} = \begin{bmatrix} \mathcal{K} & \mathcal{L} & \mathcal{M} & \mathcal{N} \end{bmatrix}^{\mathsf{T}}. \tag{4.35}$$

In practice, the components may take the form of integers to indicate the respective class (e.g., $1, 2, 3, 4$). The matrix $\mathbf{T}$ is a block diagonal matrix where each block is an all-ones column vector consisting of N_f elements, denoted as $\mathbf{I}_{N_f}$.

$$\mathbf{T} = \begin{bmatrix} \mathbf{I}_{N_{\mathcal{K}}} & & & \\ & \mathbf{I}_{N_{\mathcal{L}}} & & \\ & & \mathbf{I}_{N_{\mathcal{M}}} & \\ & & & \mathbf{I}_{N_{\mathcal{N}}} \end{bmatrix}. \tag{4.36}$$

To give an example, the class vector of degree $n = 3$ is shown:

$$\mathbf{c}_3 = \begin{bmatrix} 1 & 1 & 2 & 2 & 3 & 3 & 4 \end{bmatrix}^{\mathsf{T}} \tag{4.37}$$

In order to keep performance high, the use of sparse matrices is recommended.

Computation of the Lamé Polynomials

The method of computing Lamé functions was derived by Dobner and Ritter (1998). It involves polynomials of the type

$$P_n^p(w_i) = \sum_j^{N_f - 1} b_j \left(1 - \frac{w_i^2}{k_3^2}\right)^j, \tag{4.38}$$

where w_i is one of the three coordinates, ρ, μ, ν, presented in Chapter 2. The polynomial coefficients b_j are obtained by eigenvalue-eigenvector-decomposition. For details and formulas, the reader is referred to Appendix B.

Computation of the Lamé Functions

Based on the polynomials $P_n^p(w_i)$, the Lamé function is computed by

$$E_n^p(w_i) = \psi_n^p(w_i)\, P_n^p(w_i)\,, \tag{4.39}$$

where $\psi_n^p(w_i)$ is a multiplier that is, somehow, a stumbling block in the otherwise tractable problem of computing Lamé functions. The reason therefore lies in the sign ambiguities of the ellipsoidal coordinates (cf., Section 2.5). This and only this equation requires the coordinates in their actual (non-squared) form:

$$\psi_n^p(w_i) = \begin{cases} w_i^{n-2r} & \text{for } \mathcal{K} \\ w_i^{1-n+2r}\sqrt{\left|w_i^2 - k_3^2\right|} & \text{for } \mathcal{L} \\ w_i^{1-n+2r}\sqrt{\left|w_i^2 - k_2^2\right|} & \text{for } \mathcal{M} \\ w_i^{n-2r}\sqrt{\left|\left(w_i^2 - k_2^2\right)\left(w_i^2 - k_3^2\right)\right|} & \text{for } \mathcal{N} \end{cases} \tag{4.40}$$

Thus, determination of the Lamé function is always ambiguous. This fact alone complicates the usage of ellipsoidal harmonics. However, when it comes to gravitational field modeling we are never confronted with single Lamé functions, but always with the triple product $E_n^p(\rho)\, E_n^p(\mu)\, E_n^p(\nu)$. We can make use of this fact by expressing the product of the underlying multipliers in terms of Cartesian coordinates as

$$\Psi_n^p(x_1, x_2, x_3) = \psi_n^p(\rho)\, \psi_n^p(\mu)\, \psi_n^p(\nu)\,, \tag{4.41}$$

which was shown to be

$$\Psi_n^p(x_1, x_2, x_3) = \begin{cases} (k_2 k_3 x_1)^{\delta} & \text{for } \mathcal{K} \\ k_2 x_2 \sqrt{k_2^2 - k_3^2}\,(k_2 k_3 x_1)^{\delta'} & \text{for } \mathcal{L} \\ k_3 x_3 \sqrt{k_2^2 - k_3^2}\,(k_2 k_3 x_1)^{\delta'} & \text{for } \mathcal{M} \\ k_2 k_3 x_2 x_3 \left(k_2^2 - k_3^2\right)(k_2 k_3 x_1)^{\delta} & \text{for } \mathcal{N} \end{cases} \tag{4.42}$$

where δ and δ' are auxiliary variables indicating the evenness or oddness of the degree n:

$$\delta = \begin{cases} 0 & \text{if } n \text{ is even} \\ 1 & \text{if } n \text{ is odd} \end{cases}, \qquad \delta' = \begin{cases} 1 & \text{if } n \text{ is even} \\ 0 & \text{if } n \text{ is odd} \end{cases} \tag{4.43}$$

The triple product of Lamé functions (cf. Eq. 2.14) is therefore given by

$$Y_n^p(x_1, x_2, x_3, \rho, \mu, \nu) = \Psi_n^p(x_1, x_2, x_3)\, P_n^p(\rho)\, P_n^p(\mu)\, P_n^p(\nu)\,. \tag{4.44}$$

Note that in Eq. 3.44 we actually need the second kind of Lamé function. From Eq. 3.43 we know, however, that functions of the first kind can easily be converted to those of the second kind by multiplication with a certain integral I_n^p (see below).

Normalization

The surface ellipsoidal harmonics, i.e., $E_n^p(\mu)\,E_n^p(\nu)$ can be normalized by the normalization factor γ_n^p,

$$\gamma_n^p(\mu,\nu) = 4\pi\,(\alpha B - \beta A)\,. \tag{4.45}$$

This is the formula derived by Garmier and Barriot (2001) multiplied by the constant value 8, which was suggested by Dassios (2012) in order to regard every octant. As simple as this equation seems at first sight, it actually poses quite a lot of effort to solve. Four elliptic integrals are involved within the determination of the constants α, β, A, B (see Appendix B). Sophisticated numerical methods are required in order to get reliable results. The normalized surface harmonics are then

$$\overline{E}_n^p(\mu)\,\overline{E}_n^p(\nu) = \frac{E_n^p(\mu)\,E_n^p(\nu)}{\sqrt{\gamma}}. \tag{4.46}$$

Whenever we speak of these Lamé functions we refer to the normalized kind. For simplicity of notation, however, we will continue to write E instead of $\overline{E}$.

First Order Derivative

In the actual implementation a different representation of the derivative of the Lamé functions will be used. Nevertheless, this part includes the formulas of the first-order derivative of $E(w_i)$ for the sake of completeness:

$$\frac{\partial}{\partial w_i}E_n^p(w_i) = \frac{\partial\psi(w_i)}{\partial w_i}\frac{\partial P_n^p(w_i)}{\partial w_i}. \tag{4.47}$$

The respective derivatives of Eqs. 4.39 and 4.40 are trivial and not indicated here.

Lamé Functions of the Second Kind

In the previous section we stated that we never have to deal with single Lamé functions, but always with the triple product. This is, strictly speaking, not correct, because in order to compute the radial attenuation, the Lamé functions of the second kind $F_n^p(a_1)$ (see Eq. 3.44) are required. But, since the semi-major axis a_1 can only have positive values we will not have to face ambiguity issues here and can therefore apply Eq. 4.40 without any troubles.

We recall the definition of the Lamé function of the second kind (Eq. 3.43) and rewrite it by replacing the infinite integral limits with finite values, as

$$F_n^p(\rho) = (2n+1)\, E_n^p(\rho) \int_0^{\rho^{-1}} \frac{t^{2n} dt}{[E(t)]^2 \sqrt{1-k_2^2 t^2}\sqrt{1-k_3^2 t^2}}, \tag{4.48}$$

and abbreviate it using the notation

$$F_n^p(\rho) = E_n^p(\rho)\, I_n^p(\rho). \tag{4.49}$$

It is obvious that the term $(2n+1)$ cancels when computing the ratio $F(\rho)/F(a_1)$. Evaluation of $I_n^p(\rho)$ must be carried out by means of numerical integration methods.

The derivative of the Lamé function of the second kind is

$$\frac{\partial}{\partial\rho} F_n^p(\rho) = \frac{\partial}{\partial\rho} E_n^p(\rho)\, \frac{\partial}{\partial\rho} I_n^p(\rho) \tag{4.50}$$

with

$$\frac{\partial}{\partial\rho} I_n^p(\rho) = \frac{-1}{\left(E_n^p(\rho)\right)^2 \sqrt{\rho^2-k_2^2}\sqrt{\rho^2-k_3^2}}. \tag{4.51}$$

We will encounter the derivative of the integral I_n^p when we set up the relations between the gravitational acceleration and the parameters α_n^p (from Eq. 3.44).

A Different Expression of the Gravitational Potential

Considering the above relations, we may rewrite the ellipsoidally parametrized gravitational potential as

$$V(x_1, x_2, x_3, \rho, \mu, \nu) = GM \sum_{n=0}^{\infty} \sum_{p=1}^{2n+1} \alpha_n^p \frac{I_n^p(\rho)}{I_n^p(a_1)} \frac{Y_n^p(x_1, x_2, x_3, \rho, \mu, \nu)}{E_n^p(a_1)\sqrt{\gamma_n^p}}. \tag{4.52}$$

We introduce another symbol to abbreviate the fraction in the sum above and to simplify notation, so that

$$V = GM \sum_{n=0}^{\infty} \sum_{p=1}^{2n+1} \alpha_n^p V_n^p, \tag{4.53}$$

where the dependencies have been omitted for convenience reasons.

4.4. Investigating the Applicability of the Basis Functions

We introduced formulas to compute the basis functions of spherical, spheroidal and ellipsoidal harmonics. We are now interested in finding out how these functions behave and to what peculiarities we must pay attention to when applying them. We will see that one crucial point is the choice of the reference figure's semi-axes, which has a major impact on the numerical stability of the functions. This, of course, exerts no influence whatsoever on the ALF of the first kind, which makes them incredibly reliable in practical usage. The limiting factor in evaluating them really comes down to the computer capacity when trying to calculate functions of high degrees [3].

ALF of the Second Kind

In the definition of the ALF2 in Section 4.2 it was stated that the recurrence formulas elaborated in the respective subsections should be preferred over traditional formulas found in the literature. We will now try to find arguments to corroborate this recommendation.

In contrast to spherical harmonics, spheroidal harmonics need to make use of Legendre functions to account for the exterior solutions of the Laplace equation. This complicates their usage, since the "radial coordinate" can take very large values which may cause numerical problems in the computation of the basis functions. In addition to that, the semi-focal distance of the reference spheroid appears in the denominator of some terms involved within the computation (cf. Eqs. 3.11 and 3.23) and poses therefore another crucial aspect, especially for sphere-like spheroids.

With this in mind, two tests were carried out. The first test should shed light on the influence of the semi-focal distance. The second test was designed to analyze the effect of increasing distance between field point and reference spheroid. In this part we only deal with oblate spheroidal harmonics, since their prolate counterpart behaves accordingly.

To control both these quantities, the flattening f of the reference spheroid and the second numerical eccentricity e' of the spheroid related to the coordinate u were used. They are defined as

$$f = \frac{a_1 - a_3}{a_1}, \qquad e' = \frac{\sqrt{a_1^2 - a_3^2}}{u}. \tag{4.54}$$

The algorithm described in Section 4.2 is denoted as *Method 1*, while the "classical" method is referred to as *Method 2*. The latter is based on Thong and Grafarend (1989), cf. Appendix A. We supposed a small body, which is fully contained by a reference

[3] Numerical issue of computing ALFs of extremely high degrees (say a few thousands) is not of interest here since they will not be encountered with *small* body gravitational field modeling.

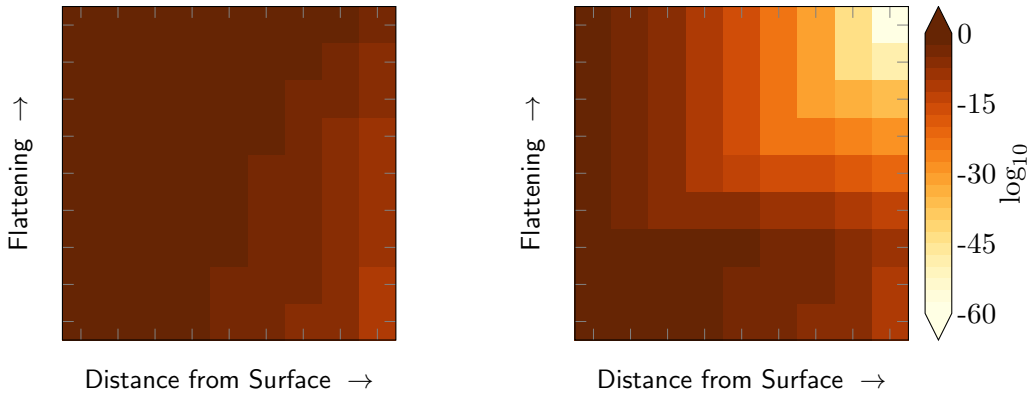

(a) Method 1 **(b)** Method 2

Figure 4.1.: Comparison of the magnitudes of the ratios $q_{10,0}$ computed via Method 1 (4.1a) and Method 2 (4.1b). Flattening increases from bottom upwards. The evaluation point's altitude increases from left to right.

sphere of radius $R = 10\,\text{km}$. According to Davis et al. (2002), there are more than one thousand asteroids in our solar system exceeding that size and millions inferior to it. The maximum degree of expansion was chosen to be $N = 10$. With these parameters, the ratio of the ALF2s, q_{nm}, was computed for reference spheroids of constant semi-major axis ($a_1 = R$) and decreasing semi-minor axis a_3. The field point, controled by the coordinate u, was chosen in such way that e' took values in the inverval $[e'_0, 0]$, with

$$e'_0 = \frac{\sqrt{a_1^2 - a_3^2}}{a_3}. \tag{4.55}$$

In other words, the radial distance from the surface increased from zero to infinity. A two-dimensional matrix plot was created to visualize the respective effects (Figure 4.1). Both panels show the ratio of the zonal ALF2s of degree 10. The values of the factor q_{nm} cover a large range of magnitudes, therefore, a logarithmic scale was chosen to enhance comparability. It is interesting to see that the values of q_{nm} are for both methods of similar magnitude when referred to slightly flattened spheroids, no matter the distance. Moving on the upper parts of the figure, the magnitudes of the values obtained via Method 2 rapidly decrease with increasing flattening as well as growing distance from the surface. The situation exacerbates even further when the maximum degree of the expansion is increased. For $N = 60$, for instance, the minimum can be found to be -120. Continuing in this manner may lead to arithmetic underflow.

In Figure 4.2, the influence of flattening is visualized again. This time, the distance from the surface was set to be constant, so that the coordinate u satisfies

$$u = \frac{\sqrt{a_1^2 - a_2^2}}{e_0' - \varepsilon}, \qquad \varepsilon = \frac{e_0'}{4}. \tag{4.56}$$

Note that ε controls the distance from the surface. This specific value was chosen arbitrarily. It simply represents a point not too far from nor too close to the spheroid. To get a clearer picture: if the reference spheroid was referred to the Earth, the evaluation point would be about 2000 km above the North Pole. Besides the zonal part of the functions, also the sectoral and one tesseral function is shown. The values of Method 1 are drawn in terms of solid lines while those of the second method are dashed. Moreover, the corresponding parameters of the reference spheroids of four small bodies are indicated as gray lines. More information about these bodies will be given in Chapter 7. Again, for reasons of comparability, the respective flattening parameter of the Earth is stated, which is about 0.003 and would not even be visible on this scale. Figure 4.2 confirms what was indicated before. The dashed lines drop very soon which allows for the conclusion that this method is only reliable for spheroids with small semi-focal distances. The curves associated with Method 1 rise slowly and do not show erratic reactions to increasingly flattened spheroids. Also, no particular effect of differently sized semi-major axes could be detected. Very similar results were obtained for, e.g., $a = 10\,\mathrm{m}$. This is in contrast to the ellipsoidal harmonics, as we will see later. Thus, Method 1 can be seen as an adequate means for small-body gravity modeling.

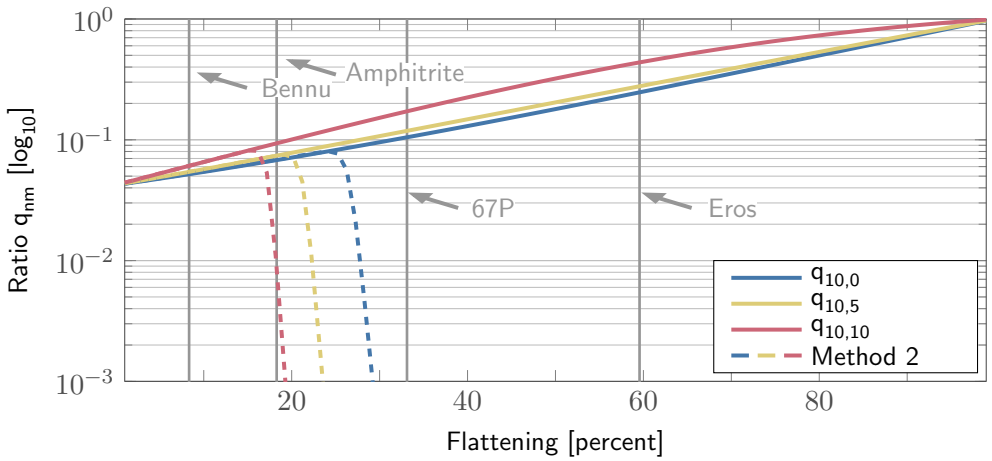

Figure 4.2.: Comparison of the magnitudes of the ratios $q_{10,0}$, $q_{10,5}$ and $q_{10,10}$ computed via both Method 1 and Method 2. The evaluation point's altitude is constant. The reference spheroids of four small bodies are indicated by gray lines.

When it comes to prolate spheroids, very similar behavior of the functions can be observed when the above described tests are applied. For reasons of brevity we skip the respective figures.

Lamé Functions

We will now turn to the Lamé functions and discuss some aspects of their practical usage. Gravitational field modeling by means of ellipsoidal harmonics involves double products of Lamé functions of the first kind, ratios of those of the second kind and a complicated normalization factor to balance the magnitudes. A lot of computational work is coupled with its determination. By looking at the system of formulas, three crucial parameters stick out:

- the semi-focal distances k_2 and k_3,
- the magnitude of the semi-major axis a_1,
- the degree n of the expansion.

In a similar way as before, we analyzed the effects of the shape of the ellipsoid. Again a small body with mean radius of 10 km was supposed. The field point P was defined on the circumscribed reference sphere with coordinates

$$r = 10000, \qquad \vartheta = 45^\circ \qquad \lambda = 45^\circ. \tag{4.57}$$

In contrast to ALF2, the distance of the field point from the surface of the reference ellipsoid did not turn out to have great impact on the results. Moreover, the octant in which the field point lies was inessential. To control the reference figure, the semi-major axis a_1 was set constant to 10 km and the semi-minor axes were defined by means of the flattening parameters $f_{(2,3)}$

$$f_2 = \frac{a_1 - a_2}{a_1}, \qquad f_3 = \frac{a_1 - a_3}{a_1}, \tag{4.58}$$

with the inequality

$$0 < f_2 < f_3 < 1. \tag{4.59}$$

Again the maximum degree of expansion was set to 10. The main issue one has to face with the Lamé functions becomes obvious by looking at Figure 4.4a. This matrix plot is a visualization of the Lamé function $E_{10}(\mu)$. Every gray square is subdivided into four squares, each of which represents the first solution of all classes of the Lamé function of degree 10. Their arrangement is shown in Figure 4.3.

We used logarithmic scaling to emphasize the large orders of magnitude, what these function values take. The geometric meaning of the variation of the semi-focal distances

$\mathcal{L}$	$\mathcal{N}$
$\mathcal{K}$	$\mathcal{M}$

Figure 4.3.: Detail of Figure 4.4

can easily be interpreted. The lower left corner represents oblate-like ellipsoids, because k_3 and k_2 are small, hence, the semi-minor axes are large. Increasing k_3 shapes the ellipsoid more prolate, so that the upper left corner stands for almost prolate ellipsoids. The factor k_2 obviously controls the "tri-axiality" of the ellipsoid. The extreme cases (not plotted) would be a sphere in the lower-left corner, a circle in the lower right corner and a straight line for both upper corners (assuming both semi-minor axes to be zero).

The values of this Lamé function[4] ranges only within a few orders of magnitude. This is somewhat surprising because the sheer shape (regardless of the size) of the reference ellipsoid does not seem to have as much influence on the magnitude as in the spheroidal case (cf. Figure 4.1b). Since the evaluation of a triple product of Lamé functions is necessary in order to compute the gravity potential, the order of magnitude of the same already sums up to about 120. Programming environments which operate in accordance with the IEEE Standard 754 (Kahan, 1996) are able to represent numbers of double-precision floating-point formats up to a maximum of almost 1.8×10^{308}. MATLAB ©, which was used to implement this work, belongs to those programs.

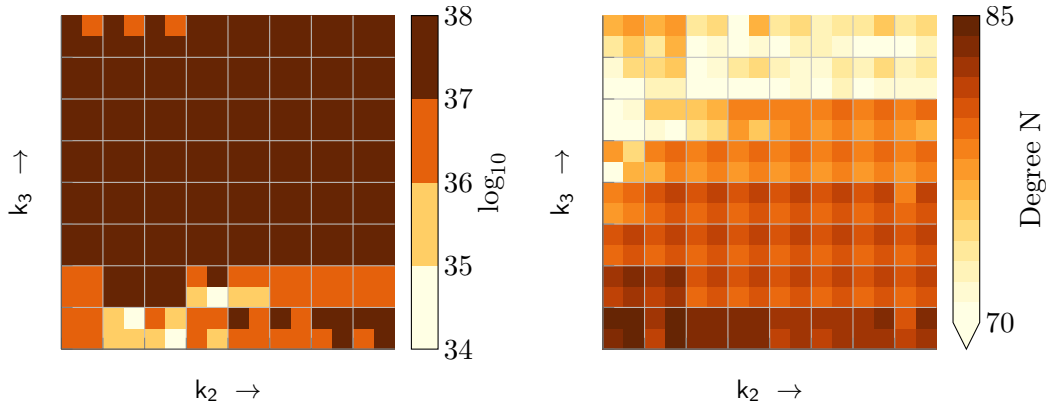

(a) Magnitudes of $E_{10}(\mu)$ **(b)** Maximum computable degree

Figure 4.4.: The left image visualizes the magnitudes of the Lamé function $E_{10}(\mu)$ for differently shaped reference ellipsoids. On the right, the maximum computable degrees for the corresponding ellipsoids are visualized. Computable in this context means no over- or underflow occurs.

[4] Very similar results may be obtained for $E_{10}(\rho)$ and $E_{10}(\nu)$.

The issue of overflow was the motivation for Figure 4.4b. By increasing the degree n of the Lamé function, the exponent grows as well. The matrix in this figure is configured in the same manner as the one on the left. But, the colorized values now represent the maximum degree that is obtainable for $E_n(\mu)$ before overflow errors occur. In contrast to what was seen from Figure 4.4a, the geometrical configuration plays an influential role in this case. Especially the increase of the factor k_3, controling the "spheroidity" of the ellipsoid, worsens the achievable resolution. This, however, is somewhat vaguely put, since the discernible pattern in the matrix is quite coarse. Be that as it may, a difference of more than 15 degrees between extremely flat and almost spherical ellipsoids is commanding.

So far, the reference ellipsoid's semi-major axis was kept constant. Attentive readers know, though, that asteroids and comets in our solar system vary heavily in size (cf., Chapter 1). Figure 4.4 may therefore only be seen as one exemplary case. We are now interested in finding out what influence the body's size exerts on the numerical stability of the Lamé functions. The field point P is again defined to lie on the circumscribed reference sphere, however the radial component is now a variable, so that

$$r = a_1, \qquad \vartheta = 45^\circ, \qquad \lambda = 45^\circ. \tag{4.60}$$

The length of the semi-major axis was limited to the interval $\left[0, 10^7\right]$ to cover small rocks or even planets[5]. For every value of a_1, three corresponding matrices as shown in Figure 4.4a were generated. To get a feeling of what orders of magnitude the other elements of the ellipsoidal harmonics take, the triple product Y_n was chosen instead of $E_n(\mu)$ and the integral I_n involved in the computation of the second kind functions as well as the normalization constant γ_n were computed too. The maxima of these matrices are visualized in terms of line plots in Figures 4.5a and 4.5b for degrees 10 and 20, respectively. The dashed lines indicate negative exponents. From 4.5 we can deduce a strong dependence on the size of the reference ellipsoid. All curves rise with increasing length of a_1. For higher degrees, the rise takes place even faster. Especially the normalization factor γ seems to cause difficulties and, for degree 20, can only be computed for ellipsoids smaller than 10^4.

We proceed analogously to the previous case and are eager to find the maximum obtainable degree for differently sized ellipsoids. To achieve this, a matrix corresponding to the one in Figure 4.4b was computed for every instance of a_1. This time, we directly evaluated V_n as known from Eq. 4.53. Figure 4.6 contains the results of this investigation. The mean computable (maximum) degree N for differently sized and shaped ellipsoids is plotted in terms of a dark-blue solid line. The lighter area surrounding it indicates the minimum (maximum) degree N and the maximum (maximum) degree N. This graphic also features the reference parameters of the four bodies known from the oblate case.

[5]Note that the Earth's semi-major axis is about 6.4×10^6 m

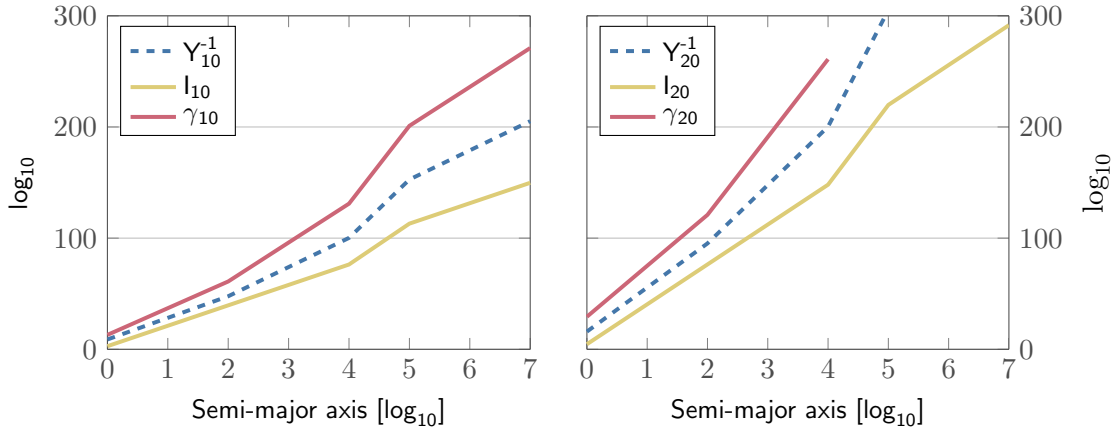

(a) Degree $N = 10$ **(b)** Degree $N = 20$

Figure 4.5.: Comparison of the magnitudes of three components of the ellipsoidal harmonic series expansion, namely Y_n, I_n and γ_n. The left image visualizes these quantities for degree $N = 10$, the right for $N = 20$.

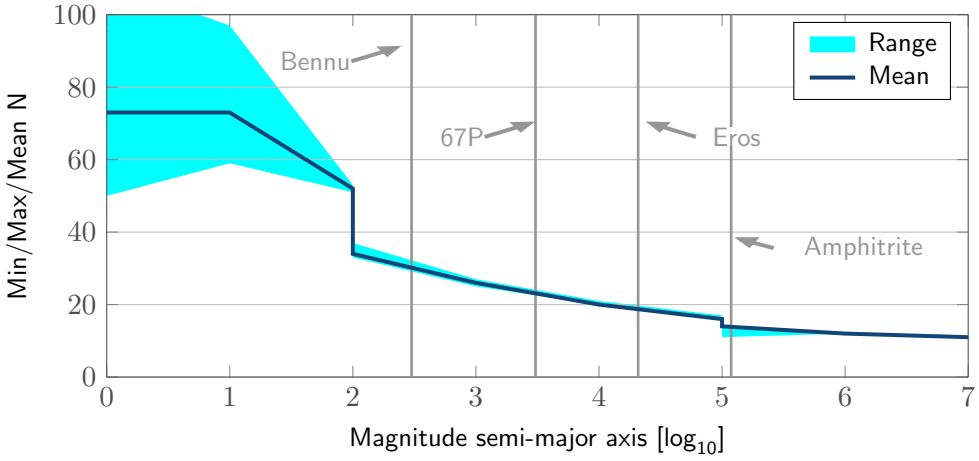

Figure 4.6.: Visualization of the maximum computable degree in dependence of the magnitude of the reference ellipsoid's semi-major axis.

The figure is self-explanatory. Still, it is worth pointing out that the shape of the reference ellipsoid seems to influence the results for bodies smaller than 10^2 strongly. Nevertheless, the attainable resolution is still better than for larger objects. According to Hu (2012), who investigated the applicability of the ellipsoidal harmonics on the small bodies Phobos and 433 Eros, computation of the normalization factor γ_n for degrees higher than ten tends to become unreliable. The author claims, however, that no serious errors occur when modeling the respective gravitational fields with series expansions up to degree 20. This corresponds to our findings in Figure 4.6.

Two thoughts shall be mentioned as a proposal to increase the resolution. Firstly, an obvious shift down three orders of magnitudes is possible when the units of lengths are chosen to be kilometres. This, however, is only advisable for the computation of the individual elements itself. Before using them in combination with gravity quantities, back-conversion should be performed. The corresponding relation, for instance for the normalization factor γ, reads

$$\gamma_n\,[\mathrm{m}] = \gamma_n\,[\mathrm{km}] \cdot 10^{12n}. \tag{4.61}$$

Let us return one more time to Figure 4.6. An extensive treatment of the ellipsoidal harmonic gravitational field representation of asteroid 4 Vesta has been carried out by Park et al. (2014). Vesta, one of the largest asteroids in our solar system, is approximated by an ellipsoid with semi-major axis length of about 300 km. In their results they state that the stable computation of the Lamé functions is possible up to degree 24. This is again in the range of our results when computing the ellipsoidal harmonics on the km-scale.

The second idea (not considered in Fig. 4.6) is based on the logarithmic representation of the functions. We may rewrite the ellipsoidal harmonics V_n^p as

$$\bar{V_n^p} = \bar{I_n^p}\,(\rho) - \bar{I_n^p}\,(a_1) + \bar{Y_n^p}\,(x_1, x_2, x_3, \rho, \mu\nu) - \bar{E_n^p}\,(a_1) - \frac{\bar{\gamma_n^p}}{2}. \tag{4.62}$$

The symbol $\bar{\bullet}$ denotes the logarithm of base 10. The term Y, containing the triple product of Lamé functions, can be decomposed this way itself. We must take care of a few things, though. The base-10 logarithm of a negative number is undefined in the real number system, the result is complex. We can either accept the non-real nature of the result or separate the signs before performing the logarithmic transformation. The appropriate sign can then easily be recovered. Besides that, at some point we have to re-convert the result to the linear scale. This means, that although we might be able to compute $\bar{V_n^p}$ for significantly higher degrees, the use of V_n^p is only guaranteed as long the logarithmic result does not exceed the value of 308.

Chapter 5.

Forward modeling

The process of using a known physical property model to analyze its effects on a related quantity is called forward modeling. In case of gravitation, the underlying physical property would be the density distribution inside a body with known shape. This chapter is dedicated to the method of determining the gravitational field of a small body based on a three-dimensional shape model.

5.1. The Shape of Small Bodies

As explained in the introducing section, small solar system bodies' gravitational attraction is insufficient to naturally shape them into a spherical form. The natural shape of the body is usually irregular and often elongated. Various asteroids and few comets have been visited by spacecraft over the last decades. Most of them were targets of flybys, i.e., the spacecraft was steered to closely pass the body. During these flybys data is collected which is then used to derive a three-dimensional shape model of the body. The resolution of these 3D models strongly depends on the quality and type of data and the duration of the visit. NASA's space mission NEAR Shoemaker, for instance, did not only flyby the asteroid 433 Eros, but managed to orbit it and even land on its surface. This allowed for a detailed investigation of the asteroid. ESA's Rosetta went one step further and performed a smooth landing on Comet 67P/Churyumov–Gerasimenko. Its lander module Philae carries a miniature laboratory and scientific instruments to thoroughly study the comet. Spectacular pictures have been posted via the Internet and a preliminary shape model was released in October 2014[1]. A full collection of shape models of small bodies which were visited by spacecraft is provided by NASA and can be obtained from its Planetary Data System (PDS) website[2]. In addition to the PDS

[1] http://sci.esa.int/rosetta/54728-shape-model-of-comet-67p/
[2] http://pds.jpl.nasa.gov/

shape models, the Database of Asteroid Models from Inversion Techniques (DAMIT)[3] provides coarse models of many other small objects.

PDS Shape Models

The PDS website provides shape models in different formats, depending on mission and target.

- Table of coordinates: This is the most simple format. The topography of the body is listed in terms of longitude, latitude and radius coordinates. This yields a three-dimensional point cloud. The disadvantage of this format lies in the lack of any topological information, which makes it difficult to reconstruct the real shape of the body, especially if it has concave features like craters or holes.
- Spherical harmonics: Sometimes, a table with spherical harmonics coefficients describing the topography is available. The spatial resolution obtainable via this method is limited to the degree of the expansion. To give some numbers: A spherical harmonics expansion to degree 60 leads to a spatial resolution of 3°. On Earth, this corresponds to about 330 km at the equator, for small bodies this values is much smaller (a few hundred metres for 433 Eros, for instance). The usefulness of this method is the possibility to generate coordinate grids with arbitrary longitude and latitude values. On the downside, the lack of topological clarity remains. The formula to evaluate the radial components is

$$r(\vartheta, \lambda) = \sum_{n=0}^{\infty} \sum_{m=0}^{n} \left[P_{nm} \left(c_{nm} \cos m\lambda + s_{nm} \sin m\lambda \right) \right], \tag{5.1}$$

  where P_{nm} of course indicates the ALF of the first kind.
- Triangular plate form: This is the format most shape models are avialable in. The idea is to represent the shape of a body in terms of a polyhedron consisting of triangular faces. Two tables are involved. The vertices table is a list of enumerated points with three columns corresponding to the respective Cartesian coordinates. The second table describes the topology in terms of enumerated faces with identification number of the three corners in counter-clock wise order. The coordinates are obtained by looking for the respective point ID in the vertices table. Sometimes only 3D point clouds are available, but a polyhedron shape is required for different applications, e.g., gravitational field determination. To convert the point cloud into a shape model, some sort of triangulation must be performed. Although it is not the purpose of this thesis to develop highly reliable meshing algorithms,

[3] http://astro.troja.mff.cuni.cz/projects/asteroids3D

it is nevertheless worth pointing out that we found a simple way to generate shape models with sufficient accuracy for the purpose of gravity field modeling. Since most triangulation algorithms provided by software like, e.g., Matlab, are incapable of reconstructing concave shapes, we used a simple trick to avoid this issue. In order to get the topological information, we can project all vertices radially onto a surrounding sphere and use these new coordinates to apply the triangulation algorithm. We obtain a table of faces which we can use in combination with the original coordinates of the vertices. This method allows us in quite an elegant way to create polyhedral representations of a body, whose shape is given in terms of a list of spherical harmonics coefficients. We could use this approach, for example, to generate a polyhedral model of the Earth. The respective spherical harmonics coefficients can be obtained from many online sources[4].

- Implicity Connected Quadrilateral format (ICQ): Models from recent space missions (e.g., Cassini) are usually provided in the implicity connected quadrilateral format, developed by Robert Gaskell. A detailed description of this format is given, for instance, in Gaskell (2013).

5.2. Gravitational Field Representation

The gravitational field of such bodies can be represented in various ways. Most commonly, harmonic series expansions are used to describe the exterior potential (see Chapter 6). Alternatively, the gravitational effects can be approximated by using the mass concentrations (mascon) approach. The idea behind this method is simple. The body's interior is filled with individual point masses, located on a regular grid. The total mass of the body corresponds to the sum of the individual masses (cf. Eq. 3.4). The simplicity and intuitiveness of the mascon approach is diminished by the increasingly computational complexity as well as the fact that errors in the force vector might become unacceptable large (Werner and Scheeres, 1997).

A third way of modeling gravitation is to approximate the asteroid as a constant density body. The great advantage of this approach lies in the fact that closed-form expressions can be applied and therefore no truncation errors occur. To give the most simple example, consider the exterior gravitational potential of a constant density sphere

$$V = \frac{GM}{r}, \tag{5.2}$$

where GM is the product of Newton's gravitational constant and the total mass of the sphere M. The evaluation for an arbitrary point outside the sphere solely depends on its

[4] E.g., http://geodesy.curtin.edu.au/research/models/earth2012/

radial distance r. Similar expressions exist for simple shapes like cylinders or ellipsoids. For some applications, this might already be sufficient. For higher accuracy applications like the landing of a spacecraft on a comet, the deviation to the actual gravitational field may not be neglected.

An elegant approach to generalize this idea is to use a polyhedral representation of the body and to analytically evaluate its gravitational effects. The best general reference here is Werner and Scheeres (1997). The developed method allows for the computation of the potential as well as its first and second derivatives. In the following section, we briefly summarize without proofs their results.

5.3. Gravitation of a Polyhedron

The potential V for a point outside a solid body is determined by Eq. 3.9. The basic idea of the polyhedron method is to simplify this equation by expressing the potential in terms of a vector field and subsequently applying the Gaussian divergence theorem. This theorem relates the volume integral of the divergence of some vector field $\mathbf{g}$ to the surface integral of $\mathbf{g}$ by

$$\iiint_v (\nabla \cdot \mathbf{g})\, dv = \iint_\sigma (\mathbf{n} \cdot \mathbf{g})\, d\sigma, \tag{5.3}$$

where σ refers to the closed (!) boundary of the volume v. The surface's orientation must be positive so that its normal vector $\mathbf{n}$ points outside. A further simplification of this surface integral to a one dimensional line integral is achieved by applying Green's theorem, which is basically the divergence integral in the two-dimensional case.

Based on this, Werner and Scheeres (1997) derived practical formulas for the special case of polyhedra consisting of triangular faces. Before stating their results, some terms and definitions needed within the graph theory are given below:

- Polyhedron: a solid whose faces are polygons.
- Face: a planar part of the surface of a solid.
- Edge: a line segment that is part of the boundary of a face.
- Vertex: an intersection point of two edges.

Let N_f be the set of all faces of the polyhedron and N_e the set of all edges. Given the special case of triangular faces, the number of faces n_f and the number of unique edges n_e are related by

$$n_e = n_f \frac{3}{2}. \tag{5.4}$$

From Eq. 5.4 follows that there must exist $n_v = n_e - n_f + 2$ vertices. We follow the author's notation and introduce $\mathbf{r}_i$, i.e., the three-dimensional directional vector from some evaluation point to each vertex $v_i, i = 1, 2, \ldots, n_v$. Each face comprises three vertex vectors $\mathbf{r}_j^f$ and each edge two vertex vectors $\mathbf{r}_k^e$. Moreover the outward pointing face normal $\mathbf{n}_f$ and accordingly the edge normal $\mathbf{n}_e^f$, perpendicular to $\mathbf{n}_f$ and the edge are introduced. Please note the superscript f in the above definition. It must be clarified that each edge is associated with two faces, thus, two different normal vectors, $\mathbf{n}_e^f$ and $\mathbf{n}_e^{f'}$, are involved.

The final equations for constant density polyhedral gravitation and gravitational gradient were derived to be:

$$V = \frac{1}{2} G\rho \sum_e^{N_e} \mathbf{r}_e \mathbf{E}_e \mathbf{r}_e \cdot L_e - \frac{1}{2} G\rho \sum_f^{N_f} \mathbf{r}_f \mathbf{F}_f \mathbf{r}_f \cdot \omega_f, \tag{5.5}$$

$$\mathbf{g} = -G\rho \sum_e^{N_e} \mathbf{E}_e \mathbf{r}_e \cdot L_e + G\rho \sum_f^{N_f} \mathbf{F}_f \mathbf{r}_f \cdot \omega_f. \tag{5.6}$$

Some of the terms in the above equations need further explanation. $\mathbf{E}_e$ and $\mathbf{F}_f$ are the edge dyad $\mathbf{n}_f \mathbf{n}_e^f + \mathbf{n}_{f'} \mathbf{n}_e^{f'}$ and the face dyad $\mathbf{n}_f \mathbf{n}_f$, respectively. The evaluation of the one-dimensional line integral can be conveniently established using

$$L_e = \ln \frac{r_1^e + r_2^e + e_e}{r_1^e + r_2^e - e_e}, \tag{5.7}$$

where e_e is the constant length of the edge and $r_i^e, i = 1, 2$ is the length of the vector $\mathbf{r}_i^e$ connecting the evaluation point and the vertices of the edge. Finally, the factor ω_f is given by

$$\omega_f = 2 \arctan \frac{\mathbf{r}_1^f \mathbf{r}_2^f \times \mathbf{r}_f^f}{r_1^f r_2^f r_3^f + r_1 \left(\mathbf{r}_2^f \mathbf{r}_3^f\right) + r_2 \left(\mathbf{r}_3^f \mathbf{r}_1^f\right) + r_3 \left(\mathbf{r}_1^f \mathbf{r}_2^f\right)}. \tag{5.8}$$

For a deeper discussion of this topic please refer to Werner and Scheeres (1997) and Scheeres (2012). A more general solution for polyhedra composed of polygons with arbitrary vertex count was established by D'Urso (2013).

Chapter 6.

Backward modeling

In this chapter we are concerned with setting up a relation between the observed gravity quantities and the unknown gravitational field coefficients. If the density distribution of the respective body is known, the orthogonality relations of the basis functions allow for the direct computation of the unknown parameters (Hofmann-Wellenhof and Moritz, 2006, Sections 1.9-1.10). Since no real data is involved in our investigations, the forward modeled gravitational potential and its derivative serve as "observations". We point out again that these observations were computed under the assumption of constant density. Therefore, application of the integral formulas provided in the above referenced book to determine the coefficients (for spherical harmonics, in this case) is possible. A different approach of connecting the unknowns with the observations is the use of least squares methods. A functional model relates each observation to the gravitational coefficients, which leads to a system of linear observation equations. Usually, the number of observations clearly exceeds that of parameters. The solution of such overdetermined systems will very shortly be outlined in the first section of this chapter. The second section illustrates exemplarily how to set up the system in case of spherical harmonics. Two observation types will be treated, that is firstly the gravitational potential itself and secondly the force vector related to it. A full exposition concerning all four types of parametrizations (spherical, oblate and prolate spheroidal and ellipsoidal harmonics) can be found in Appendix C.

6.1. Least Squares Adjustment

The basic principle of least squares can be explained in few sentences. Let $\mathbf{l}$ be the vector of observations, which are related to the functional model parameters $\mathbf{x}$ by means of the design matrix $\mathbf{A}$. Then the system of linear (or linearized) observation equations is represented by

$$\mathbf{l} = \mathbf{A}\mathbf{x}. \tag{6.1}$$

If the number of observations equals that of unknown parameters, the solution is trivially found by applying the Gaussian elimination algorithm or Cholesky decomposition. In case of overdetermined systems, however, different solution techniques are required. Measurement noise causes the linear system to lose its property of consistency. The observation equations are then expressed in terms of the Gauß-Markov model

$$\mathbf{l} + \mathbf{v} = \mathbf{A}\mathbf{x}, \tag{6.2}$$

where $\mathbf{v}$ represents the residual vector, which is assumed to be normal distributed around zero mean. In general, weighting of the individual observations must be performed to account for different accuracies or constraints. The weight matrix $\mathbf{P}$ is the inverse of the cofactor matrix $\mathbf{Q}$ of the observations. When scaled with the a priori variance of unit weight σ_0, they correspond to the covariance matrix $\mathbf{\Sigma_l}$ by

$$\mathbf{\Sigma_l} = \sigma_0^2 \mathbf{Q} = \sigma_0^2 \mathbf{P}^{-1}. \tag{6.3}$$

The fundamental criterion in least squares adjustment is the minimization of the sum of squared residuals. Mathematically put,

$$\mathbf{v}^\mathsf{T}\mathbf{P}\mathbf{v} \stackrel{!}{=} \min. \tag{6.4}$$

Based on this condition, the system of normal equations is found to be

$$\mathbf{N}\hat{\mathbf{x}} = \mathbf{n}, \qquad \mathbf{N} = \mathbf{A}^\mathsf{T}\mathbf{P}\mathbf{A}, \qquad \mathbf{n} = \mathbf{A}^\mathsf{T}\mathbf{P}\mathbf{l}, \tag{6.5}$$

and the best estimation of a set of parameters, denoted by $\hat{\mathbf{x}}$, is given by

$$\hat{\mathbf{x}} = \mathbf{N}^{-1}\mathbf{n}. \tag{6.6}$$

6.2. Observation Equation: Spherical Harmonics

This section demonstrates the usage of least squares adjustment to determine gravitational field coefficients from potential on the one hand, and gravitational acceleration observations on the other hand. For brevity reasons, only the spherical harmonics will be discussed. The treatment including all parametrizations can be found in Appendix C.

We recall the equation of the gravitational potential in spherical coordinates (Eq. 3.22),

$$V(r, \vartheta, \lambda) = \frac{GM}{R} \sum_{n=0}^{N} \sum_{m=0}^{n} \left(\frac{R}{r}\right)^{n+1} P_{nm}(\cos\vartheta) \left[c_{nm} \cos m\lambda + s_{nm} \sin m\lambda\right], \tag{6.7}$$

which is needed to set up the design matrix $\mathbf{A}$. Note that the series is now truncated at a maximum degree N.

Potential

If the observation data are gravitational potential values, the vectors and matrices involved in the least squares adjustment read

$$\mathbf{l} = \begin{bmatrix} V_1 \\ V_2 \\ \vdots \\ V_K \end{bmatrix}, \qquad \mathbf{A} = \begin{bmatrix} \mathbf{A}_c & \mathbf{A}_s \end{bmatrix}, \qquad \mathbf{x} = \begin{bmatrix} \mathbf{x}_c \\ \mathbf{x}_s \end{bmatrix}, \tag{6.8}$$

where $V_k = V\left(r_k, \vartheta_k, \lambda_k\right)$ and

$$\mathbf{A}_c = \begin{bmatrix} \partial V_1/\partial c_{0,0} & \partial V_1/\partial c_{1,0} & \partial V_1/\partial c_{1,1} & \dots & \partial V_1/\partial c_{N,N} \\ \partial V_2/\partial c_{0,0} & \partial V_2/\partial c_{1,0} & \partial V_2/\partial c_{1,1} & \dots & \partial V_2/\partial c_{N,N} \\ \vdots & \vdots & \vdots & \ddots & \vdots \\ \partial V_K/\partial c_{0,0} & \partial V_K/\partial c_{1,0} & \partial V_K/\partial c_{1,1} & \dots & \partial V_K/\partial c_{N,N} \end{bmatrix} \tag{6.9}$$

$$\mathbf{A}_s = \begin{bmatrix} \partial V_1/\partial s_{1,1} & \partial V_1/\partial s_{2,1} & \partial V_1/\partial s_{2,2} & \dots & \partial V_1/\partial c_{N,N} \\ \partial V_2/\partial s_{1,1} & \partial V_2/\partial s_{2,1} & \partial V_2/\partial s_{2,2} & \dots & \partial V_2/\partial s_{N,N} \\ \vdots & \vdots & \vdots & \ddots & \vdots \\ \partial V_K/\partial s_{1,1} & \partial V_K/\partial s_{2,1} & \partial V_K/\partial s_{2,2} & \dots & \partial V_K/\partial s_{N,N} \end{bmatrix} \tag{6.10}$$

$$\mathbf{x}_c = \begin{bmatrix} c_{0,0} & c_{1,0} & c_{1,1} & \dots & c_{N,N} \end{bmatrix}^\mathsf{T} \tag{6.11}$$

$$\mathbf{x}_s = \begin{bmatrix} s_{1,1} & s_{2,1} & s_{2,2} & \dots & s_{N,N} \end{bmatrix}^\mathsf{T} \tag{6.12}$$

The partial derivatives are given by

$$\partial V_k/\partial c_{ij} = \frac{GM}{R}\left(\frac{R}{r}\right)^{i+1} P_{ij}\left(\cos\vartheta\right)\cos j\lambda \tag{6.13}$$

$$\partial V_k/\partial s_{ij} = \frac{GM}{R}\left(\frac{R}{r}\right)^{i+1} P_{ij}\left(\cos\vartheta\right)\sin j\lambda \tag{6.14}$$

From Eq. 6.14 it becomes clear that all zonal s_{ij} coefficients vanish. That is the reason why these are excluded from the parameter vector $\mathbf{x}_s$. This is the most simple case of observation equations. The relation between $\mathbf{l}$ and $\mathbf{x}$ is linear and the derivatives straightforward. In real applications, however, the observable quantity will virtually never be the gravitational potential itself.

Gravitational Acceleration Vector

Introducing the first derivative of the potential as observable, the situation becomes more realistic. The acceleration vector $\mathbf{g}$ is obtained by applying the gradient operator

to the potential V (Chapter 3). We repeat its definition to facilitate the derivation of the observation equations:

$$\mathbf{g}\left(x_1, x_2, x_3\right) = \mathbf{e}_1 \frac{\partial V}{\partial x_1} + \mathbf{e}_2 \frac{\partial V}{\partial x_2} + \mathbf{e}_3 \frac{\partial V}{\partial x_3}. \tag{6.15}$$

The spherical parametrization of the potential is based on the coordinates r, φ, and λ. The definition above requires the partial derivation w.r.t. Cartesian coordinates, though. Finding suitable observation equations is therefore achieved by calculating the total differential of V in order to get an expression dependent on the rectangular coordinates x_1, x_2 and x_3:

$$\mathbf{l}_k = \begin{bmatrix} g_k^{x_1} \\ g_k^{x_2} \\ g_k^{x_3} \end{bmatrix} = \begin{bmatrix} (\partial V/\partial r_k)\,(\partial r_k/\partial x_1) + (\partial V/\partial \vartheta_k)\,(\partial \vartheta_k/\partial x_1) + (\partial V/\partial \lambda)\,(\partial \lambda_k/\partial x_1) \\ (\partial V/\partial r_k)\,(\partial r_k/\partial x_2) + (\partial V/\partial \vartheta_k)\,(\partial \vartheta_k/\partial x_2) + (\partial V/\partial \lambda)\,(\partial \lambda_k/\partial x_2) \\ (\partial V/\partial r_k)\,(\partial r_k/\partial x_3) + (\partial V/\partial \vartheta_k)\,(\partial \vartheta_k/\partial x_3) + (\partial V/\partial \lambda)\,(\partial \lambda_k/\partial x_3) \end{bmatrix}. \tag{6.16}$$

The dependencies of V on the spherical coordinates were omitted due to readability. Note that for every observation "epoch" k, three observation equations are involved which blow up the vector $\mathbf{l}$ to a total size of $3K$ elements. Expressions of the partial derivatives in Eq. 6.16 can be found in Appendix C.

The design matrix $\mathbf{A}$ can subsequently be set up by taking the partial derivatives of the observation equations w.r.t. the unknown coefficients. Without going into details, the formal definition of Eq. 6.9 is stated:

$$\mathbf{A}_c^k = \begin{bmatrix} \partial g_k^{x_1}/\partial c_{0,0} & \dots & \partial g_k^{x_1}/\partial c_{N,N} \\ \partial g_k^{x_2}/\partial c_{0,0} & \dots & \partial g_k^{x_2}/\partial c_{N,N} \\ \partial g_k^{x_3}/\partial c_{0,0} & \dots & \partial g_k^{x_3}/\partial c_{N,N} \end{bmatrix}. \tag{6.17}$$

Matrix $\mathbf{A}_s^k$ is of course obtained analogously. Due to the increased number of observations, the design matrix' number of rows is expanded likewise. The parameter vector $\mathbf{x}$, however, remains the same as in the case of potential observations.

Chapter 7.

Case Studies

In the previous chapters we got acquainted with the necessary tools to perform gravitational field modeling of small bodies. As a logical step further we are now interested in using these tools for determining gravity fields of real bodies. Three asteroids and one comet have been examined in detail, namely

- Asteroid 433 Eros,
- Asteroid 101955 Bennu,
- Asteroid 29 Amphitrite and
- Comet 67P/Churyumov–Gerasimenko.

Eros is an elongated, relatively large asteroid with approximate dimensions of $34 \times 12 \times 12$ km (Miller et al., 2002). It was first visited by the NEAR-Shoemaker spacecraft in 1998 during a close flyby and then again in 2000 for a more comprehensive examination. The probe orbited Eros for one year during which the body was measured and mapped extensively. A landing on the surface concluded the NEAR mission on February 12, 2001. Since the shape of Eros could be determined with very high precision, this asteroid has already been used often times as a case study for small body gravity modeling, cf. (D'Urso, 2013; Garmier and Barriot, 2002; Hu, 2012).

The second body, Asteroid 101955 Bennu, is a small Near-Earth Object with a more regular shape and an average radius of about 250 m (Nolan et al., 2013). It is categorized as one of the top three potential Earth impact events on the Sentry Risk Table[1].

Having a shape similar to that of Bennu, the asteroid 29 Amphitrite stands out for its immense size. The mean diameter measures more than 212 km [2], which makes this body by far the largest among the four. It is, however, the only one that has not yet been visited by a spacecraft. Its shape was estimated based on observations done by the

[1] http://neo.jpl.nasa.gov/risk/index.html
[2] JPL Small-Body Database, http://ssd.jpl.nasa.gov/sbdb.cgi

Infrared Astronomical Satellite (IRAS). A triangulated shape model can be downloaded from the Database of Asteroid Models from Inversion Techniques (DAMIT).

Comet 67P/Churyumov–Gerasimenko became famous in 2014 when Rosetta's mini-labor Philae successfully landed on its surface. It was hence included in our study due to actuality reasons. Out of the three bodies, it is by far the most irregularly shaped one. As mentioned in Chapter 1, it resembles a rubber duck or a dumb-bell because it looks like as if two individual parts were stuck together to one comet.

Several tests were carried out to analyze the accuracy and applicability of the various gravitational field parametrizations. The gravitational effects are evaluated for certain computation points using the forward-modeling technique outlined in Chapter 5. These potential or acceleration values are then used as observations in a least-squares adjustment to determine the harmonic series coefficients for the spherical, spheroidal and ellipsoidal cases. This step is called analysis. On the other hand, the process of using the respective coefficients to compute the gravitational quantities is referred to as synthesis. The differences between the analytically determined values and those resulting from the synthesis allow for the interpretation of the performance of the chosen parametrization. This misfit is introduced as the percentage error $\delta_{(V,g)}$, defined as

$$\delta_V = \left| \frac{V_f - V_b}{V_f} \right| \times 100, \qquad \delta_g = \left| \frac{\|\mathbf{g}_f - \mathbf{g}_b\|}{\|\mathbf{g}_f\|} \right| \times 100. \tag{7.1}$$

The subscripts f and b denote *forward* and *backward*, respectively. Note that δ_g is a scalar and represents the error of the magnitude of the acceleration vector $\mathbf{g}_b$. V, as usual, is the potential.

The computation points are chosen in such way that either all of them are fully, partially or not at all located outside the reference figures. This idea is motivated by the investigation of the performance of the harmonic series *outside* their respective convergence region. In other words, we are interested in finding out, if, for instance, the spheroidal harmonics perform better inside the Brillouin spheroid than the spherical harmonics do inside the Brillouin sphere[3]. Table 7.1 provides an overview of the respective Brillouin figures for every body. Listed is the percentage of how much volume of the reference figure is taken by the polyhedron itself. Ideally, this number would be 100 %. By taking a look at the volume of the Earth[4] and its enclosing sphere[5], this value can found to exceed 99.3 %. As expected, in every of the four cases, the tri-axial reference ellipsoid fits the body best, followed by either the prolate or the oblate spheroid, and finally the sphere. The crucial aspect here shall be outlined more explicitly. Consider a spacecraft's

[3] Brillouin reference figure is the closest circumscribing figure

[4] http://nssdc.gsfc.nasa.gov/planetary/factsheet/earthfact.html

[5] The summit of Ecuadorian mountain Chimborazo is the highest point of the Earth's topography in terms of geocentric distance, see: http://geology.com/records/

orbit about an elongated asteroid. To get the most out of its exploratory mission it is necessary to approach the body as close as possible. The spacecraft's motion is subject to gravity, which must be considered at every stage of the mission by means of, e.g., spherical harmonics. During its approach, however, the orbiter leaves the "comfort zone" of the harmonic series expansion and dives deeper into the so-called divergence region. As a consequence, the gravitation model might become erroneous. Obviously, the use of spheroidal or ellipsoidal harmonics would reduce respective divergence regions. The dimensions of the respective reference figures are listed in Appendix D.

Body	Sphere	Oblate S.	Prolate S.	Ellipsoid
433 Eros	10.4 %	24.0 %	26.2 %	33.8 %
101955 Bennu	55.1 %	60.1 %	61.0 %	66.3 %
29 Amphitrite	62.1 %	70.3 %	64.3 %	72.7 %
67P Chury	21.7 %	31.5 %	35.6 %	39.7 %

Table 7.1.: Percentage of the total reference figure's volume taken by the body.

7.1. Asteroid 433 Eros

7.1.1. Shape and Gravity

We start off with Asteroid 433 Eros and present in Figure 7.1 its shape as well as the gravitational field and three orthogonal projections of the reference figures. The axes of the coordinate system are chosen in such way, that the X-axis passes through the elongated part of the body, the Z-axis approximates the axis of rotation and the Y-axis completes the right-handed system (Figure 7.1d). The shape model consists of 1708 faces and was downloaded from the Planetary Data System provided by NASA. The gravitational field around Eros visualized in sub-figures 7.1a-7.1c was obtained via the polyhedron method. Shown are potential values, which are in the range of few decajoules per unit mass. Translated into gravitational acceleration values this means a maximum field strength of about $5.5\,\mathrm{mm\,s^{-1}}$. This is in the same order of magnitude as the gravitational attraction due to the Sun for a particle on the Earth's surface. The ellipses (and circles) in these figures represent projections of the four reference figures, i.e., the sphere (S), the oblate (O) and the prolate (P) spheroid as well as the tri-axial ellipsoid (E). All four share the same origin[6]. The visualization practically speaks for itself and emphasizes once more the unsuitability of the sphere to approximate such bodies.

[6]Due to this fact, the used reference figures are strictly speaking not the best fitting reference figures.

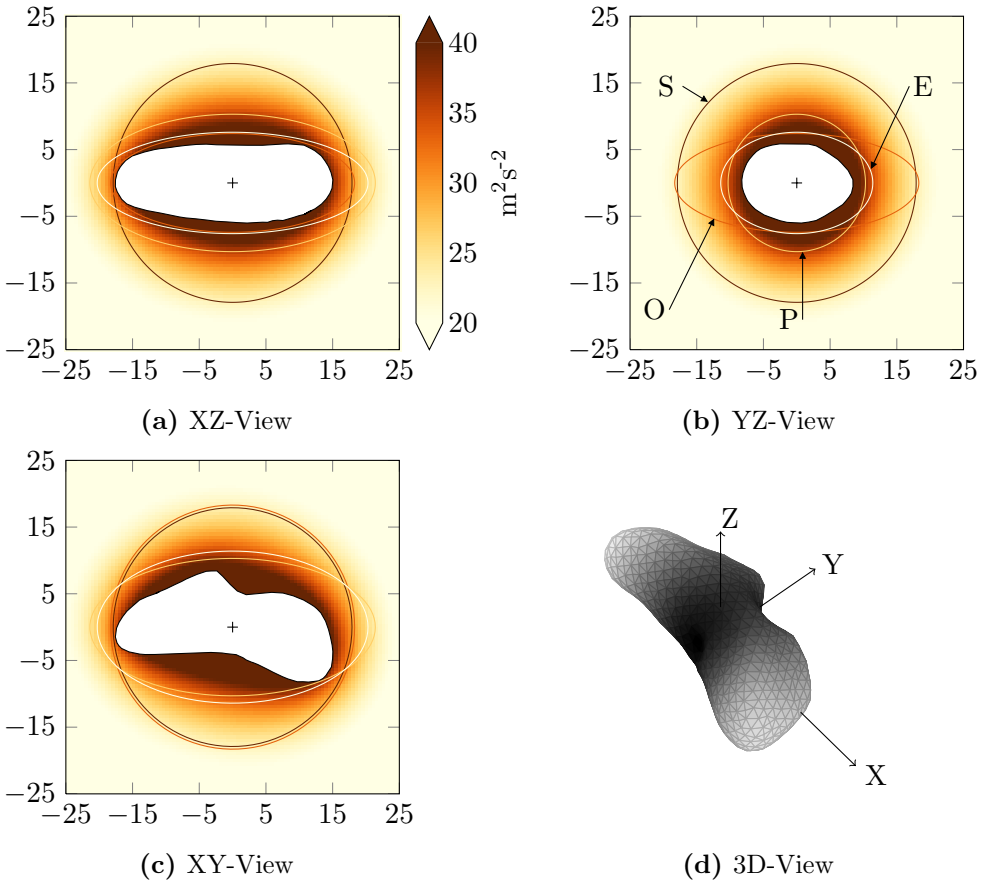

(a) XZ-View

(b) YZ-View

(c) XY-View

(d) 3D-View

Figure 7.1.: Visualization of the polyhedral shape model of 433 Eros and the gravitational field in its environment. Indicated by ellipses are the four reference figures, i.e., the sphere (S), the oblate (O) and prolate (P) spheroid and the ellipsoid (E). Units are kilometers.

7.1.2. Accuracy inside Convergence Region

A sphere with radius $R = 25\,\mathrm{km}$ enclosing all four reference figures is used in order to test the accuracy of the various methods. The calculation points are evenly distributed on the sphere's surface by means of the so-called Reuter grid. In contrast to the widely used geographical grid, this point distribution algorithm sophisticatedly reduces the number of points while enhancing a uniform arrangement (Eicker, 2008). The resolution of grids is defined by the control parameter L, which was found to be related to the maximum obtainable degree of a harmonic series by

$$L \Leftrightarrow N + 1. \tag{7.2}$$

Figure 7.2 exemplarily illustrates a Reuter grid $L = 5$ on the exterior sphere. Compared to the geographical grid, the point density is loosened due to the equi-distant characteristic of the Reuter grid, especially near the poles. To guarantee for strongly overdetermined normal equation systems we used the grid resolution paremter $L = 41$ in our test series.

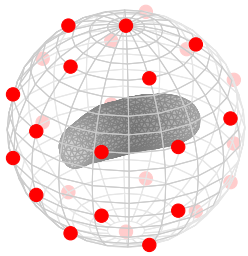

Figure 7.2.: Distribution of computation points on a sphere using the Reuter grid.

The true potential is approximated by means of the four harmonic series with expansions up to degree $N = 10$. In order to make statements about the accuracy we take a look at the percentage error δ_V. The error values are interpolated on a regular grid and plotted as two-dimensional maps (Figure 7.3). As indicated by the colored scale-bar, the true field could be estimated with an average accuracy better than one percent in all four cases. Nevertheless, noticeable differences between the solutions can be observed. The upper left image represents the deviations related to the spherical harmonics solution. A significant, circular pattern with two "centers" strikes the eye. These circle centers represent the locations at which the distance between evaluation sphere and the body's topography is minimal, i.e., the *tail* and the *nose* of Eros. The wave-like propagation

probably results from truncating the series expansion at such low degree and is further explainable by the choice of the evaluation surface, and hence the fact that the distance between the data points and the reference figure is always constant. This is no longer case for the the three alternative parametrizations. Sub-Figure 7.3b reveals a zebra stripes-like error pattern associated with the oblate spheroidal representation. As we have seen in Figure 7.1, the reference spheroid fits the body best near the poles. This fact is mirrored in the characteristics of the truncation error. The highest accuracy of the gravitational field is obviously obtained at latitudes higher or lower $\pm 50°$. Everywhere else, the errors are in the same order of magnitude as the spherical harmonics. The most influencing factor is again the closeness to the tail of the asteroid at about $180°$ longitude. The maximum errors, however, are located near the equator at about $-100°$ longitude. At this point, the "free air" distance on a line connecting the reference spheroid's surface and the expansion center is obviously larger than anywhere else (see Fig. 7.1). This effect is even clearer seen when regarding only the first two or three degrees of the series expansion. Moving on to the prolate case, we see an overall decrease in the errors compared to the first two methods. The smallest distance between the prolate reference spheroid and the asteroid is in the equatorial plane at around $-31°$ longitude. Nevertheless we recognize a similar pattern as seen in the other sub-figures, i.e., an error pattern centered at $(0,0)°$. In fact, the oblate and prolate errors are distributed somehow inversely. This also makes sense, since the above mentioned "free air" distance is also in the prolate case very large near this dominating part. The same applies to the ellipsoidal harmonic representation, shown in the lower right image. As expected, the overall accuracy of this solution turned out to be the best.

In addition to the uniform point distribution on the spherical surface, also real orbit data of the NEAR Shoemaker spacecraft is used to simulate a more realistic scenario. Figure 7.4a shows a seven-day orbit of the spacecraft w.r.t. the Eros-fixed coordinate system. The mean length of the semi-major axis is about 50 km. The orbit was integrated with a one minute time step using data provided by the PDS. For details, the reader is referred to (Miller et al., 2002, Table I). Due to the orbit characteristics, the computation points are located very far from the attracting masses causing the gravitational force to become exceedingly weak. Similar results as compared to the uniform spherical point distribution can be obtained. The "worst" solution is again the spherical harmonics field and the "best" the ellipsoidal representation. The quotation marks are used, because worst is a very strong word when speaking of errors smaller than 10ppb (parts per billion). In Figure 7.4b the error δ_V associated with the spherical harmonics solution is visualized in terms of ground track paths on a two-dimensional map. We recognize immediately the same pattern as in Sub-Figure 7.3a. The magnitude of the errors is of course smaller due to the damping of the higher frequencies at increased distance from the masses. The corresponding figures referring to the spheroidal and ellipsoidal solution are skipped for the sake of brevity.

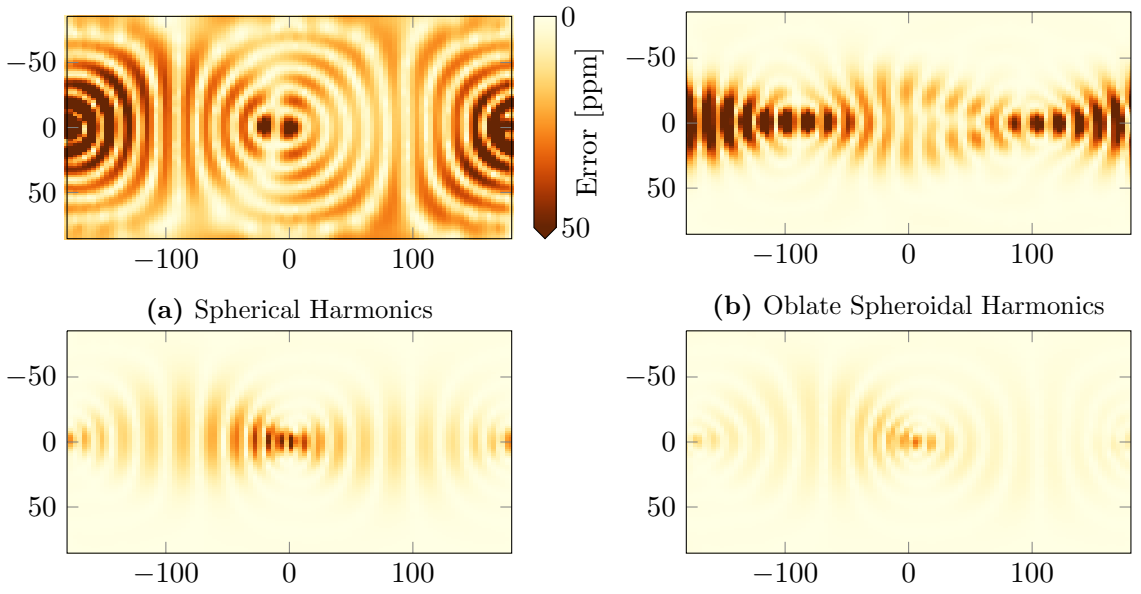

(a) Spherical Harmonics

(b) Oblate Spheroidal Harmonics

(c) Prolate Spheroidal Harmonics

(d) Ellipsoidal Harmonics

Figure 7.3.: 2D-map of errors of the gravitational potential modeled by means of spherical, spheroidal and ellipsoidal harmonics with an expansion up to degree 10 in comparison with the forward modeled potential. Units are parts per million (10 ppm = 0.001 %). Axes ticks are longitude and latitude values in degrees.

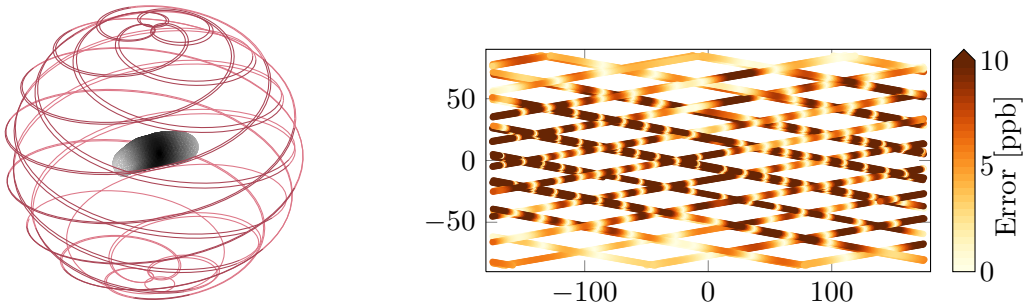

(a) 7-days orbit

(b) SH errors

Figure 7.4.: Visualization of the NEAR shoemaker trajectory w.r.t. the Eros-fixed coordinate system (left image) and the errors due to SH approximation in terms of a ground track plot (right image).

We have seen in Figures 7.3 and 7.4 that the greatest error sources are associated with the high frequency content of the gravitational field near the ends of the asteroid. By regarding higher degrees in the computation of the harmonics series we expect these errors to decrease. To confirm our hypothesis, the analysis and synthesis processes are carried out for different degrees n for both the data sphere (Fig. 7.5a) and the orbit (Fig. 7.5b). In these figures, the root mean square (RMS) of the percentage errors δ_V of each solution is displayed as a function of the degree n. The solid and dashed lines proof indeed beautifully the convergence of the four harmonic series towards the true potential and acceleration values, respectively. The errors resulting from the approach of using gravitational acceleration values as observables are consistently larger throughout. By recalling the fact, that the acceleration vector is obtained by taking the gradient of the potential, this systematic offset is explained immediately. Differentiating a function in the time (or spatial) domain means emphasizing the higher frequencies in the frequency domain. As a consequence, a much larger number of polynomial terms is needed in order to attain the same accuracy as for potential observations. Let us first focus on the left image in 7.5 and the uniform point distribution on the sphere. The forward-backward simulations were carried out up to degree $N = 15$. The legend explaining the color code makes use of the following abbreviations:

- SH: Spherical Harmonics,
- OH: Oblate Spheroidal Harmonics,
- PH: Prolate Spheroidal Harmonics,
- EH: Ellipsoidal Harmonics.

The geometrical similarity of the reference figures belonging to SH and OH as well as PH and EH is mirrored by the adjacency of the respective lines. Put differently, the convergence of the PH and the EH takes place at noticeable faster pace than the SH and the OH. The EH field of resolution $N = 10$, for instance, is more accurate than the SH field of resolution $N = 13$. However, at lower degrees, say $N < 6$, the four parametrizations perform similarly. No significant improvement is achieved by choosing EH or PH over SH. The maximum errors (not visible at this scale) occur in the solutions $N \leq 1$ and are in the order of 5 % for potential and 15 to 19 % for acceleration values. The OH solution sticks out with acceleration RMS values of about 25 %.

Sub-Figure 7.5b shows the analogous graph obtained by using orbit trajectories as calculation points. All lines drop rapidly and converge very fast to the true potential. We repeat again, that this fast convergence is of course due to the strongly attenuated gravitation at these positions. The graph reveals the same order of the various solutions, the differences between these lines are comparably small, though. As indicated by the horizontal axis, the series were truncated already at a maximum of $N = 10$. This is due to singularity issues in the progress of estimating the series coefficients. To be more

precise, the normal equations in spheroidal and ellipsoidal parametrizations involved in the least squares adjustment became non-invertible when including degrees $N > 12$. The complexity of the underlying coordinate systems causes the elements of the design matrix to range over many orders of magnitudes. This ill-conditioning is again worsened by the unequal spatial distribution of the data points due to the characteristics of the orbit. Thus, we draw the conclusion that SH should be preferred over the other harmonics if all data points are located significantly far outside the attracting masses and, of course, the Brillouin sphere.

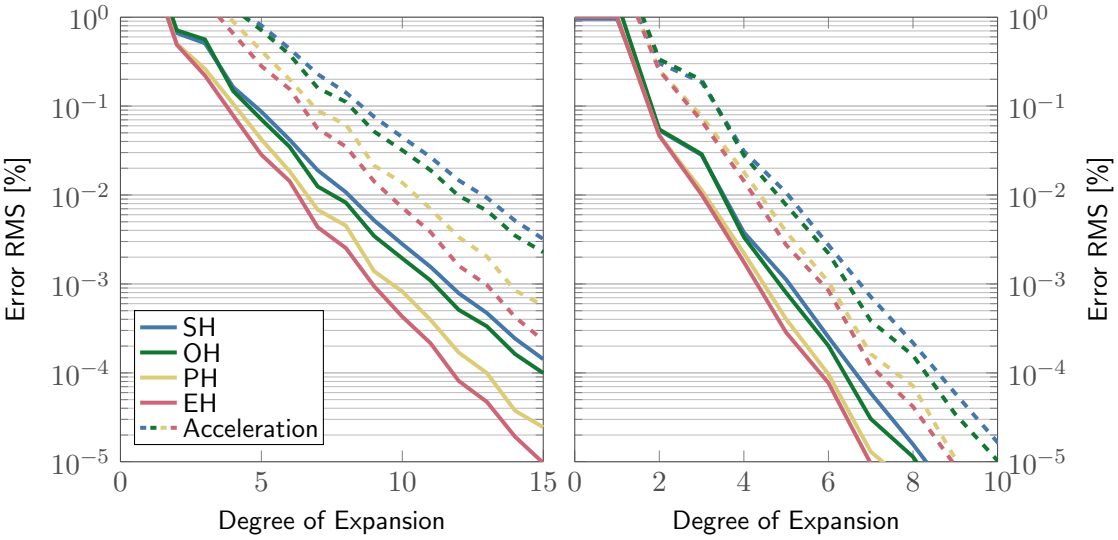

(a) Sphere **(b)** Orbit

Figure 7.5.: RMS of the percentage errors for different series expansion maxima. The solid lines represent gravitational potential while the dashed ones indicate gravitational acceleration.

7.1.3. Influence of Measurement Noise

Up until now, the only limiting factors in the computation of the various representation have been numerical and computational capacities. In reality we will never have the pleasure to deal with completely noise-free observations, though. Every instrument has a limited range of accuracy and reliability in which it is guaranteed to work under most circumstances. We are interested in finding out what influence measurement noise has on the four parametrizations. White noise with standard deviations of (i) $\sigma = 10^{-9}\,\mathrm{m\,s^{-2}}$ and (ii) $\sigma = 10^{-6}\,\mathrm{m\,s^{-2}}$ has been added to the forward-computed acceleration values obtained at the regularly distributed points on the sphere. Figure 7.6 depicts the percentage

error as a function of the expansion degree N obtained using the noisy observations. The dashed lines are the corresponding noise-free observations. The series were again truncated at $N = 15$. In these low order harmonics, the small noise of $\sigma = 10^{-9}\,\mathrm{m\,s^{-2}}$ has no visual effect on the SH and OH. The EH and PH curves become flatter for degrees higher than $N = 13$. What this means is clearer visible in Sub-Figure 7.6b. This noise level only allows gravitational field models with an accuracy not better than 0.25 %. Compared to SH and OH, the expansion degree required to reach this accuracy is obviously smaller for PH and EH.

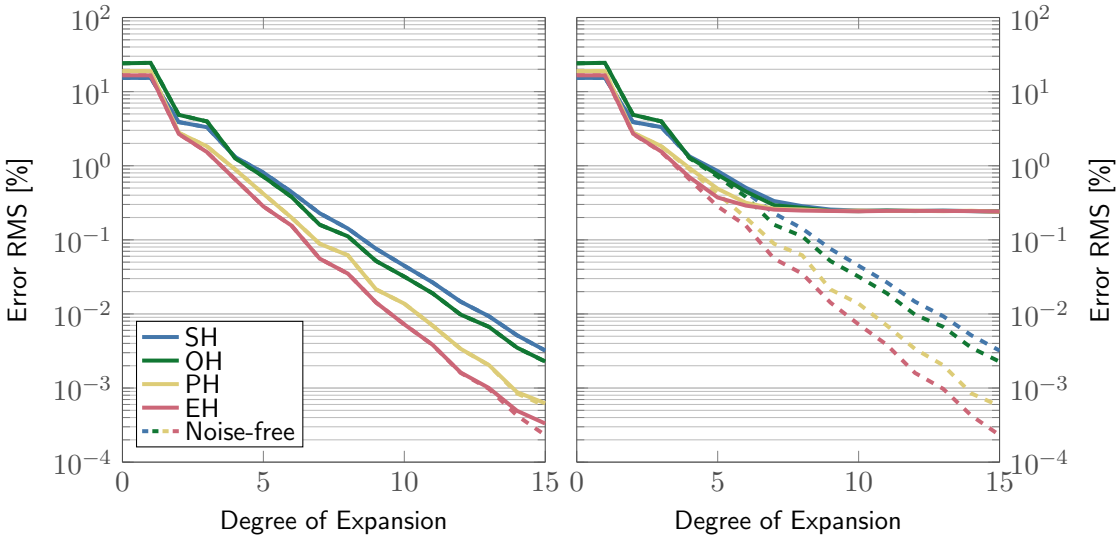

(a) $\sigma = 10^{-9}\,\mathrm{m\,s^{-2}}$ **(b)** $\sigma = 10^{-6}\,\mathrm{m\,s^{-2}}$

Figure 7.6.: RMS error curves showing the influence of measurement noise.

7.1.4. Accuracy inside Divergence Region

In this section we will try to assess the accuracy or reliability of the different methods inside the divergence regions, i.e., inside the respective Brillouin figures. The computation points are distributed on the surface of the asteroid using a Reuter grid with $L = 41$ and the spherical harmonics shape model of Eros, which is obtainable from the PDS. The forward-backward computation is carried out in completely the same manner as before and the RMS values of the resulting errors are compared graphically. Instead of letting the expansion degree vary, only two cases are considered, i.e. $N = 5$ and $N = 15$. In order to account for different "levels" of divergence, the radial component of the evaluation points is increased constantly until all points are located outside all reference figures again. For every intermediate, puffed up pseudo-surface, the RMS determination

process is repeated. This admittedly rather cumbersome approach has the advantage of irregularly distributing the computation points both inside and outside the convergence regions. When thinking of a spacecraft navigating in close proximity of a small body, this mixed configuration is certainly a realistic scenario.

Figure 7.7 depicts the results of this investigation. The horizontal axis indicates the increase in the radial coordinate, i.e., the distance from the surface of the body. The maximum is 15 km. Caution must be taken when analyzing the lines and areas because two different ordinates are used. The filled areas belong to the axis on the right-hand side of the figure. They represent the percentage of data points located *inside* the respective convergence regions, i.e., outside the reference figures. Beginning from the left, a dramatic increase in the percentage related to the oblate spheroid at about 2 km is the first thing that catches the eye. This comes at no surprise because the spheroid fits the body best along the X-axis (Fig. 7.1). In addition to that, the equal spacing property of the Reuter grid is only valid on the sphere. The elongated shape of Eros hence causes the point density around the poles to be significantly higher than at the ends of the body. As a consequence, most data points are pushed outside the divergence region very fast. This sharp rise is attenuated at about 5 km and the percentage is increased at much slower pace afterwards. As expected, the ellipsoid fits the body best and after only 5 km more than 80 % of the points are located at its outside. The colored area belonging to the prolate spheroid shoots up at about 4 km and reaches the 100 % mark shortly after. The corresponding area of the sphere is yet another evidence of its ineptness. After 10 km still more than 70 % are inside the spherical harmonics' divergence region.

Let us now move on to the line plots in this figure and thus the already known RMS values of the percentage error. As seen in the logarithmically scaled left axis, the errors range over several orders of magnitude. The group of the four distinct lines in the upper part of the figure, i.e., errors greater than 10^{-2} %, represent the $N = 5$ solutions. The lower four lines are the RMS values of the $N = 15$ solutions. Let us first comment on the latter. In close proximity to the surface, say distances smaller than 3 km, all four parametrizations suffered singularity issues during the LSA progress. This is explainable by the very definition of the harmonic series, i.e., the guaranteed convergence outside the circumscribed reference figure. This uncertainty in the solution is seen especially clear for EH in the unsteady decline of the errors in the first few kilometers where almost 100 % of the data points are inside the divergence region. Nevertheless, even directly on the surface the true field can be represented by means of OH, PH and EH with an average accuracy of better than 1 %. Maximum errors range from 15 to 20 % and relativize the deceivingly small RMS values though. PH and EH steadily converge with increased radial distance. No significant improvement is obtained when choosing EH instead of PH. In fact, between 2.5 and 5 km, the two lines are barely distinguishable from each other even though the number of points inside the EH's convergence region exceeds that of the PH by far. In accordance with the area plot of the OH, the corresponding RMS

values are reasonably small near the surface. In the following, however, the line falls only slowly until it is even equal to the SH solution at about 11 km. The oblate spheroid is obviously an inappropriate choice for this asteroid, especially due to the large deviations in the equatorial plane. As expected, SH solutions are worst near the topography but still converge steadily with almost constant offset of about one order of magnitude compared to PH and EH.

Regarding the SH, PH and EH solutions, a similar picture can be observed when the series is truncated at $N = 5$. The overall errors are of course significantly larger, because high frequent content near the surface cannot be modeled adequately with such low resolution. The aforementioned offset between the lines is equally well seen in this case. A very interesting feature is the somewhat mirrored course of the PH and EH curves over the first 3 km. The symmetrical blow-up effect lets points located at near $-31°$ longitude first leave the prolate spheroid causing a short drop of the PH errors. In the meantime, more and more points leave the EH's divergence zone which yields a gently falling curve. What really strikes the eye, though, is the curve characteristic of the OH errors. Over the first 10 km, it remains relatively stable or even rises a little. Even afterwards, convergence takes place rather unshapely proving once more the inadequateness of the OH for this asteroid.

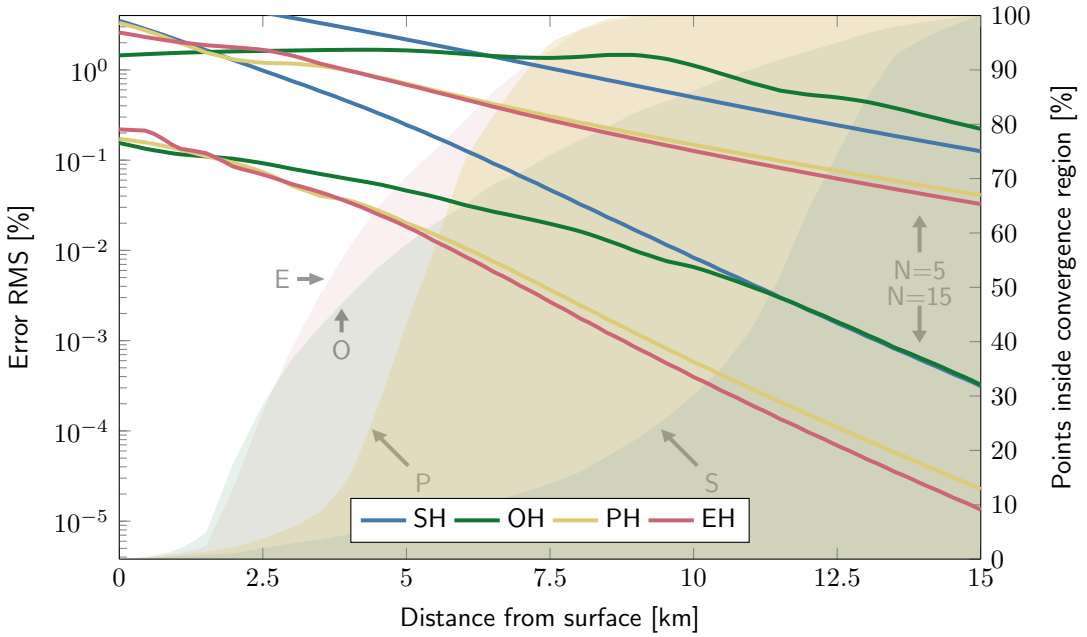

Figure 7.7.: RMS values of SH, OH, PH and EH for points distributed irregularly inside and outside the respective convergence regions. S, O, P, E are the reference figures.

7.2. Asteroids 101955 Bennu and 29 Amphitrite

Both asteroids are more regular than 433 Eros and are thus treated simultaneously in this section. Figure 7.8 is a visual comparison of the polyhedral shape models and shows the two bodies side by side in the XZ-plane. Magnification by a factor of 350 was applied to Bennu to enable making out details. Amphitrite's shape model is coarse and irregular. The flat poles make the oblate spheroid a very good fit (Table 7.1), Bennu's shape is almost equally well approximated by the oblate and prolate spheroid.

Let us say some words about the gravitational field of the two bodies. Bennu is in fact just a *tiny* rock. An analogous comparison as before reveals a maximum field strength of 8.5 mGal, i.e., $8.5 \times 10^{-5}\,\mathrm{m/s^2}$. Deviations of the normal gravity field of the Earth are usually expressed in this unit. Amphitrite is one of the largest asteroids known in our solar system. Its gravitational field is almost one thousand times stronger than Bennu's. The maximum acceleration of $8.2 \times 10^{-2}\,\mathrm{m/s^2}$ is equal to that of the Earth at an altitude of about 70 000 km, which is almost twice the orbital altitude of geostationary satellites.

The investigation of the accuracy is performed analogously to Eros. For the sake of brevity, however, only the convergence tests in the regular case (i.e., all points are located outside the Brillouin figures) are presented here. The points are distributed on spheres in the same manner as before. In order to make results comparable to those of Eros, the sizes of these spheres are chosen in such way that the ratio between the radii of the Brillouin and the data spheres is equal to the corresponding ratio of the spheres associated with Eros. Thus, all points are inside the respective convergence regions. Figure 7.9 confirms what we had expected from the geometry. Compared to the elongated asteroid Eros, the four curves associated with the various parametrizations lie close together. EH perform best, followed by OH, PH and SH. Asteroid Amphitrite is more oblate, the EH and OH perform similarly well and keep the other solutions at a distance. Especially for degrees higher than $N = 6$, the two groups of curves drop at different paces. An interesting characteristic of the Bennu solutions is the stair-like course of the RMS lines. It seems like even expansion degrees contribute stronger to fast convergence than odd ones. This statement, however, is just a visual interpretation and is not based on thorough research.

In Chapter 4 it was stated that the size of the body is especially crucial for determining EH series components. In accordance with Figure 4.6, the maximum degree of $N = 15$ could be computed for both Bennu and Amphitrite.

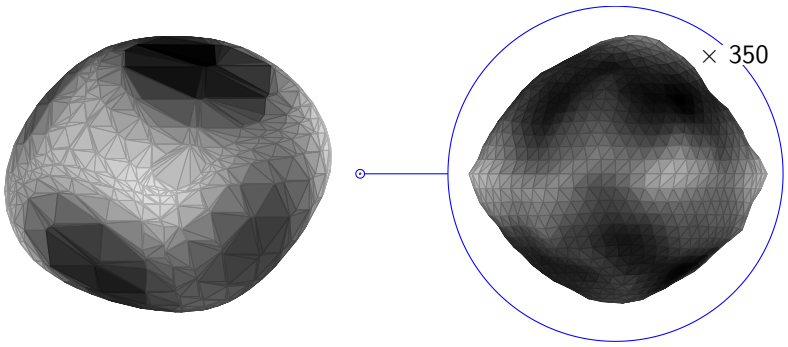

Figure 7.8.: Comparison of Asteroid 29 Amphitrite (left) and 101955 Bennu (right).

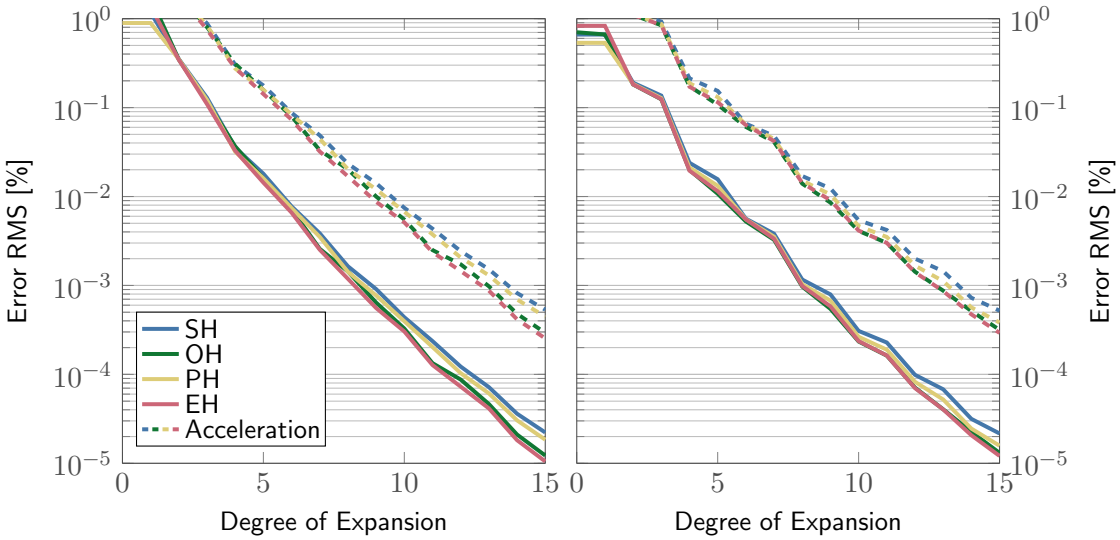

(a) Amphitrite **(b)** Bennu

Figure 7.9.: RMS of the percentage errors for Amphitrite (left) and Bennu (right).

7.3. Comet 67P/Churyumov–Gerasimenko

7.3.1. Shape and Gravity

The last object in this test series is Comet 67P/Churyumov–Gerasimenko. Never before had a comet been studied as meticulous as the Rosetta mission did with Chury in 2014. Figure 7.10 is again a visualization of the shape model, the reference figures and the gravitational field. The divergence regions are similarly large as for 433 Eros and the prolate spheroid is again a comparably good fit for the body. The gravitational field's maximum strength of about 19 mGal is exerted near the larger lobe of the comet.

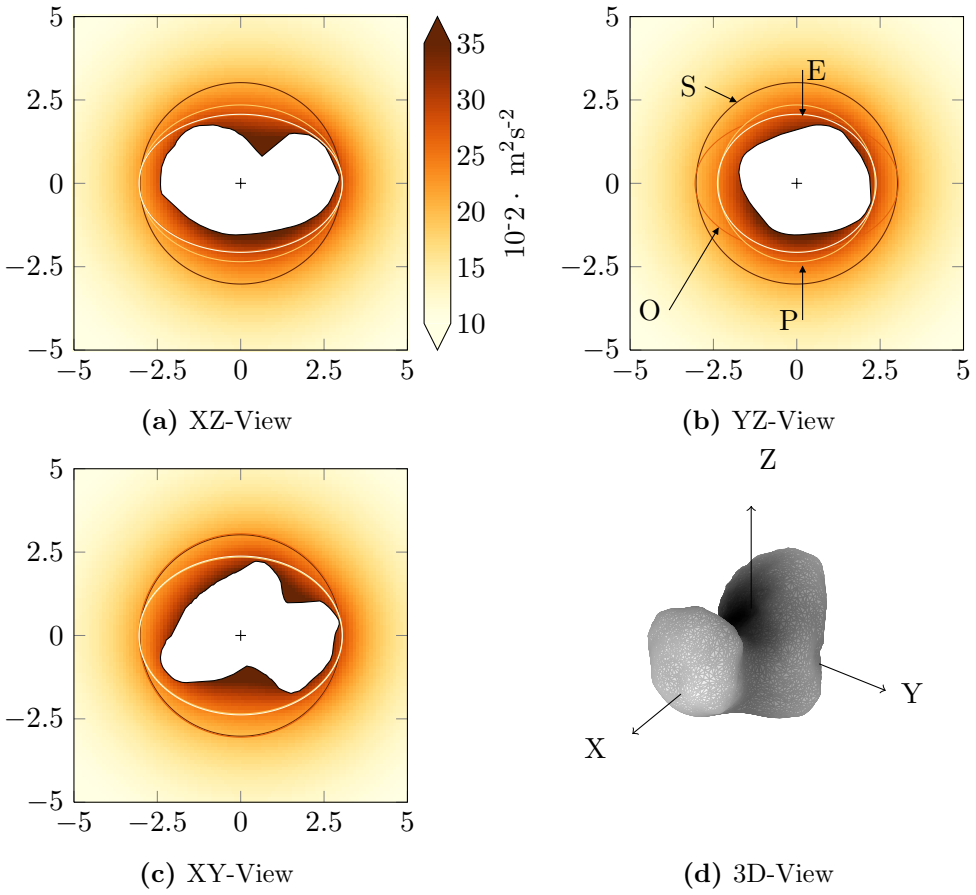

(a) XZ-View **(b)** YZ-View

(c) XY-View **(d)** 3D-View

Figure 7.10.: Visualization of the polyhedral shape model of 67P/Churyumov–Gerasimenko and the gravitational field in the body's environment. Indicated by ellipses are the four reference figures, i.e., the sphere (S), the oblate (O) and prolate (P) spheroid and the ellipsoid (E). Units are kilometers.

7.3.2. Accuracy inside Convergence Region

The computation points are again distributed using a Reuter grid on a sphere enclosing all four reference figures. The RMS values of the errors $\delta_{(V,g)}$ are visually compared in Figure 7.11. We immediately observe a very similar behavior of the PH and EH curves. The two graphs are visually almost identical. This applies for both the potential and the acceleration approaches. The OH perform only a little better than the SH, especially at higher degrees. Fast convergence is given by all four solutions due to the attenuated field strength at the evaluation points.

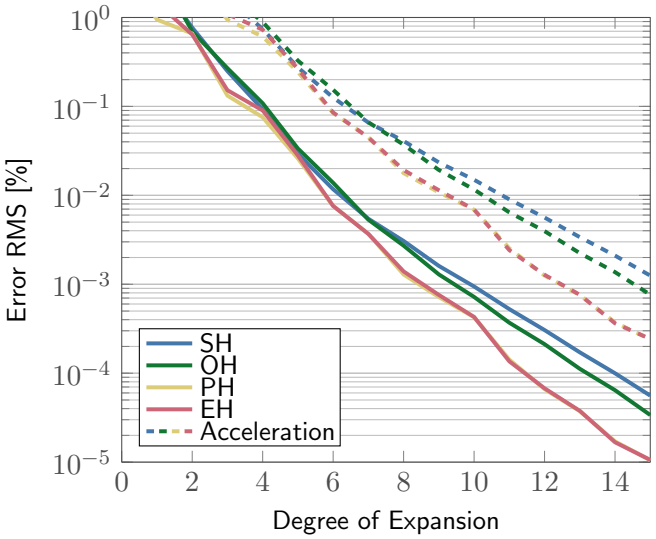

Figure 7.11.: RMS of percentage error of 67P/Churyumov–Gerasimenko.

7.3.3. Free Fall Simulation

A last test was carried in order to get a better understanding of the influence of divergence on the various solutions. A particle located at $r = 4000\,\mathrm{m}, \vartheta = 45°, \lambda = 45°$ with unit mass was "thrown" with an initial velocity of $1\,\mathrm{m\,s^{-2}}$ in direction of the origin. The trajectory of the particle is determined via numerical integration of the acceleration vector. The gravitational acceleration was computed using (i) the polyhedral method, (ii) SH, (iii) OH, (iv) PH and of course (v) EH . The respective series coefficients are estimated a priori from data points located strictly inside the convergence regions. The maximum degree of expansion is set to $N = 15$.

Figure 7.12 visualizes the different trajectories. Emphasized is the area around the true

impact location. It is located in the valley between the two individual parts of the comet. This area is especially deep inside the divergence regions of each of the four parametrizations. As a consequence, the final impact locations differ more or less from the true location. The SH trajectory begins to drift away from the others at an altitude of about 900 m. It makes a bend before intersecting the surface 273 m in terms of Euclidean distance from where the true intersection point is. Clearly better results are obtained with the other parametrizations. The distance from the EH impact location is only 40 m, that of OH and PH both 96 m although at different positions. The Euclidean distance may be a sub-optimal quality criterion here, because the straight line connecting the positions often cuts through the polyhedron or runs through the "air" and makes the distance apparently shorter. It does, however, still support the main message of the investigation, namely, the unsuitability of the SH to model the gravitational field near irregularly shaped bodies.

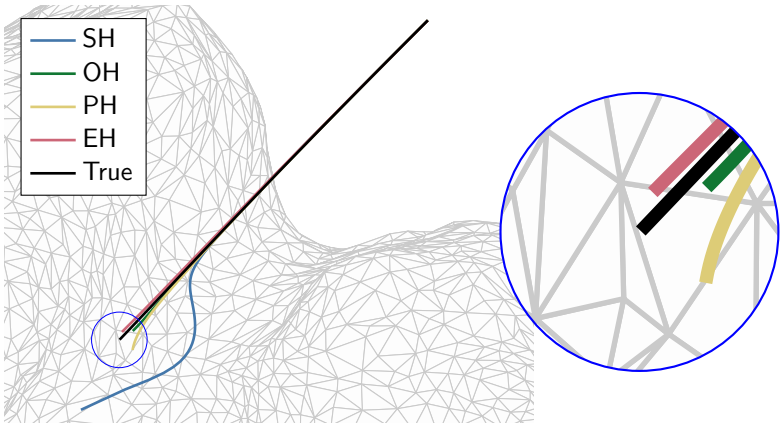

Figure 7.12.: Free fall trajectories computed via polyhedral method, SH, OH, PH and EH.

Chapter 8.

Conclusions

The gravitational field of small solar system bodies can be modeled in different ways. The polyhedron method is a powerful tool for determining the gravitational attraction of an oddly shaped body. The computation points may be located far outside the body, near it or even on its surface. The only limiting factors here are the resolution of the three-dimensional shape model and, of course, the rather vague assumption of a constant density distribution inside the body. The inverse way, i.e., using observations made on the outside of the attracting body to draw conclusion of its inside is referred to as backward modeling. The classical approach in Geodesy to perform this task is by making use of spherical harmonics. The irregular shape of asteroids and comets, however, leads to large areas of divergence, which results in unreliable results for computation points located near the body's surface. Spheroids or tri-axial ellipsoids, on the other hand, approximate the shape of small bodies relatively well. More or less complicated curvilinear coordinate systems attached to these figures are used in order to derive the solutions of Laplace's equation in this alternative parametrizations. They are called spheroidal and ellipsoidal harmonics. While oblate spheroidal harmonics are already well established for the purpose of gravitational field modeling, the prolate counterpart is rarely seen in the literature. Since the shaping process of small bodies does or did not follow any particular rules, some asteroids might be better approximated by an oblate spheroid while others snugly fit into a prolate one. The best geometrical fit, however, will always be obtained by means of a tri-axial ellipsoid. The theory of ellipsoidal harmonics goes back to the 19^{th} century, practical aspects and the applicability of these functions have only recently been investigated, though.

In this thesis, we got acquainted with the theory of the four gravitational field parametrizations and studied the computational aspects of the underlying basis functions. Spheroidal harmonics make use of the Associated Legendre Functions of the second kind in order to represent the radial solution of Laplace's equation. Fast and effective recurrence relations exist, which allow for applying these harmonics to differently shaped and sized spheroids. With increasing expansion order, however, numerical issues may arise due to the rather large exponents of these numbers. Even though we did not encounter such

problems, the possibility of arithmetical over- or underflow must be considered. Even more complex is the process of computing the basis functions of the ellipsoidal harmonics, i.e., the Lamé functions of the first and second kind. A first obstacle that needs to be overcome is the ambiguous coordinate transformation between the Cartesian and the ellipsoidal coordinate system. While this problem is taken care of fairly easily by using an expression dependent on signed Cartesian coordinates, another one is already around the corner. In contrast to the other parametrizations, no elegant recurrence formula is known that would enable a fast computation of the Lamé functions. Quite the opposite is the case. Various integrals must be solved and exceedingly large exponents handled. In addition to that, the maximum computable degree of the expansion was found to depend strongly on the size of the reference ellipsoid.

We tested the different gravitational field parametrizations on four small bodies: three asteroids, varying in shape and size, and one comet, being of interest due to recent events. Asteroid 433 Eros and comet 67P/Churyumov–Gerasimenko are heavily irregular shaped and best approximated by a tri-axial ellipsoid from a geometrical point of view. The other two bodies are more sphere-like, but 29 Amphitrite is incomparably larger than 101955 Bennu. The series coefficients are computed via least-squares adjustment based on forward-modeled potential or acceleration values. The accuracy of the so obtained approximated gravitational fields is assessed by comparison with the true field. The results proved indeed, that ellipsoidal and spheroidal harmonics converge faster to the true potential as opposed to the traditional spherical harmonics. Especially the odd shapes of the two previously mentioned bodies yield to an improvement in accuracy of about one order of magnitude. Of particular interest are the results related to 67P. The prolate spheroidal parametrization turns out to be just as accurate as the ellipsoidal one. This means that the laborious procedure of computing the Lamé functions can be avoided by making use of the much simpler Legendre functions - without loss of accuracy. Nevertheless, the gravitational field of more regularly shaped bodies like Bennu or Amphitrite is almost equally well determined by means of spherical harmonics. Due to the simplicity of the basis functions and the fact that the size of the reference sphere has no great impact on the computability of those, the spherical harmonics might still be the best choice here.

While many aspects of small body gravity field modeling have been dealt with in this thesis, there is still a lot of research to do in the future. Within this work, the density of the small bodies has always been assumed to be constant. In reality, this will virtually never be the case. Hence, one direction that might be taken in future is the inclusion of a density model during the process of evaluating the gravitational effects of the polyhedral shape model. The theoretical concept is fairly easy: the total potential simply results from summing up individual potentials corresponding to different densities. The availability of such mass distributions is the critical factor here. However, the Rosetta spacecraft and its lander Philae will examine Comet 67P/Churyumov–Gerasimenko ex-

tensively over the next few months, following the comet as it approaches the Sun. The increased temperature will cause the comet to outgas and to change its physical and even geometrical properties. As a consequence, also the gravity field of the comet changes with time. Rosetta will observe this process and the backward-modeling approach might even allow for making coarse assumptions of the mass distribution inside the body.

Ellipsoidal harmonics are unhandy and complicated. The advantages of this parametrization cannot be denied, though. Future research might lead to simplified algorithms to compute the Lamé functions, which would doubtlessly make the ellipsoidal harmonics the best choice when it comes to representing the gravity field of irregularly shaped bodies.

Bibliography

Balmino, G. et al. (Dec. 1991). "Simulation of gravity gradients: a comparison study." In: *Bulletin Géodésique* 65.4, pp. 218–229.

Bardhan, J. and M. Knepley (2012). "Computational science and re-discovery: open-source implementation of ellipsoidal harmonics for problems in potential theory." In: *Computational Science & Discovery*.

Byerly, W. E. (1893). *An elementary treatise on Fourier's series*. Boston, Ginn & Company.

Colombo, O. (1981). *Numerical methods for harmonic analysis on the sphere*. Tech. rep. Department of Geodetic Science, The Ohio State University.

Dassios, G. (2012). *Ellipsoidal harmonics: theory and applications*. Cambridge University Press.

Davis, D. et al. (2002). "Collisional evolution of small-body populations." In: *Asteroids III*.

Dechambre, D. and D. Scheeres (2002). "Transformation of spherical harmonic coefficients to ellipsoidal harmonic coefficients." In: *Astronomy and astrophysics*.

Dobner, H.-J. and S. Ritter (1998). "Verified computation of Lamé functions with high accuracy." In: *Computing*.

D'Urso, M. G. (Oct. 2013). "Analytical computation of gravity effects for polyhedral bodies." In: *Journal of Geodesy* 88.1, pp. 13–29.

Eicker, A. (2008). *Gravity field refinement by radial basis functions from in-situ satellite data*. Tech. rep. Univ. Bonn, Inst. für Geodäsie und Geoinformation.

Fukushima, T. (2013). "Recursive computation of oblate spheroidal harmonics of the second kind and their first-, second-, and third-order derivatives." In: *Journal of Geodesy*.

— (2014). "Prolate Spheroidal Harmonic Expansion of Gravitational Field." In: *The Astronomical Journal*.

Garmier, R. and J.-P. Barriot (Apr. 2001). "Ellipsoidal Harmonic expansions of the gravitational potential: Theory and application." en. In: *Celestial Mechanics and Dynamical Astronomy* 79.4, pp. 235–275.

— (2002). "Modeling of the Eros gravity field as an ellipsoidal harmonic expansion from the NEAR Doppler tracking data." In: *Geophysical research ...*

Gaskell, R. (2013). "Gaskell Tethys Shape Model V1. 0." In: *NASA Planetary Data System*.

Hobson, E. W. (1931). *The theory of spherical and ellipsoidal harmonics*. CUP Archive.

Hofmann-Wellenhof, B. and H. Moritz (2006). *Physical Geodesy*. Ed. by J. Gilluly and A. O. Woodford. Vol. 77. June. Springer, p. 412.

Holmes, S. and W. Featherstone (2002). "A unified approach to the Clenshaw summation and the recursive computation of very high degree and order normalised associated Legendre functions." In: *Journal of Geodesy*.

Hu, X. (2012). *Comparison of Ellipsoidal and Spherical Harmonics for Gravitational Field Modeling of Non-spherical Bodies*. Tech. rep. The Ohio State University.

IAU (2006). *RESOLUTION B5 - Definition of a Planet in the Solar System*.

Kahan, W. (1996). "IEEE standard 754 for binary floating-point arithmetic." In: *Lecture Notes on the Status of IEEE*.

MacMillan, W. D. (1958). *The theory of the potential*. Dover Publications Inc.

Meixner, J. and F. W. Schäfke (1954). *Mathieusche Funktionen und Sphäroidfunktionen*. Berlin, Heidelberg: Springer Berlin Heidelberg.

Miller, J. et al. (2002). "Determination of shape, gravity, and rotational state of asteroid 433 Eros." In: *Icarus*.

Nolan, M. C. et al. (Sept. 2013). "Asteroid (101955) Bennu Shape Model V1.0." en. In: *NASA Planetary Data System* 211.

Olver, F. et al., eds. (2010). *NIST Handbook of Mathematical Functions*. New York, NY: Cambridge University Press.

Panou, G. (2014). *A Study on Geodetic Boundary Value Problems in Ellipsoidal Geometry*. Tech. rep. National Technical University of Athens.

Park, R. et al. (Sept. 2014). "Gravity field expansion in ellipsoidal harmonic and polyhedral internal representations applied to Vesta." In: *Icarus* 240, pp. 118–132.

Sansò, F. and M. Sideris (2013). *Geoid Determination*. Ed. by F. Sansò and M. G. Sideris. Vol. 110. Lecture Notes in Earth System Sciences. Berlin, Heidelberg: Springer Berlin Heidelberg.

Scheeres, D. (2012). "Orbital Motion in Strongly Perturbed Environments." en. In: *Orbital Motion in Strongly Perturbed Environments, by Scheeres, Daniel J. ISBN: 978-3-642-03255-4. Berlin: Springer, 2012* -1.

The NIST Reference On Constants Units and Uncertainty (2014). *Newtonian constant of gravitation G*.

Thong, N. C. (1989). "Simulation of gradiometry using the spheroidal harmonic model of the gravitational field." In: *Manuscr. Geodaet.* 14, pp. 404–417.

Thong, N. C. and E. Grafarend (1989). "A spheroidal harmonic model of the terrestrial gravitational field." en. In: *Manuscr. Geod.* 14, pp. 285–304.

Tsoulis, D. (Mar. 2012). "Analytical computation of the full gravity tensor of a homogeneous arbitrarily shaped polyhedral source using line integrals." In: *GEOPHYSICS* 77.2, F1–F11.

Wang, Z. et al. (1989). *Special functions*. World Scientific.

Werner, R. and D. Scheeres (1997). “Exterior gravitation of a polyhedron derived and compared with harmonic and mascon gravitation representations of asteroid 4769 Castalia.” In: *Celestial Mechanics and Dynamical Astronomy* 65.3.

Appendix A.

Legendre Functions of the Second Kind, Method 2

In this part, the results of Thong and Grafarend (1989) to compute the ALF2 are shown.

The gravitational potential is expressed in terms of oblate spheroidal harmonics by

$$V(u,\vartheta,\lambda) = \frac{GM}{a_1}\sum_{n=0}^{\infty}\sum_{m=0}^{n}\frac{Q_{nm}\left(i\frac{u}{E}\right)}{Q_{nm}\left(i\frac{b}{E}\right)}P_{nm}(\cos\vartheta)\left[c_{nm}\cos m\lambda + s_{nm}\sin m\lambda\right], \tag{A.1}$$

where P_{nm} and Q_{nm} are the associated Legendre functions of the first and second kind, respectively.

The functions Q_{nm} are given by the recurrence relation

$$Q_{nm}(\eta) = \sum_{k=0}^{K} Q_{nmk}(\eta), \tag{A.2}$$

where

$$\begin{aligned} Q_{nmk}(\eta) &= \frac{(1-n-m-2k)(n+m+2k)}{2k(2n+2k+1)(\sinh\eta)^2}Q_{n,m,k-1}(\eta), \\ Q_{nm0}(\eta) &= (\coth\eta)^m\left(\frac{\cosh\eta_0}{\sinh\eta}\right)^{n+1} \end{aligned} \tag{A.3}$$

and

$$\eta = \operatorname{arcsinh}\frac{u}{E}, \qquad \eta_0 = \operatorname{arcsinh}\frac{b}{E}. \tag{A.4}$$

The upper sum limit K depends on the reference spheroid. Example Earth: In order to achieve an accuracy of 10×10^{-15} for $n = m = 1000$, the number of required terms was found to be 28 (Thong and Grafarend, 1989, Figure 3.1).

Appendix B.

Lamé Polynomials and Normalization

The following is a brief summary of the results presented in (Garmier and Barriot, 2001). The final formula to compute the normalization factor was edited according to (Dassios, 2012). Some symbols are used, like the semi-focal distances k_i, which can be looked up in the main text of this thesis.

Lamé Polynomials

The polynomial coefficients b as needed in Eq. 4.38 are obtained by solving the eigenvalue problem

$$\tilde{\mathbf{M}}_{(\mathcal{K},\mathcal{L},\mathcal{M},\mathcal{N})}\tilde{\mathbf{V}} = p\tilde{\mathbf{V}} \tag{B.1}$$

with

$$\tilde{\mathbf{M}}_{(\mathcal{K},\mathcal{L},\mathcal{M},\mathcal{N})} = \begin{pmatrix} \tilde{d}_0 & \tilde{g}_0 & 0 & 0 & \cdots & 0 \\ \tilde{f}_1 & \tilde{d}_1 & \tilde{g}_1 & 0 & \cdots & 0 \\ 0 & \tilde{f}_2 & \tilde{d}_2 & \tilde{g}_2 & \cdots & 0 \\ \vdots & \ddots & \ddots & \ddots & \ddots & \vdots \\ 0 & 0 & \cdots & 0 & \tilde{f}_r & \tilde{d}_r \end{pmatrix}, \qquad \tilde{\mathbf{V}} = \begin{pmatrix} b_0 \\ b_1 \\ b_2 \\ \vdots \\ b_r \end{pmatrix}. \tag{B.2}$$

For index r refer to Eq. 4.32. The components of the matrix $\tilde{\mathbf{M}}$ depend on the solution class and the evenness or oddness of the degree n. They are listed in (Garmier and Barriot, 2001) and stated in Eqs. B.5 and B.6. The auxiliary constants are functions of the semi-focal distances and read

$$\alpha = k_3^2, \qquad \beta = k_2^2 - k_3^2, \qquad \gamma = \alpha - \beta. \tag{B.3}$$

An integer index i appears, defined in the ranges

$$i = \begin{cases} [0, r] & \text{for class } \mathcal{K} \\ [0, n-r-1] & \text{for class } \mathcal{L} \\ [0, n-r-1] & \text{for class } \mathcal{M} \\ [0, r-1] & \text{for class } \mathcal{N} \end{cases}. \tag{B.4}$$

For even n the components read

$$\begin{aligned}
\tilde{\mathbf{M}}_{\mathcal{K}} &= \begin{cases} \tilde{f}_i = -(2r-2i+2)(2r+2i-1)\,\alpha, \\ \tilde{d}_i = 2r(2r+1)\,\alpha - 4i^2\gamma, \\ \tilde{g}_i = -(2i+2)(2i+1)\,\beta. \end{cases} \\
\tilde{\mathbf{M}}_{\mathcal{L}} &= \begin{cases} \tilde{f}_i = -(2r-2i)(2r+2i+1)\,\alpha, \\ \tilde{d}_i = \left(2r(2r+1) - (2i+1)^2\right)\alpha + (2i+2)^2\,\beta, \\ \tilde{g}_i = -(2i+2)(2i+3)\,\beta. \end{cases} \\
\tilde{\mathbf{M}}_{\mathcal{M}} &= \begin{cases} \tilde{f}_i = -(2r-2i)(2r+2i+1)\,\alpha, \\ \tilde{d}_i = 2r(2r+1)\,\alpha - (2i+1)^2\,\gamma, \\ \tilde{g}_i = -(2i+2)(2i+1)\,\beta. \end{cases} \\
\tilde{\mathbf{M}}_{\mathcal{N}} &= \begin{cases} \tilde{f}_i = -(2r-2i)(2r+2i+1)\,\alpha, \\ \tilde{d}_i = 2r(2r+1)\,\alpha - (2i+2)^2\,\alpha + (2i+1)^2\,\beta, \\ \tilde{g}_i = -(2i+2)(2i+3)\,\beta. \end{cases}
\end{aligned} \tag{B.5}$$

and in the odd case

$$\begin{aligned}
\tilde{\mathbf{M}}_{\mathcal{K}} &= \begin{cases} \tilde{f}_i = -(2r-2i+2)(2r+2i+1)\,\alpha, \\ \tilde{d}_i = \left((2r+1)(2r+2) - 4i^2\right)\alpha + (2i+2)^2\,\beta, \\ \tilde{g}_i = -(2i+2)(2i+1)\,\beta. \end{cases} \\
\tilde{\mathbf{M}}_{\mathcal{L}} &= \begin{cases} \tilde{f}_i = -(2r-2i+2)(2r+2i+1)\,\alpha, \\ \tilde{d}_i = (2r+1)(2r+2)\,\alpha - (2i+1)^2\,\gamma, \\ \tilde{g}_i = -(2i+2)(2i+3)\,\beta. \end{cases} \\
\tilde{\mathbf{M}}_{\mathcal{M}} &= \begin{cases} \tilde{f}_i = -(2r-2i+2)(2r+2i+1)\,\alpha, \\ \tilde{d}_i = \left((2r+1)(2r+2) - (2i+1)^2\right)\alpha + 4i^2\beta, \\ \tilde{g}_i = -(2i+2)(2i+1)\,\beta. \end{cases} \\
\tilde{\mathbf{M}}_{\mathcal{N}} &= \begin{cases} \tilde{f}_i = -(2r-2i)(2r+2i+3)\,\alpha, \\ \tilde{d}_i = (2r+1)(2r+2)\,\alpha - (2i+2)^2\,\gamma, \\ \tilde{g}_i = -(2i+2)(2i+3)\,\beta. \end{cases}
\end{aligned} \tag{B.6}$$

Lamé Normalization

The ellipsoidal surface harmonics are normalized by the factor γ, computable via

$$\gamma_n^p = 4\pi\left(\alpha B - \beta A\right). \tag{B.7}$$

The coefficients α, β, A and B are solutions of the equation system

$$\begin{aligned}
\mathcal{I}_1 &= I_0(\mu)\,\alpha + I_1(\mu)\,\beta,\\
\mathcal{I}_2 &= I_0(\mu)\,A + I_1(\mu)\,B,\\
\mathcal{I}_3 &= I_0(\nu)\,\alpha + I_1(\nu)\,\beta,\\
\mathcal{I}_4 &= I_0(\nu)\,A + I_1(\nu)\,B,
\end{aligned} \tag{B.8}$$

with the four elliptic integrals

$$\begin{aligned}
\mathcal{I}_1 &= \int_{k_3}^{k_2} \frac{\left(E_n^p(\mu)\right)^2}{\sqrt{\left(\mu^2-k_3^2\right)\left(k_2^2-\mu^2\right)}}d\mu,\\
\mathcal{I}_2 &= \int_{k_3}^{k_2} \frac{\left(E_n^p(\mu)\right)^2\mu^2}{\sqrt{\left(\mu^2-k_3^2\right)\left(k_2^2-\mu^2\right)}}d\mu,\\
\mathcal{I}_3 &= \int_{0}^{k_3} \frac{\left(E_n^p(\nu)\right)^2}{\sqrt{\left(k_3^2-\nu^2\right)\left(k_2^2-\nu^2\right)}}d\nu,\\
\mathcal{I}_4 &= \int_{0}^{k_3} \frac{\left(E_n^p(\nu)\right)^2\nu^2}{\sqrt{\left(k_3^2-\nu^2\right)\left(k_2^2-\nu^2\right)}}d\nu,
\end{aligned} \tag{B.9}$$

and the basic integrals

$$\begin{aligned}
I_j(\mu) &= \frac{1}{2}\int_a^b \frac{\Lambda^j}{\sqrt{1-\Lambda}\sqrt{k_3^2\Lambda+\left(k_2^2-k_3^2\right)}\sqrt{-\Lambda}}d\Lambda \quad \text{with} \begin{cases} a=0,\\ b=1-\left(k_2^2/k_3^2\right),\\ j=0 \text{ or } 1,\end{cases}\\
I_j(\nu) &= \frac{1}{2}\int_a^b \frac{\Lambda^j}{\sqrt{1-\Lambda}\sqrt{k_3^2\Lambda+\left(k_2^2-k_3^2\right)}\sqrt{+\Lambda}}d\Lambda \quad \text{with} \begin{cases} a=0,\\ b=1,\\ j=0 \text{ or } 1.\end{cases}
\end{aligned} \tag{B.10}$$

Appendix C.

Observation Equations and Partial Derivatives

In this part we present the observation and parameter vectors and the design matrices involved in the least squares adjustment of determining the gravitational field coefficients from potential or acceleration values. For the sake of brevity, no further explanation will be given. The interested reader is referred to Chapter 6 or to the rich literature on this topic.

Spherical Harmonics

Potential

The observation and parameter vector and the design matrix are

$$\mathbf{l} = \begin{bmatrix} V_1 \\ V_2 \\ \vdots \\ V_K \end{bmatrix}, \qquad \mathbf{A} = \begin{bmatrix} \mathbf{A}_c & \mathbf{A}_s \end{bmatrix}, \qquad \mathbf{x} = \begin{bmatrix} \mathbf{x}_c \\ \mathbf{x}_s \end{bmatrix}, \tag{C.1}$$

where $V_k = V(r_k, \vartheta_k, \lambda_k)$ and

$$\mathbf{A}_c = \begin{bmatrix} \partial V_1/\partial c_{0,0} & \partial V_1/\partial c_{1,0} & \partial V_1/\partial c_{1,1} & \dots & \partial V_1/\partial c_{N,N} \\ \partial V_2/\partial c_{0,0} & \partial V_2/\partial c_{1,0} & \partial V_2/\partial c_{1,1} & \dots & \partial V_2/\partial c_{N,N} \\ \vdots & \vdots & \vdots & \ddots & \vdots \\ \partial V_K/\partial c_{0,0} & \partial V_K/\partial c_{1,0} & \partial V_K/\partial c_{1,1} & \dots & \partial V_K/\partial c_{N,N} \end{bmatrix} \tag{C.2}$$

$$\mathbf{A}_s = \begin{bmatrix} \partial V_1/\partial s_{1,1} & \partial V_1/\partial s_{2,1} & \partial V_1/\partial s_{2,2} & \dots & \partial V_1/\partial c_{N,N} \\ \partial V_2/\partial s_{1,1} & \partial V_2/\partial s_{2,1} & \partial V_2/\partial s_{2,2} & \dots & \partial V_2/\partial s_{N,N} \\ \vdots & \vdots & \vdots & \ddots & \vdots \\ \partial V_K/\partial s_{1,1} & \partial V_K/\partial s_{2,1} & \partial V_K/\partial s_{2,2} & \dots & \partial V_K/\partial s_{N,N} \end{bmatrix} \tag{C.3}$$

$$\mathbf{x}_c = \begin{bmatrix} c_{0,0} & c_{1,0} & c_{1,1} & \dots & c_{N,N} \end{bmatrix}^\mathsf{T} \tag{C.4}$$

$$\mathbf{x}_s = \begin{bmatrix} s_{1,1} & s_{2,1} & s_{2,2} & \dots & s_{N,N} \end{bmatrix}^\mathsf{T} \tag{C.5}$$

The partial derivatives are given by

$$\partial V_k/\partial c_{ij} = \frac{GM}{R}\left(\frac{R}{r}\right)^{i+1} P_{ij}(\cos\vartheta)\cos j\lambda \tag{C.6}$$

$$\partial V_k/\partial s_{ij} = \frac{GM}{R}\left(\frac{R}{r}\right)^{i+1} P_{ij}(\cos\vartheta)\sin j\lambda. \tag{C.7}$$

Acceleration Vector

In this case, the observation vector and design matrix are

$$\mathbf{l}_k = \begin{bmatrix} g_k^{x_1} \\ g_k^{x_2} \\ g_k^{x_3} \end{bmatrix}, \qquad \mathbf{A} = \begin{bmatrix} \mathbf{A}_c & \mathbf{A}_s \end{bmatrix}. \tag{C.8}$$

The parameter vector remains unchanged. In order to relate the gravitational acceleration to the coefficients, the total differential of the potential must be computed. We find

$$\begin{bmatrix} g_k^{x_1} \\ g_k^{x_2} \\ g_k^{x_3} \end{bmatrix} = \begin{bmatrix} (\partial V/\partial r_k)(\partial r_k/\partial x_1) + (\partial V/\partial \vartheta_k)(\partial \vartheta_k/\partial x_1) + (\partial V/\partial \lambda)(\partial \lambda_k/\partial x_1) \\ (\partial V/\partial r_k)(\partial r_k/\partial x_2) + (\partial V/\partial \vartheta_k)(\partial \vartheta_k/\partial x_2) + (\partial V/\partial \lambda)(\partial \lambda_k/\partial x_2) \\ (\partial V/\partial r_k)(\partial r_k/\partial x_3) + (\partial V/\partial \vartheta_k)(\partial \vartheta_k/\partial x_3) + (\partial V/\partial \lambda)(\partial \lambda_k/\partial x_3) \end{bmatrix}, \tag{C.9}$$

with the partial derivatives

$$\begin{aligned}
\partial V/\partial r &= -\frac{GM}{r^2}\sum_{n=0}^{N}\sum_{m=0}^{n}(n+1)\left(\frac{R}{r}\right)^n P_{nm}(t)\left[c_{nm}\cos m\lambda + s_{nm}\sin m\lambda\right], \\
\partial V/\partial \vartheta &= \frac{GM}{R}\sum_{n=0}^{N}\sum_{m=0}^{n}\left(\frac{R}{r}\right)^{n+1}\frac{d}{dt}P_{nm}(t)\left[c_{nm}\cos m\lambda + s_{nm}\sin m\lambda\right], \\
\partial V/\partial \lambda &= \frac{GM}{R}\sum_{n=0}^{N}\sum_{m=0}^{n}\left(\frac{R}{r}\right)^{n+1}P_{nm}(t)\, m\left[-c_{nm}\sin m\lambda + s_{nm}\cos m\lambda\right].
\end{aligned} \tag{C.10}$$

and

$$\partial r/\partial x_1 = \sin\vartheta\cos\lambda, \qquad \partial r/\partial x_2 = \sin\vartheta\sin\lambda, \qquad \partial r/\partial x_3 = \cos\vartheta, \tag{C.11}$$

$$\partial \vartheta/\partial x_1 = \frac{\cos\vartheta\cos\lambda}{r}, \qquad \partial \vartheta/\partial x_2 = \frac{\cos\vartheta\sin\lambda}{r}, \qquad \partial \vartheta/\partial x_3 = \frac{\sin\vartheta}{r}, \tag{C.12}$$

$$\partial \lambda/\partial x_1 = -\frac{\sin\lambda}{r\sin\vartheta}, \qquad \partial \lambda/\partial x_2 = \frac{\cos\lambda}{r\sin\vartheta}, \qquad \partial \lambda/\partial x_3 = 0. \tag{C.13}$$

In the denominators in the above equations we recognize the scale factors as introduced in Eq. 2.13. Knowing these derivatives it is easy to set up the design matrix analogously to Eqs. C.2 and C.3. The function, which is differentiated w.r.t. the coefficients is of course no longer the potential itself but the three components of the acceleration vector (Eq. C.9). Thus, this design matrix' number of rows is three times that of the potential matrix.

Oblate Spheroidal Harmonics

Potential

The same definitions as in the spherical case can be applied, i.e., Eqs. C.28-C.5. The partial derivatives w.r.t. the coefficients are different, of course:

$$\partial V_k/\partial c_{ij} = \frac{GM}{a_1} q_{ij}(x)\, P_{ij}(\cos\vartheta)\cos j\lambda \tag{C.14}$$

$$\partial V_k/\partial s_{ij} = \frac{GM}{a_1} q_{ij}(x)\, P_{ij}(\cos\vartheta)\sin j\lambda. \tag{C.15}$$

Acceleration Vector

Based on Eq. C.8 we find in the oblate spheroidal parametrization the vector

$$\begin{bmatrix} g_k^{x_1} \\ g_k^{x_2} \\ g_k^{x_3} \end{bmatrix} = \begin{bmatrix} (\partial V/\partial u_k)(\partial u_k/\partial x_1) + (\partial V/\partial \vartheta_k)(\partial \vartheta_k/\partial x_1) + (\partial V/\partial \lambda)(\partial \lambda_k/\partial x_1) \\ (\partial V/\partial u_k)(\partial u_k/\partial x_2) + (\partial V/\partial \vartheta_k)(\partial \vartheta_k/\partial x_2) + (\partial V/\partial \lambda)(\partial \lambda_k/\partial x_2) \\ (\partial V/\partial u_k)(\partial u_k/\partial x_3) + (\partial V/\partial \vartheta_k)(\partial \vartheta_k/\partial x_3) + (\partial V/\partial \lambda)(\partial \lambda_k/\partial x_3) \end{bmatrix}. \tag{C.16}$$

The partial derivatives are

$$\begin{aligned} \partial V/\partial u &= \frac{GM}{a_1}\sum_{n=0}^{N}\sum_{m=0}^{n}\frac{d}{dx}q_{nm}(x)\,P_{nm}(t)\left[c_{nm}\cos m\lambda + s_{nm}\sin m\lambda\right], \\ \partial V/\partial \vartheta &= \frac{GM}{a_1}\sum_{n=0}^{N}\sum_{m=0}^{n}q_{nm}(x)\,\frac{d}{dt}P_{nm}(t)\left[c_{nm}\cos m\lambda + s_{nm}\sin m\lambda\right], \\ \partial V/\partial \lambda &= \frac{GM}{a_1}\sum_{n=0}^{N}\sum_{m=0}^{n}q_{nm}(x)\,P_{nm}(t)\,m\left[-c_{nm}\sin m\lambda + s_{nm}\cos m\lambda\right]. \end{aligned} \tag{C.17}$$

and

$$\partial u/\partial x_1 = \frac{x_1(A_o+2B_o)}{4B_o u}, \quad \partial u/\partial x_2 = \frac{x_2(A_o+2B_o)}{4B_o u}, \quad \partial u/\partial x_3 = \frac{x_3\left(A_o+2B_o+2E^2\right)}{4B_o u}, \tag{C.18}$$

$$\partial \vartheta/\partial x_1 = \frac{x_1 x_3}{2B_o u\sin\vartheta}, \qquad \partial \vartheta/\partial x_2 = \frac{x_2 x_3}{2B_o u\sin\vartheta}, \qquad \partial \vartheta/\partial x_3 = \frac{1}{u\sin\vartheta}\left(\frac{x_3}{u}\frac{\partial u}{\partial x_3} - 1\right), \tag{C.19}$$

$$\partial \lambda/\partial x_1 = -\frac{x_2}{x_1^2+x_2^2}, \qquad \partial \lambda/\partial x_2 = \frac{x_1}{x_1^2+x_2^2}, \qquad \partial \lambda/\partial x_3 = 0. \tag{C.20}$$

The auxiliary terms A_o and B_o are defined in Eq. 2.19 and E in Eq. 2.20.

Prolate Spheroidal Harmonics

Potential

Analogously to the oblate case we have

$$\partial V_k/\partial c_{ij} = \frac{GM}{a_1}q_{ij}(y)\,P_{ij}(\cos\vartheta)\cos j\lambda \tag{C.21}$$

$$\partial V_k/\partial s_{ij} = \frac{GM}{a_1}q_{ij}(y)\,P_{ij}(\cos\vartheta)\sin j\lambda. \tag{C.22}$$

Acceleration Vector

Only minor changes to the oblate parametrization must be applied:

$$\begin{bmatrix} g_k^{x_1} \\ g_k^{x_2} \\ g_k^{x_3} \end{bmatrix} = \begin{bmatrix} (\partial V/\partial v_k)(\partial v_k/\partial x_1) + (\partial V/\partial \vartheta_k)(\partial \vartheta_k/\partial x_1) + (\partial V/\partial \lambda)(\partial \lambda_k/\partial x_1) \\ (\partial V/\partial v_k)(\partial v_k/\partial x_2) + (\partial V/\partial \vartheta_k)(\partial \vartheta_k/\partial x_2) + (\partial V/\partial \lambda)(\partial \lambda_k/\partial x_2) \\ (\partial V/\partial v_k)(\partial v_k/\partial x_3) + (\partial V/\partial \vartheta_k)(\partial \vartheta_k/\partial x_3) + (\partial V/\partial \lambda)(\partial \lambda_k/\partial x_3) \end{bmatrix}. \tag{C.23}$$

With

$$\begin{aligned} \partial V/\partial u &= \frac{GM}{a_1} \sum_{n=0}^{N} \sum_{m=0}^{n} \frac{d}{dy} q_{nm}(y) P_{nm}(t) \left[c_{nm} \cos m\lambda + s_{nm} \sin m\lambda \right], \\ \partial V/\partial \vartheta &= \frac{GM}{a_1} \sum_{n=0}^{N} \sum_{m=0}^{n} q_{nm}(y) \frac{d}{dt} P_{nm}(t) \left[c_{nm} \cos m\lambda + s_{nm} \sin m\lambda \right], \\ \partial V/\partial \lambda &= \frac{GM}{a_1} \sum_{n=0}^{N} \sum_{m=0}^{n} q_{nm}(y) P_{nm}(t) m \left[-c_{nm} \sin m\lambda + s_{nm} \cos m\lambda \right]. \end{aligned} \tag{C.24}$$

and

$$\partial v/\partial x_1 = \frac{x_1 (A_p + 2B_p)}{4B_p v}, \quad \partial v/\partial x_2 = \frac{x_2 (A_p + 2B_p)}{4B_p v}, \quad \partial v/\partial x_3 = \frac{x_3 \left(A_p + 2B_p - 2E^2\right)}{4B_p v}, \tag{C.25}$$

$$\partial \vartheta/\partial x_1 = \frac{x_1 x_3}{2B_p v \sin \vartheta}, \qquad \partial \vartheta/\partial x_2 = \frac{x_2 x_3}{2B_p v \sin \vartheta}, \qquad \partial \vartheta/\partial x_3 = \frac{1}{v \sin \vartheta} \left(\frac{x_3}{v} \frac{\partial v}{\partial x_3} - 1 \right), \tag{C.26}$$

$$\partial \lambda/\partial x_1 = -\frac{x_2}{x_1^2 + x_2^2}, \qquad \partial \lambda/\partial x_2 = \frac{x_1}{x_1^2 + x_2^2}, \qquad \partial \lambda/\partial x_3 = 0. \tag{C.27}$$

The auxiliary terms A_p and B_p are defined in Eq. 2.25.

Ellipsoidal Harmonics

Potential

The design matrix and the parameter vector are now given by

$$\mathbf{A} = \begin{bmatrix} \partial V_1/\partial \alpha_0^1 & \partial V_1/\partial \alpha_1^1 & \partial V_1/\partial \alpha_1^2 & \cdots & \partial V_1/\partial \alpha_N^{2N+1} \\ \partial V_2/\partial \alpha_0^1 & \partial V_2/\partial \alpha_1^1 & \partial V_2/\partial \alpha_1^2 & \cdots & \partial V_2/\partial \alpha_N^{2N+1} \\ \vdots & \vdots & \vdots & \ddots & \vdots \\ \partial V_K/\partial \alpha_0^1 & \partial V_K/\partial \alpha_1^1 & \partial V_K/\partial \alpha_1^2 & \cdots & \partial V_K/\partial \alpha_N^{2N+1} \end{bmatrix}, \quad \mathbf{x} = \begin{bmatrix} \alpha_0^1 \\ \alpha_1^1 \\ \vdots \\ \alpha_N^{2N+1} \end{bmatrix}, \tag{C.28}$$

with

$$\partial V_k / \partial \alpha_i^j = GM \cdot V_i^j. \tag{C.29}$$

The definition of V_i^j can be found in Section 4.3.

Acceleration Vector

According to (Garmier and Barriot, 2001) the gravitational acceleration vector in ellipsoidal parametrization can be expressed as

$$\begin{bmatrix} g_{x_1} \\ g_{x_2} \\ g_{x_3} \end{bmatrix} = GM \sum_{n=0}^{N} \sum_{p=1}^{2n+1} \alpha_n^p \begin{bmatrix} V_n^p \left(\partial \Psi_n^p / \partial x_1 + \Psi_n^p \Upsilon_{x_1}^{n,p} \right) \\ V_n^p \left(\partial \Psi_n^p / \partial x_2 + \Psi_n^p \Upsilon_{x_2}^{n,p} \right) \\ V_n^p \left(\partial \Psi_n^p / \partial x_3 + \Psi_n^p \Upsilon_{x_3}^{n,p} \right) \end{bmatrix}, \tag{C.30}$$

where Ψ_n^p is the quantity from Eq. 4.43. Its partial derivatives w.r.t. the Cartesian coordinates are trivial and not stated here. The computation of Υ_{x_i} is accomplished using the formula

$$\begin{aligned} \Upsilon_{x_i} = & \left(\frac{\partial \rho}{\partial x_i} \frac{1}{P_n^p(\rho)} \frac{dP_n^p(\rho)}{d\rho} + \frac{\partial \mu}{\partial x_i} \frac{1}{P_n^p(\mu)} \frac{dP_n^p(\mu)}{d\mu} + \frac{\partial \nu}{\partial x_i} \frac{1}{P_n^p(\nu)} \frac{dP_n^p(\nu)}{d\nu} \right) + \\ & + \frac{1}{I_n^p(\rho)} \frac{dI(\rho)}{d\rho} \frac{\partial \rho}{\partial x_i}. \end{aligned} \tag{C.31}$$

The integral I_n^p and its derivative are stated in Section 4.3. Differentiation of the Lamé polynomials w.r.t. the ellipsoidal coordinates is easily found to be

$$\frac{dP_n^p(\lambda_i)}{d\lambda_i} = -\frac{2\lambda_i b_i}{k_3^2} \sum_{j=0}^{N_f - 1} m \left(1 - \frac{\lambda_i^2}{k_3^2} \right)^{j-1}, \tag{C.32}$$

where λ_i represents one of the three ellipsoidal coordinates. The partial derivatives of the ellipsoidal coordinates are given by

$$\begin{aligned} \partial \rho / \partial x_1 &= \frac{x_1}{\rho} \frac{\left(\rho^2 - k_2^2\right)\left(\rho^2 - k_3^2\right)}{\left(\rho^2 - \mu^2\right)\left(\rho^2 - \nu^2\right)}, \\ \partial \rho / \partial x_2 &= x_2 \frac{\rho\left(\rho^2 - k_2^2\right)}{\left(\rho^2 - \mu^2\right)\left(\rho^2 - \nu^2\right)}, \\ \partial \rho / \partial x_3 &= x_3 \frac{\rho\left(\rho^2 - k_3^2\right)}{\left(\rho^2 - \mu^2\right)\left(\rho^2 - \nu^2\right)}, \end{aligned} \tag{C.33}$$

and

$$\begin{aligned}
\partial\mu/\partial x_1 &= \frac{x_1}{\mu}\frac{\left(\mu^2-k_2^2\right)\left(\mu^2-k_3^2\right)}{\left(\mu^2-\rho^2\right)\left(\mu^2-\nu^2\right)},\\
\partial\mu/\partial x_2 &= x_2\frac{\mu\left(\mu^2-k_2^2\right)}{\left(\mu^2-\rho^2\right)\left(\mu^2-\nu^2\right)},\\
\partial\mu/\partial x_3 &= x_3\frac{\mu\left(\mu^2-k_3^2\right)}{\left(\mu^2-\rho^2\right)\left(\mu^2-\nu^2\right)},
\end{aligned} \tag{C.34}$$

and

$$\begin{aligned}
\partial\nu/\partial x_1 &= \frac{x_1}{\nu}\frac{\left(\nu^2-k_2^2\right)\left(\nu^2-k_3^2\right)}{\left(\nu^2-\rho^2\right)\left(\nu^2-\mu^2\right)},\\
\partial\nu/\partial x_2 &= x_2\frac{\nu\left(\nu^2-k_2^2\right)}{\left(\nu^2-\rho^2\right)\left(\nu^2-\mu^2\right)},\\
\partial\nu/\partial x_3 &= x_3\frac{\nu\left(\nu^2-k_3^2\right)}{\left(\nu^2-\rho^2\right)\left(\nu^2-\mu^2\right)}.
\end{aligned} \tag{C.35}$$

Appendix D.

Reference Figures

The following tables present the dimensions of the reference spheres, spheroids and ellipsoids belonging to the four small bodies presented in Chapter 7.

Figure	a_1	a_2	a_3
Sphere	17.9	17.9	17.9
Oblate	18.3	18.3	7.4
Prolate	21.4	10.3	10.3
Ellipsoid	20.3	11.4	7.6

Table D.1.: Reference figures 433 Eros. Units are kilometres.

Figure	a_1	a_2	a_3
Sphere	300	300	300
Oblate	300	300	275
Prolate	300	285	285
Ellipsoid	300	280	267

Table D.2.: Reference figures 101955 Bennu. Units are metres.

Figure	a_1	a_2	a_3
Sphere	114.9	114.9	114.9
Oblate	117.9	117.9	96.3
Prolate	116.1	112.3	112.3
Ellipsoid	118.5	112.8	96.9

Table D.3.: Reference figures 29 Amphitrite. Units are kilometres.

Figure	a_1	a_2	a_3
Sphere	3020	3020	3020
Oblate	3050	3050	2040
Prolate	3040	2350	2350
Ellipsoid	3050	2380	2070

Table D.4.: Reference figures 67P/Churyumov-Gerasimenko. Units are metres.